UNIVERSITÀ DEGLI STUDI DI PADOVA

Dipartimento di Fisica e Astronomia "Galileo Galilei"

Corso di Laurea Magistrale in Fisica

Tesi di Laurea

Study of Shape Coexistence in the ^{188}Hg nucleus via lifetime measurements

Relatore

Dr. Alain Goasduff

Correlatore

Dr. Marco Siciliano

Laureanda

Irene Zanon

Anno Accademico 2017/2018

Introduction

I come in different colors and shapes, some parts of me are curvy, some parts are straight, I'm am everywhere but only belong to one place

A riddle

The aim of this thesis is the study of shape coexistence in the neutron-deficient ^{188}Hg isotope, populated via a fusion-evaporation reaction and studied by lifetime measurements with two dedicated experiments performed at the Legnaro National Laboratories (LNL) in 2016.

Shape coexistence is a characteristic phenomenon of finite many-body quantum systems where different nuclear shapes coexist within the typical energy range of nuclear excitations. Many previous experiments confirmed the presence of such phenomenon in the neutron-deficient nuclei around Z = 82, in particular in light isotopes of Hg using different reactions (Coulomb excitation, fusion evaporation) and different techniques (matrix elements extrapolation, Recoil Distance Doppler-Shift method, Doppler-Shift Attenuation Method). From the systematics of the mercury isotopes and from theoretical calculations, ^{188}Hg is expected to be the heaviest isotope where two different shapes coexist. However, for this nucleus information on the electromagnetic properties of low-lying states is scarce or absent. Thus, an investigation of the ^{188}Hg states is of great interest for a better comprehension of shape coexistence in this region.

This work presented in this thesis is organized as follow.

In Chapter 1, the phenomenon of shape coexistence is explained. I will briefly present the two main theoretical approaches used to describe this phenomenon. Then an overview on the experimental fingerprints and on the previous experiments is given to finally focus on the nucleus of interest, the ^{188}Hg.

In Chapter 2, the experimental apparatus is described: the Tandem-ALPI accelerator complex was used to accelerate the beam while the reaction was studied using the GALILEO array coupled with the Neutron Wall array and the plunger device. The employed detectors

and their main characteristics will also be also described.

In Chapter 3, the pre-sorting of the experimental data will be presented, focusing in particular on the calibration of the different detectors, on the optimization of the spectra and on the lime and energy alignment of the apparatuses.

In Chapter 4 the analysis of the experimental data and the results will be presented. In particular, this work is aimed at the lifetime determination of the 2_1^+, 4_1^+, 6_1^+ and 8_1^+ states via Recoil Distance Doppler-Shift method. This technique will also be explained in the chapter.

Finally, in Chapter 5 a theoretical interpretation of the experimental data is given. The ^{188}Hg was studied via Symmetry-Conserving Configuration-Mixing (SCCM) method. The theoretical framework and the results are presented together with a comparison with previous calculations and with experimental data.

Moreover, for a better comprehension of topics that will be discussed, a rapid review on nuclear models, nuclear reactions and electromagnetic radiations is presented in Appendices A, B and C, respectively.

Contents

1. Shape Coexistence **7**
1.1. Theoretical introduction . . . 7
1.2. Experimental fingerprints . . . 9
1.3. Shape coexistence in neutron-deficient Hg isotopes . . . 11

2. Experimental apparatus **15**
2.1. Accelerators . . . 16
2.2. GALILEO spectrometer . . . 17
2.2.1. γ-ray detectors . . . 18
2.2.2. Anti-Compton shields . . . 19
2.2.3. GALILEO phase II . . . 21
2.3. Neutron Wall . . . 22
2.4. The Plunger device . . . 24

3. Pre-sorting of experimental data **25**
3.1. GALILEO . . . 25
3.1.1. Energy calibration . . . 25
3.1.2. Efficiency . . . 29
3.2. Compton Suppression . . . 29
3.3. Pile up rejection . . . 32
3.4. Stability of the HPGe . . . 33
3.5. Time alignment . . . 33
3.6. Neutron Wall calibration . . . 36
3.7. The plunger device . . . 39

4. Analysis and Results **41**
4.1. Determination of the ^{188}Hg velocity . . . 41
4.2. Neutron-gamma discrimination . . . 43
4.3. The RDDS method . . . 44
4.3.1. Decay-Curve Method . . . 45
4.3.2. Differential Decay-Curve Method . . . 48

4.4. Lifetime results 49
4.4.1. Lifetime of the 2_1^+ 49
4.4.2. Lifetime of the 4_1^+ 53
4.4.3. Lifetime of the 6_1^+ 55
4.4.4. Lifetime of the 8_1^+ 56

5. Theoretical Interpretation **59**
5.1. B(E2) systematics along the Hg isotopic chain 59
5.2. Symmetry-conserving configuration-mixing methods 61
5.3. Comparison with the experimental results 65

6. Conclusions **67**

A. Nuclear models **69**
A.1. The shell model 69
A.2. Collective model 71

B. Nuclear reactions **75**

C. Electromagnetic radiation **79**
C.1. Classical interpretation 79
C.2. Quantum interpretation and selection rules 81
C.3. Internal conversion 83
C.4. Gamma-matter interaction 85

Bibliography **87**

1 Shape Coexistence

Already observed in atomic nuclei and in molecules for over 50 years [1], shape coexistence is a peculiar phenomenon of many-body quantum systems where the structures belonging to different shapes coexist within typical energy range of nuclear excitation (typically from 100 keV−10 MeV). The principle behind this phenomenon is the contrast between two different forces: on one hand valence nucleons and $np-nh$ excitations drive the nucleus to a deformed shape; on the other hand, pairing forces and shell effects lead to a spherical shape. While at first it was considered an exotic phenomenon, now it has been observed in many nuclei and it is known to exhibit an island of occurrence at certain mass values, as for example the neutron-deficient region close to and at the proton shell closure Z=82. For even-even nuclei, as in the case of the ^{188}Hg, the appearance of a deformed band, built on the top of a low-lying 0^+ state close to the ground-state band, is a distinctive fingerprint of shape mixing [2].

In this chapter two theoretical approaches will be introduced and then a review on the experimental fingerprints in the region of interest will be provided. Finally, a review on previous measurements and theoretical predictions of Hg isotopes will be presented.

1.1. Theoretical introduction

When studying the shape coexistence in atomic nuclei, two theoretical approaches are possible: on one hand, the spherical shell-model approach with the addition of the residual proton-nucleon force; on the other hand, the mean-field approach, to obtain the single-particle states starting from a two-body interaction.

Spherical shell-model approach

The starting point of this first method is the Hamiltonian [1]

$$\hat{H} = \sum_{\alpha} \varepsilon_a a^{\dagger}_{\alpha} a_{\alpha} + \frac{1}{4} \sum_{\alpha\beta\gamma\delta} \langle \alpha\beta | V | \gamma\delta \rangle \, a^{\dagger}_{\alpha} a^{\dagger}_{\beta} a_{\delta} a_{\gamma} \tag{1.1}$$

where two main components can be identified: the first term contains the information on the single-particle energies ε_a that can be determined from self-consistent Hartree-Fock (HF) calculations or from experimental neutron and proton separation energies; the second term represents the residual two-body nuclear interaction. In particular, the inclusion of particles

excitations across closed shell helps to describe the lowering of the excitation energy of the deformed side band.

In order to simplify the resolution of the quantum problem, the Hamiltonian can be re-written as a sum of two components [3]

$$\hat{H} = \hat{H}_{mon} + \hat{H}_M \tag{1.2}$$

where $\hat{H}_{mon}$ is the monopole part of the Hamiltonian, having the information on the spherical mean field extracted from the interacted shell model, while $\hat{H}_M$ contains all the higher order multipole components (quadrupole, octupole, etc.) that are fundamental to describe strong correlations between nucleons and they lead to collective behaviours such as deformations. The monopole part can be written as [1]

$$\hat{H}_{mon} = \sum_i \varepsilon_{\nu_i}\hat{n}_{\nu_i} + \sum_i \varepsilon_{\pi_i}\hat{n}_{\pi_i} + \sum_{ij} V_{ij}^{\nu\pi}\hat{n}_{\nu_i}\hat{n}_{\pi_j} + \sum_{i\leq j} \frac{\hat{n}_{\nu_i}(\hat{n}_{\nu_j} - \delta_{ij})}{1+\delta_{ij}} V_{ij}^{\nu\nu} + \sum_{i\leq j} \frac{\hat{n}_{\pi_i}(\hat{n}_{\pi_j} - \delta_{ij})}{1+\delta_{ij}} V_{ij}^{\pi\pi} \tag{1.3}$$

where $\hat{n}_\nu$ and $\hat{n}_\pi$ are the neutron- and proton-number operators, respectively. This $\hat{H}_{mon}$ is an important instrument to better understand the formation of shells and to predict the variation of shell gaps as a function of nucleons number.

This nuclear shell model approach allows the description of many features, such as the appearance of magic numbers or possible low-lying intruder states. These calculations are very demanding from a computational point of view and their application to nuclei heavier than A=100 is restricted to region a few nucleon away from doubly magic nuclei. Hence for the study of heavy exotic nuclei such as ^{188}Hg, that is the nucleus of interest of this thesis, it is necessary to consider a mean-field approach.

Mean-field approach

The mean-field approach is based on the effective forces and on self-consistent Hartree-Fock(-Bogoliubov) (HFB) theory. The basic idea behind this method is the description of global nuclear properties by studying the potential-energy surface. The most common interactions used in these calculations are the Skyrme and the Gogny interactions. The variational method is applied in order to determine the single-particle wave functions and then to build a nuclear many-body wave function from the independent (quasi)particle states. However, the mean-field approach is defined in the intrinsic frame so, in order to obtain the information on the nucleus, it is necessary to project the wave function into the laboratory frame. Finally, the symmetries, that have been broken in the process, are restored by projecting the mean-field states onto fixed quantum numbers as, for example, the particle number (N, Z), the isospin (T) or the angular momentum (J) [1].

The shell-model and the mean-field methods present several advantages and disadvantages. The former is a powerful method that has a strong predictive power, but precise calculations would not be feasible for heavy nuclei with current computer capabilities. The latter leads to an energy surface that is semiclassical and, in order to reach results that can be compared with the experimental data, one has to project the mean-field states from the intrinsic to the laboratory frame. Nowadays, the theoretical knowledge and the precision of these two methods have come to a point where they often lead to the same results.

In the present work the ^{188}Hg will be studied using a beyond mean-field approach, in par-

ticular via symmetry-conserving configuration-mixing (SCCM) method. Further information about this technique will be given in Chapter 5.

1.2. Experimental fingerprints

In nuclear physics there are different experimental evidences about the presence of shape coexistence.

The most evident signatures about this phenomenon are given by rapid changes along the isotopic chains of mean-square radii, masses or pair occupancies. Usually these signatures are the easiest to notice, especially in nuclei far from the stability, and so they are often the first to be observed. Such quantities can be a good starting point for a systematic study of the region. An example of these features is offered by the study of the Hg isotopes [1]: the drastic change in the charge mean-square radius between the ^{181}Hg and the ^{185}Hg isotopes, as shown in Figure 1.1, suggests the presence of a large nuclear deformation. However, these observations do not represent an incontestable proof for the shape coexistence: in fact, this rapid change in the charge radii is not observed in Pb and Po neutron-deficient nuclei, even if the phenomenon of shape coexistence is well established along these isotopic chains.

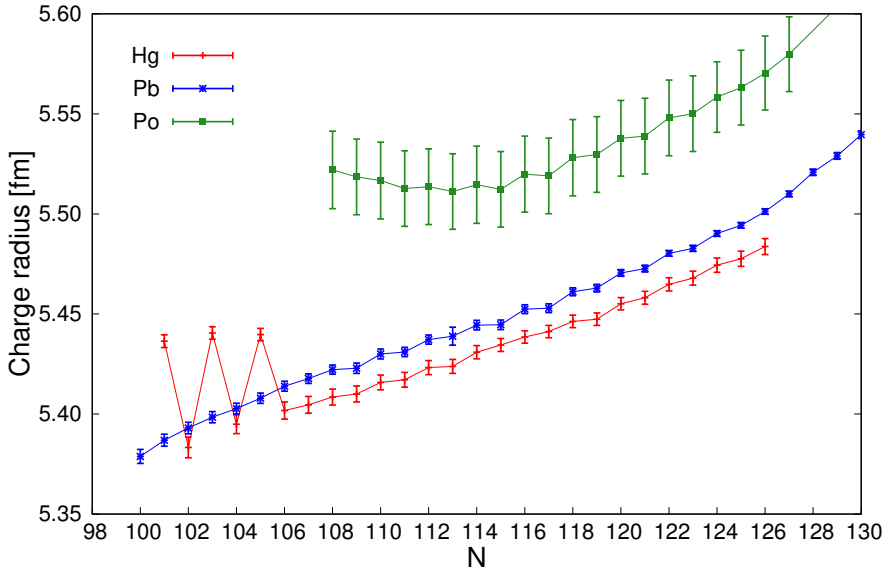

Figure 1.1.: Charge radius systematics for the Hg, Pb and Po isotopes. The large variation in the charge radius between ^{185}Hg and ^{187}Hg is a fingerprint of the presence of a change in the nuclear deformation. The same change is not observed in the isotopic chains of the Pb and Po, even though the shape coexistence is well established in these nuclei. Data taken from [4].

This is particularly evident in the case of ^{186}Pb, as shown by A. Adreyev et al [5], where three bands with different deformations were found at low energy. The potential-energy surface calculated for ^{186}Pb, presented in Fig. 1.2, exhibits three minima within a 2 MeV range with three different deformation: a spherical one corresponding to the ground states band, an oblate one corresponding to the band built on the first excited 0^+ (532 keV) and finally a prolate one correspond to the second excited 0^+ (650 keV).

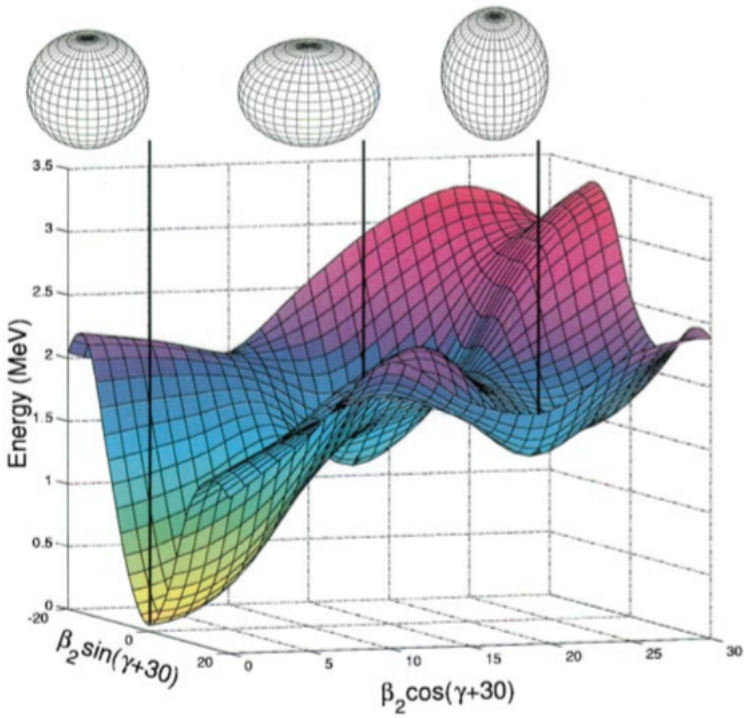

Figure 1.2.: Calculated potential-energy surface for ^{186}Pb. The spherical, oblate and prolate minima are indicated with the black vertical lines. Figure from [5].

Another indication of a strong shape mixing in a nucleus is the observation of a large interband E0 strength: this characteristic of the E0 transitions provides informations on the nuclear structure, in particular on the volume oscillations, the shape coexistence and the isotopes and isotones [6]. The electric monopole operator couples the nucleus to the atomic electrons, giving rise to the internal conversion process. The strength of these transitions, usually quantified by the dimensionless quantity $\rho(E0)$, is related to difference in mean-square charge radii between the involved states (for more details see Eq. (C.17)) and usually it is quantified through the measurement of conversion electrons line intensities. For example, in Figure 1.3 the strenght of the E0 transitions for isotonic chain N=90 near Z=64 is presented. The large values indicate the coexistence of bands with different deformations that mix strongly.

However, the signature we decided to focus in this thesis is given by the electric quadrupole (E2) matrix elements and by the reduced transition probabilites B(E2) which can be obtain via Coulomb excitation and/or lifetime measurements. The B(E2) values in particular give information about the internal structure of the nucleus and on its collectivity: the transitions probabilities are expected to be higher at midshell, where the number of valence nucleons is larger, while they are usually significantly reduced near the shell closure. Thus, any variation with respect to the expected trend of the B(E2) in the isotopic chain could suggest some changing in the collectivity of the nucleus. In this thesis, the measurement of the reduced transition probabilities via lifetime measurement is the method chosen to investigate the presence of shape coexistence in the ^{188}Hg nucleus. More information will be given in the following chapters.

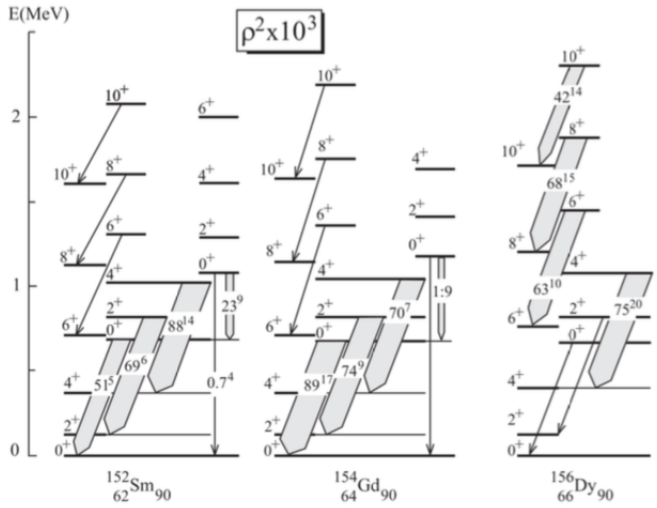

Figure 1.3.: E0 transitions strength in the isotone chain of N=90. The large values of the ρ^2 are an experimental evidence of strong shape mixing. Figure taken from Ref. [1].

1.3. Shape coexistence in neutron-deficient Hg isotopes

The neutron-deficient region near and at Z=82 presents the most intense manifestation of shape coexistence, but its investigation presents numerous experimental difficulties due to the large mass and the exoticism of the nuclei of interest. However, in the recent years the neutron-deficient mercury isotopes have been largely studied both theoretically and experimentally [7–9]. Spectroscopic measurements revealed the presence of an intruder band close in energy to the ground-state band in isotopes from ^{180}Hg to ^{188}Hg, as shown in Figure 1.4.

A theoretical interpretation of such experimental results is given by relativistic Hartree-Bogoliubov (RHB) calculations [11]: the starting point is a mean-field approximation and then pairing correlations are included in order to describe the ground-state properties of open-shell nuclei. This approach predicts the ground-state of Hg isotopes being weakly oblate-deformed. In particular, in ^{188}Hg the ground-state band is expected to be crossed by an intruding prolate-deformed band whose excitation energy decreases for lighter isotopes and reaches a minimum for ^{182}Hg; then the nucleus moves toward a more spherical shape for more neutron-deficient nuclei. The results of these calculations are presented in Figure 1.5.

Similar results are reached also using beyond mean field (BMF) calculations and interacting boson models (IBM), that have been summarized in the works of N. Bree [12, 13]. In particular, the BMF approach predicts for $N \geq 106$ a ground-state band with weak deformation and an excited prolate band with stronger deformation. For nuclei with $100 \leq N \leq 104$ the two bands cross and the ground state is expected to be predominantly prolate, while the first excited 0^+ is expected to be an equal mixture of an oblate and a prolate configuration. These results are summarized in Figure 1.6.

From the experimental point of view, the neutron-deficient Hg isotopes have been investigated mainly via two different techniques: on one hand the lifetimes of excited states of nuclei populated via fusion-evaporation reactions have been directly measured via the Recoil Distance Doppler-shift (RDDS) method, as in the case of ^{180,182}Hg [14, 15] and ^{184,186}Hg

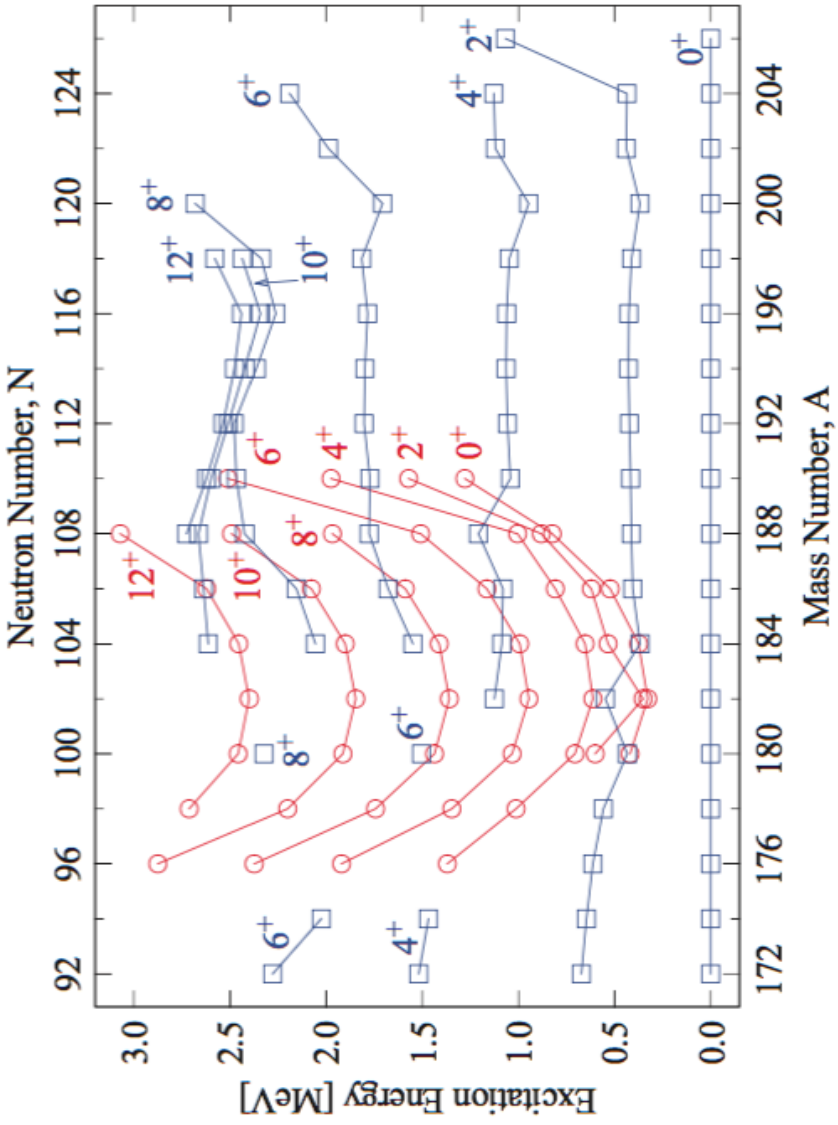

Figure 1.4.: Systematics of energy levels in even mercury isotopes. The levels belonging to the ground-state band are marked in blue, while those belonging to the assumed intruder band are marked in red. The intruder band is close in energy to the ground-state band for isotopes from N=100 to N=108. Figure taken from Ref. [10].

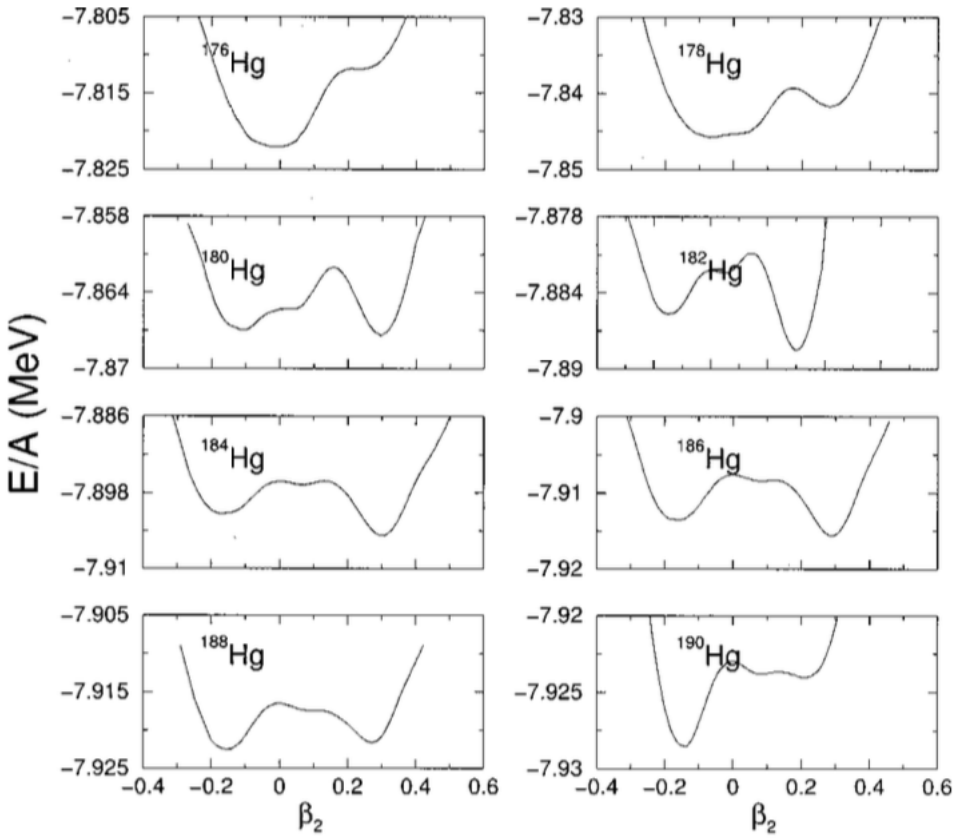

Figure 1.5.: Binding energy curves of even Hg isotopes as a function of the quadrupole deformation obtained with the Relativistic Hartree-Bogoliubov calculations of T. Nikšić and collaborators [11]. The ^{188}Hg is expected to have an oblate ground-state band crossed by an intruder band built on the top of a prolate 0^+ excited state. Figure from Ref. [11].

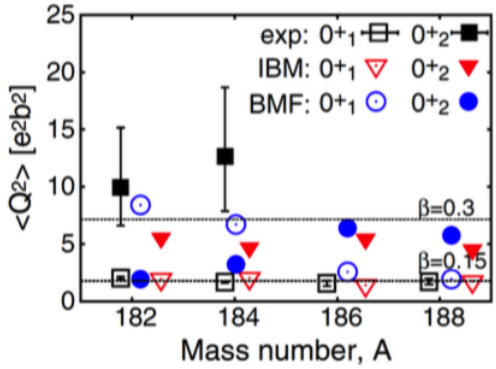

Figure 1.6.: Quadrupole deformation of even Hg isotopes. Two different theoretical approaches are compared to the experimental data. The ground state (0_1^+) of the ^{188}Hg is observed to be oblate deformed with $\beta_2 \sim 0.15$, in agreement with the theoretical predictions. Figure from Ref. [12].

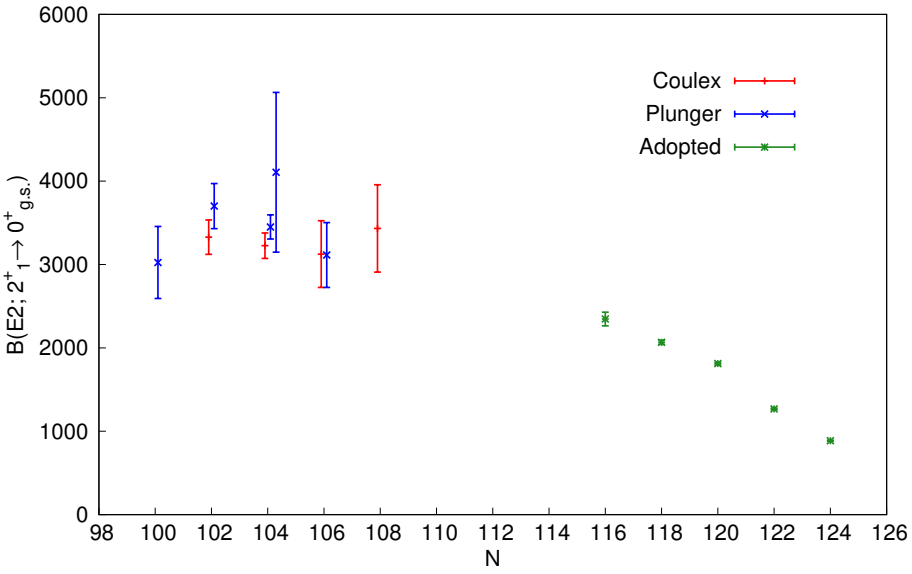

Figure 1.7.: Systematics of the $B(E2; 2_1^+ \rightarrow 0_{g.s.}^+)$ values in neutron-deficient mercury isotopes. Red dots refer to data obtained with Coulomb-excitation experiments, blue dots are from lifetime measurements with the plunger device, while the "adopted" values (green dots) are taken from [20]. The data present a parabolic trend with a plateau in the region between $N = 100$ (^{180}Hg) and $N = 108$ (^{188}Hg), where shape coexistence is expected.

[10, 16, 17], or via Doppler-Shift Attenuation Method[1] (DSAM) for the ^{186}Hg [19]; on the other hand, Coulomb-excitation measurements have been performed with radioactive ion beams, extracting the magnitude of the reduced E2 matrix elements for $^{182-188}$Hg isotopes [12]. These experimental results are summarized in Figure 1.7, where the $B(E2; 2_1^+ \rightarrow 0_{g.s.}^+)$ values are presented for neutron-deficient Hg isotopes as a function of the neutrons number. Because of the increasing collectivity driven by the number of valence neutrons, the BE(2) values are expected to increase while moving far from the shell closure and to follow a parabolic trend, but in this case a plateau is evident for $N < 110$. Such discrepancy is a hint of the presence of shape coexistence in this region.

From theoretical calculations, ^{188}Hg is expected to be the heaviest mercury isotope to manifest shape coexistence, and the Coulomb-excitation measurement seems to confirm these predictions. However, no direct measurement of the lifetime of the 2_1^+ level has been performed and there is no information on higher-spin states. For these reasons a thorough study of the low-lying states of the ^{188}Hg isotope via lifetime measurement, that is the aim of this thesis, is of great interest not only to investigate the possible presence of shape coexistence in this isotope but also to measure higher-spin levels lifetime for the first time.

[1] The Doppler-shift attenuation method is a technique for lifetimes measurements in the range of $10 - 1000$ fs based on the Doppler-shift of the γ ray due to the energy loss by the emitting nucleus in the target material [18].

2 Experimental apparatus

The aim of this thesis is the study of the electromagnetic properties of the ^{188}Hg low-lying states in order to investigate the possible presence of shape coexistence in this nucleus, as predicted by theoretical models [11, 12]. The nucleus of interest was populated via two different fusion-evaporation reactions: ^{34}S beam at the energy of 185 MeV impinged onto 600 $\mu g/cm^2$ of ^{160}Gd target (2.5 mg/cm^2 thick ^{181}Ta fronting) with the evaporation of 6 neutrons and ^{34}S beam at the energy of 165 MeV impinged onto 600 $\mu g/cm^2$ of ^{158}Gd target (2.5 mg/cm^2 thick ^{181}Ta fronting) with the evaporation of 4 neutrons[1]. Besides the ^{188}Hg, these two reactions opened different channels: from the comparison of the obtained spectra it was possible to control the presence of potential contamination from the de-excitation of the other populated nuclei, minimizing the effects on the lifetme measurement. The beam was provided by the Tandem-ALPI accelerators complex at the Laboratori Nazionali di Legnaro. For the γ-ray identification the high resolution HPGe detector array GALILEO was employed coupled with the ancillary detector array Neutron Wall, used to detect neutrons and distinguish them from photons, and therefore to select events that are in coincidence with at least a neutron. Finally, the plunger device is employed to measure the lifetime of the excited states. In this chapter a detailed description of the experimental apparatus, schematized in Figure 2.1, is presented.

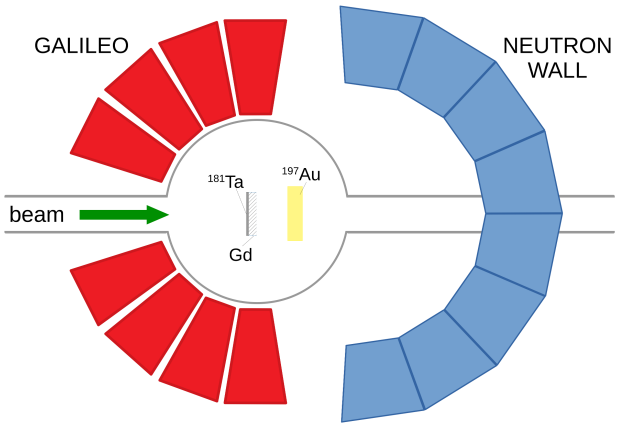

Figure 2.1.: Scheme of the experimental apparatus.

[1] In the following, these two experiments will be referred to as *week 11* and *week 30* respectively.

2.1. Accelerators

The Laboratori Nazionali di Legnaro (LNL) are one of the four national laboratories of the Istituto Nazionale di Fisica Nucleare (INFN), that focus its research activities on the study of nuclear physics, nuclear-astrophysics and applications [21].

At the moment, five linear accelerators are working at the LNL: two small machines, AN2000 (voltage terminal 2 MV) and CN (7 MV), that are usually employed for interdisciplinary research; the XTU-Tandem, a Van de Graaf accelerator; PIAVE, used as an injector, and ALPI, which is made of super-conducting cavities and it is used for the post-acceleration of the beam coming from the XTU-TANDEM or PIAVE. In addition to such machines, in 2015 a cyclotrone arrived at LNL and now it active and under tests. This accelerator is a fundamental part of the project SPES, a second generation ISOL radioactive ion beam facility. The cyclotron accelerates protons that will impinge on a uranium carbide target and produce radioactive ion beams in the neutron-rich region between $A = 60$ and $A = 130$ [22].

The XTU-Tandem accelerator

The XTU-Tandem is an electrostatic accelerator of stable beams, operating at the Laboratori Nazionali di Legnaro since 1981 [23, 24]. It provides a wide variety of different ions (from ^{1}H to ^{197}Au) with a high energy resolution. Two hight-voltage columns are placed inside a tank that contains 7 atm of SF_6, an inert gas used to prevent sparks that could damage the structure. An ion-source provides negative-charged ions that are injected in the beam tube and accelerated by an electric field from the grounding initial position to the positive high-voltage terminal placed at the center. This terminal is charged by two laddertron and it can reach 14.5 MV of voltage. After the terminal, a combination of carbon foils, called stripper foils, can be placed to remove electrons from the incoming ions: in this way ions are positively charged to a high charge state and the electric field accelerates them until the end of the beam tube. The scheme of the Tandem accelerator is shown in Figure 2.2. At this point, the beam can be delivered to the experimental area or injected to ALPI for the post-acceleration.

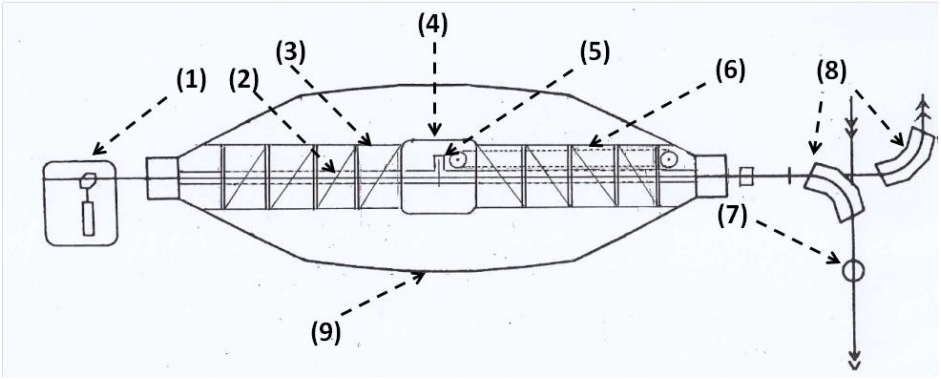

Figure 2.2.: Scheme of the XTU-Tandem. From the left, the following elements can be identified: (1) the ion source; (2) the accelerating pipe; (3) the column which supports the (4) high voltage terminal; (5) the ion beam "stripping" station; (6) the "laddertron"; (7) the beam diagnostic station; (8) bending magnets; (9) the tank filled in SF_6 gas at 7 atm. Figure from [21].

Figure 2.3.: On the left, a portion of ALPI where the cryostat, that thermally insulate the superconducting cavities, are shown. On the right, the interior of a cryostat, where the four high-purity copper-based cavities can be seen. Figure from [21].

The ALPI linear accelerator

ALPI is a radio-frequency (RF) linear accelerator, based on a superconducting Quarter-Wave Resonance (QWR) cavities. A buncher, operating at 80 MHz, provides the bunch structure essential for the acceleration in the oscillating electric field. Then the accelerator is devided in three sections with different velocities: a low-β with $\beta = 0.055$ (24 cavities), a medium-β section with $\beta = 0.11$ (44 cavities) and a high-β section with $\beta = 0.14$ (24 cavities) [25]. The cavities are cooled down by liquid helium to maintain them in a superconducting state. Finally, after the acceleration, the beam is transferred to the experimental halls and to the dedicated experimental apparatus. Two pictures of ALPI, showing the cryostats (left) and the four cavities inside of them (right), are presented in Figure 2.3.

2.2. GALILEO spectrometer

GALILEO is an array of high-purity germanium (HPGe) detectors, which are surrounded by bismuth germanate (BGO) crystals acting as anti-Compton shields, mounted in the LNL [26]. This apparatus is used to investigate nuclear structure via in-beam γ-ray spectroscopy methods. In particular, its versatile design allows to couple the HPGe array with several ancillary detectors in order to improve the selectivity, making rare and exotic nuclear species experimentally accessible.

The GALILEO array is designed to have a symmetric geometry of the HPGe detectors with respect to the beam axis [27] and to maximize the photo-peak efficiency under typical in-beam medium-high γ-ray multiplicity. The current total photopeak efficiency at 1332 keV

Figure 2.4.: On the left, a picture of the GALILEO infrastructure with the Neutron Wall array. On the right, a picture of the GALILEO array. The Compton-shields of the 10 HPGe detectors of the 90° ring are visible, hiding the 15 backward detectors. Figure from [26, 27]

is $\varepsilon \sim 2.4\%$.

In the current phase, GALILEO in composed of 25 HPGe detectors together with their anti-Compton shields. The HPGe are n-type and cylindrical with a coaxial symmetry and the FWHM at 1332 keV around ~ 2.4 keV [27]. The 25 GALILEO detectors are disposed in 4 rings: five of them are placed at 152°, five at 129°, five at 119° and ten at 90° with respect to the beam. The disposition is shown in Figure 2.4.

2.2.1. γ-ray detectors

γ-ray detection is one of the most powerful method to investigate the structure of nuclei. Semiconductor detectors with standard level of purity (e.g. silicon detectors) are usually employed for the detection of charged particles, but are ineffective in the detection of more penetrating radiation, as photons [28]. In fact, as described in Appendix C, the detection probability for electromagnetic radiation increases with the Z of the detector material. Thus, germanium (Z=34) represents the perfect compromise between detection efficiency, energy resolution and production costs.

The excitation mechanism in semiconductor crystals depends on the energy states determined by the crystal lattice of the material. The energy states are divided in three bands: the valence band at lower energy, where electrons are bounded with lattice sites, the conduction band, where electrons are free to move, and the forbidden band at medium energy, where electrons can not be found. When the radiation impinges on the detector, it promotes the electron of the lattice from the valence band to the conduction band, resulting in the creation of an electron-hole pair. Then, the electrons are then driven by an electrical field and amplified to form an electrical signal. The typical band gap of a silicon detector is 1.2 eV while for a germanium detector is about 0.7 eV [28]. This means that in germanium detectors the probability of forming an electron-hole pair is higher and results in a better resolution capability. However, this characteristic has another important consequence: because of the small band gap, is impossible to use germanium detectors at room-temperature, because the

leakage current induced by temperature would affect the performance of the detector. In fact, the room-temperature is sufficient to promote electron of the lattice from the valence gap to the conducting band and, when the detectors are under a high-voltage tension (typically -4000 V) these leakage currents damage the lattice. For this reason the detectors are cooled down with liquid nitrogen and the crystal temperature is kept between 77 K and 90 K.

To detect very penetrating radiation, a thicker detector is needed in order to increase the active volume, which also depends on the purity of the lattice. However, for some materials it is difficult to grow a large crystal and, because of the defects on the lattice, the dead layer increases with the volume as well and to reach greater depletion depths a higher level of purity must be reached. The required level of purity for the detection of photons has not yet been reached for silicon detectors but it has for germanium. These detectors are usually called *high-purity germanium* (HPGe) and are available with depletion depths of several centimeters. The level of impurity in HPGe is very low, about one impurity every 10^{12} atoms.

HPGe are characterized by an excellent energy resolution. For this reason they are largely used in γ-spectroscopy where the energy of the photons is between a few tens of keV to a few MeV and a high precision is required, such as the present experiment.

2.2.2. Anti-Compton shields

The scintillation mechanism in inorganic materials (as BGO crystals) is somehow similar to the procedure previously described for semiconductors: the energy states are also devided in three bands and when the material is hit by radiation, the electrons are promoted from the valence band to the conduction band. However in the case of a scintillator, the de-excitation of the electron is followed by the emission of a photon. In order to increase the probability of photon emission, a small amounts of impurities called *activators* are added to the crystal. These activators have also the effect of lowering the energy gap for the excitation of the electron, resulting in an increasing of the wavelenght of the radiation emitted, usually from the ultraviolet to the visible range [29]. The light produced in the scintillation process is converted in an electrical signal by a photomultiplier, coupled with the crystal. Photons that struck the cathode of the photomultiplier are converted into a current via a photoelectric process and then the electrical signal is amplified to be measurable. A schematic view of a photomultiplier is presented in Figure 2.5.

The bismuth germanate crystal (commonly known as BGO) has a very hight density that results in largest probability per unit volume for the photoelectric absorption of γ ray, leading to a very high efficiency. On the other side, BGO have a low light yield which entails a low energy resolution (10 times worse than HPGe). Each HPGe detectors of GALILEO is surrounded by eight BGOs [30], as shown in Figure 2.6. The gain of the BGO phototubes is set so that, for each of the eight signals, the electric noise has the same amplitude; this gain matching is performed to simplify treatment of the anti-Compton shields: in the data flow the eight signals are summed up together, so only one threshold is necessary for the veto purpose of the detectors. For this reason, as it will described in the followings, it is not necessary to calibrate the energy spectra of the BGO. In order to avoid the possibility that a photon strikes the scintillator directly, causing possible random coincidences and then the rejection of good events, a 5 cm thick lead collimator is placed in front of the crystal. Thus, when an event is detect by a BGO in coincidence with an event detected by its HPGe, it means that the photon did not lose all of his energy in the germanium detector but scattered

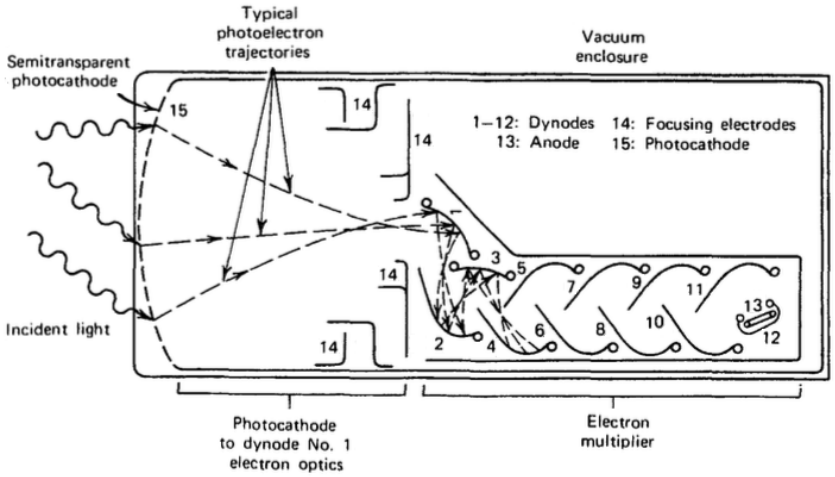

Figure 2.5.: A schematic view of a photomultiplier coupled with a scintillator. The radiation impinges on the photocathode and is then amplified through a series of dynodes. The electrons produced in the process are then collected in the anodes and form the signal. Figure adapted from [28].

outside the crystal. This imply that the event detected by the HPGe does not contain the complete information on the energy of the photon, but part of it is lost in the BGO. Events like this entail an incorrect estimation of the energy and for this reason must be discarded.

The usage of the anti-Compton shielding affects the geometric efficiency of the array, since the presence of the BGOs limits the solid angle coverage. However, the great advantage of this procedure is that the Peak to Total (P/T) ratio increase of about 50%. The effect of the BGOs on the analysis will be further explained in Chapter 3.

Figure 2.6.: Pictures of a GALILEO anti-Compton shield. In the images just the phototubes of the crystals are visible, while the detectors are inside the structure.

2.2.3. GALILEO phase II

A new phase of GALILEO is under realization with the aim of increasing the efficiency by covering a larger solid angle [31]. The second phase will consist in 10 triple cluster detectors (GTC) and their anti-Compton shield, using 30 HPGe and 90 BGO crystals from the EUROBALL array.

Since the disposition of the GTC may strongly influence the future experiments, two possible configurations have been studied via GEANT4 Montecarlo simulations and the GTC. The schematic drawing of the two configurations are shown in Figure 2.7.

One possibility is to replace the 90° ring of single crystal detectors with ten GTC: according to the simulation the GTC should not be distributed in a single ring but in two (at 83° and 97°), maximizing the overall efficiency. The gain in efficiency would be of 66% with respect to the previous phase.

The second possibility is to dispose 10 GTC at backward angles and, to avoid the collision of the anti-Compton shields with the beam line, the detectors should be taken 10 mm further away from the center of the chamber. The 15 single detectors will be disposed at forward angles. With this configuration the efficiency would increase from 2.4% to about 6.5% [32]. This geometry would benefit lifetime measurements via Recoil Distance Doppler Shift (RDDS) method with the GALILEO plunger by improving the efficiency at backward angles and also allowing the coupling of the array with ancillary detectors. The latter possibility has been chosen [32] and it is going to be under construction for the end of 2018.

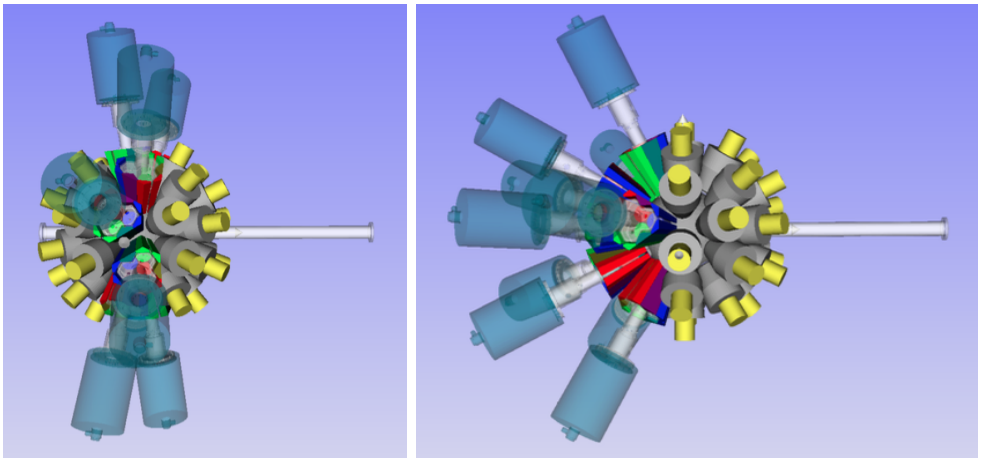

Figure 2.7.: 3D visualization of a possible GALILEO phase II. On the left, the 30 Compton-suppressed single crystals and the 10 GTC and their anti-Compton shield are well visible. On the right, the 25 Compton-suppressed single crystals placed at 90° and forward and the 10 GTC placed backward are well visible. Figure taken from [31]

2.3. Neutron Wall

Neutron Wall (NW) [33, 34], originally built for EUROBALL, is an ancillary detector of GALILEO and is composed of liquid scintillator detectors, set at forward angle with respect to the beam direction at a distance of 510 mm from the target. The array is formed of 15 pseudohexaconical detector units placed in two ring and a central pentagonal unit. The hexagonals units are divided into three hermetically separated segments, each viewed by a 130 mm diameter Philips XP4512 photomultiplier, while the pentagonal unit is divided into five segments, each coupled with a 75 mm Philips XP4312B photomultiplier, for a total of 50 detectors, each of them filled with Bicron BC501A liquid scintillator. The pentagonal unit was not present in the asset of NW in LNL due to the presence of the beam dump. The structure of Neutron Wall is presented in Figure 2.8.

Liquid scintillators are produced by dissolving an organic scintillator in a solvent [28]. The scintillation process in organic scintillators arise from transitions in the energy level structure of a single molecule. The incident radiation excites the electrons of the material that, during the de-excitation process, emits photons that are subsequently converted into an electrical signal by the photomultiplier.

Each detected event is tagged using three different parameters: the Time of Flight (TOF), the Zero-Cross-Over (ZCO) and the charge-integrated anode signal (QVC) using analog NIM Bartek modules. The TOF of γ ray and neutrons between the target and the detector segment is determined as the time difference between the constant fraction time (CFD) and the accelerator RF. The ZCO is a parameter used for the distinction of neutrons and γ rays based on the different decay time of the pulse generated by the radiation in the liquid scintillator. The QVC is a parameter proportional to the charge collected by the photomultiplier and it measures the energy deposited in each detector.

The Neutron Wall array has all the leading characteristic of an ancillary detector:

- a total efficiency of $\varepsilon_n = 25 - 30\%$ coming from an intrinsic efficiency for detecting neutrons of ε =50% and a solid angle coverage of $\Omega = 1\pi$, depending on the kinematic of the reaction;
- the possibility of performing a n-γ discrimination using the Zero Cross Over (ZCO) pulse shape and the Time of Flight (TOF) analysis;
- a high granularity;
- a fast timing.

These characteristics make NW a great tool to distinguish between neutrons and photons and to be used as a filter to select the channel of interest. This is the case of the experiments presented in this thesis. The n-γ discrimination procedure will be described in the next section.

Neutron-γ discrimination

The Neutron Wall array allows the distinction of neutrons and photons, thanks to the different pulse shape and the different time of flight of the radiation induced by the interaction. Two characteristics of the signal have been taken into account: the ZCO and the TOF. In the present experiments this discrimination is used to distinguish between fusion-evaporation

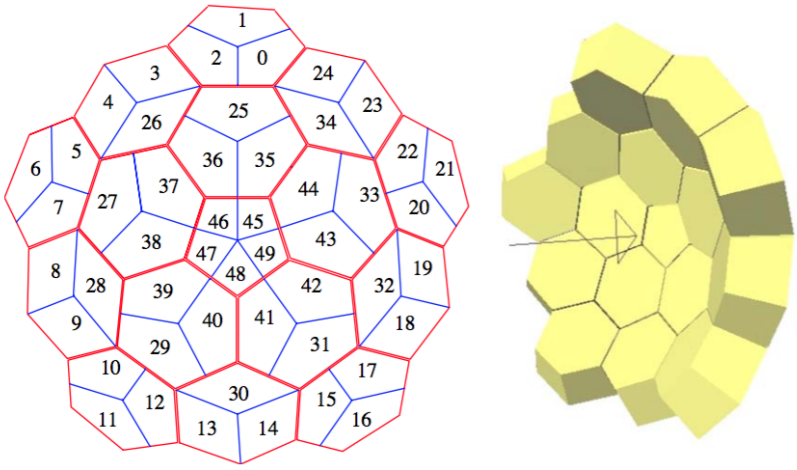

Figure 2.8.: Disposition of the scintillator detectors in the Neutron Wall array. Figure taken from [34].

events, expected to be in coincidence with at least a neutron, and the Coulomb-excitation events due to the beam interaction with the ^{181}Ta degrader and the ^{197}Au plunger stopper. In Figure 2.9 two examples of typical ZCO and TOF spectra are shown. The peak on the right corresponds to γ events, while the peak on the left, that is visibly broader than the former, corresponds to neutron events. The broadening of this second peak is due to the Maxwell-Boltzmann speed distribution of the neutron after many scatterings in the scintillator [29]. The two peaks are well distinguishable in both cases.

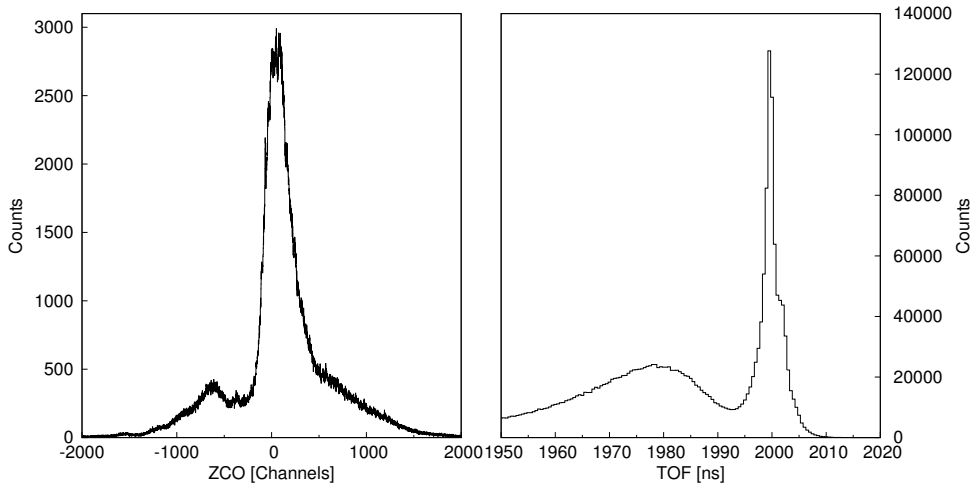

Figure 2.9.: Neutron-gamma discrimination with NW detectors: in the left graphic the ZCO for detector 0; on the right, the TOF for detector 0. On both graphics, the peak on the right corresponds to γ events while the larger peaks, on the left, correspond to neutrons events.

2.4. The Plunger device

The lifetime measurements of ^{188}Hg states are performed via Recoil Distance Doppler-Shift (RDDS) method, that will be further explained in Chapter 4. A fundamental instrument is the plunger device, that allows direct measurements of lifetimes in the range of picoseconds. Many different plunger devices have been developed to be coupled with γ-ray spectrometers. For the GALILEO array, a specific plunger device [35] has been developed in collaboration with the Cologne Institute für Kernphysik (IKP). The needed characteristic of the device are:

- the possibility to vary the distance between the target and the stopper foil from a few micrometers to some tens of millimeters, with sub-micrometric precision;
- the transparency of the device in order to maximize the geometrical efficiency of the apparatus;
- an active feedback system to compensate any changes in the target-stopper distance.

The final design of the GALILEO plunger device is presented in Figure 2.10 and with this configuration a good transparency can be achieved since the ring whose geometrical efficiency is lowered the most is the one at 90°, that is not usable for the RDDS measurement. The sub-micrometer precision ($\sim$ 40 nm) of the target position with respect to the fixed stopper is provided by a high resolution piezoelectric linear drive LPS-24 from Physik Instrumente. The parallelism of the two foils is fundamental for the distance measurement and is adjusted by bringing the two foils to electric contact and correcting it with the dedicated screws. Such delicated procedure, that is performed manually, may introduce an offset on the target-stopper distances, whose wrong evaluation would introduce a systematic error in the lifetime measurement. The calibration and the performances of the GALILEO plunger will be presented in Chapter 3 and 4, respectively.

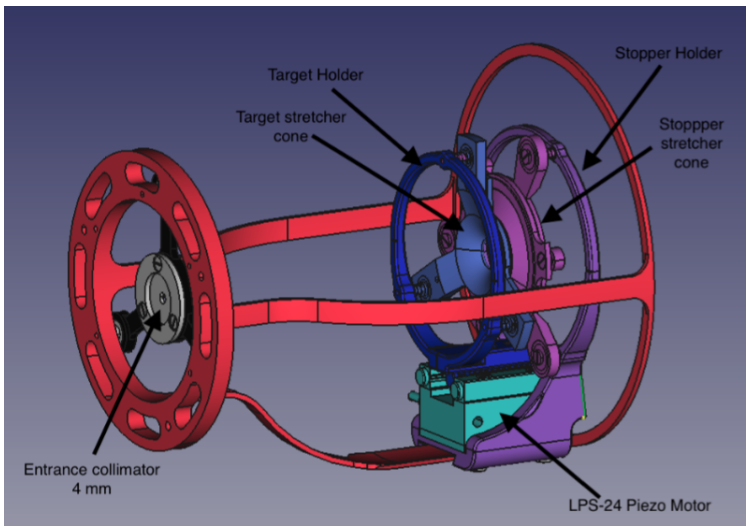

Figure 2.10.: 3D visualisation of the GALILEO plunger device. The stopper and its support are represented in purple, while the target and its support are in blue and are directly mounted on the motor, in light-blue. The mechanical support fixed on the reaction chamber is in red. Figure from [35]

3 Pre-sorting of experimental data

The knowledge of the apparatus is fundamental for a correct analysis of the experimental data. A thorough pre-sorting not only allows the physicist to become familiar with the capabilities of the apparatus and to improve them, but also to know its limitations and to estimate the precision of its measurements. Moreover, when two arrays of detectors are coupled together, as in this case for GALILEO and Neutron Wall (NW), it is necessary not only to calibrate each detector and to align them with each others, but also to align the two arrays, in order to make the in-coincidence measurement feasible.

In this Chapter the pre-sorting of the experimental data is presented, consisting in the energy and efficiency calibration of GALILEO, a systematic study of the Compton suppression, the pile up rejection, the stability check of the HPGe and the time alignment of the detectors. Then, also the calibration of the Time of Flight (TOF) and of the Zero-Cross-Over (ZCO) are performed for all the Neutron Wall detectors.

3.1. GALILEO

The GALILEO array counts 25 Compton-suppressed HPGe detectors, each of them with their own characteristics. For a correct and precise analysis a thorough pre-sorting of the data was necessary. In addition, with the implementation of the digital electronic, it is possible to record the trace of the signal, making the pile up rejection feasible.

3.1.1. Energy calibration

In the last decades germanium detectors have been shown to be useful tools for γ-ray spectroscopy. Because of their excellent energy resolution (about 2 keV at 1.3 MeV), they allow the discrimination of transitions very close in energy. For this reason the energy calibration of each detector is fundamental. This procedure allows the conversion of the ADC channels into the real energy (in keV), making possible to merge data from different detectors. For the calibration, seven different radioactive γ sources have been used, as presented in Table 3.1. The covered energy range is between 81 and 1836 keV, which is larger than the region of interest for the experiment.

In the uncalibrated spectra the full-energy peaks have been identified and their centroid and their distribution have been extracted, assuming that each of them follow a gaussian distribution. An example of spectrum is shown in Figure 3.1, on the left.

Source	Energy range [keV]	Activity (21/07/16) [kBq]
^{60}Co	$1173 - 1332$	327 ± 9
^{137}Cs	661	369 ± 11
^{133}Ba	$81 - 384$	370 ± 11
^{22}Na	$511 - 1274$	286 ± 8
^{54}Mn	835	167 ± 5
^{88}Y	$898 - 1836$	23.8 ± 0.7
^{152}Eu	$122 - 1408$	307 ± 9

Table 3.1.: γ sources used for the GALILEO calibration, showing the energy range of the considered transitions. The activities have been corrected for the day in which the sources have been used for the calibration.

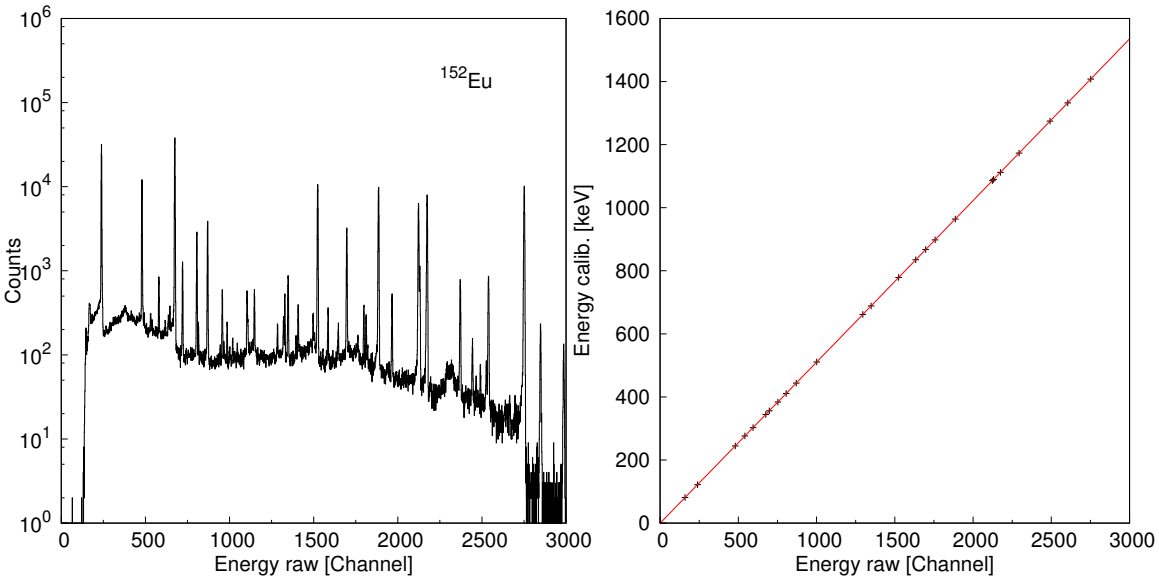

Figure 3.1.: On the left, an example of uncalibrated spectrum of ^{152}Eu for detector SC00. On the right the calibrated energy as a function of the raw energy for detector SC00. The calibration function is a third order polynomial.

By plotting the real energy as a function of the ADC channel position, the calibration function may look like a first-order polynomial (see Figure 3.1, on the right), but a more accurate analysis points out higher-order contributions: the difference between the energy obtained with a linear calibration and the real one has a parabolic-like trend (see Figure 3.2, top-left pannel). The non-linear trend of the energy calibration of the detectors is due to the electronic chain, in particular it is mainly caused by the pre-amplificators [36].

In order to investigate such non-linearities in the energy calibration and improve the final result, a systematic study of the calibration is made by using different polynomials up to the sixth order; then for each detector the calibration function is chosen by minimising the residuals dispersion and by paying attention to the residuals trend. In Figure 3.2 this

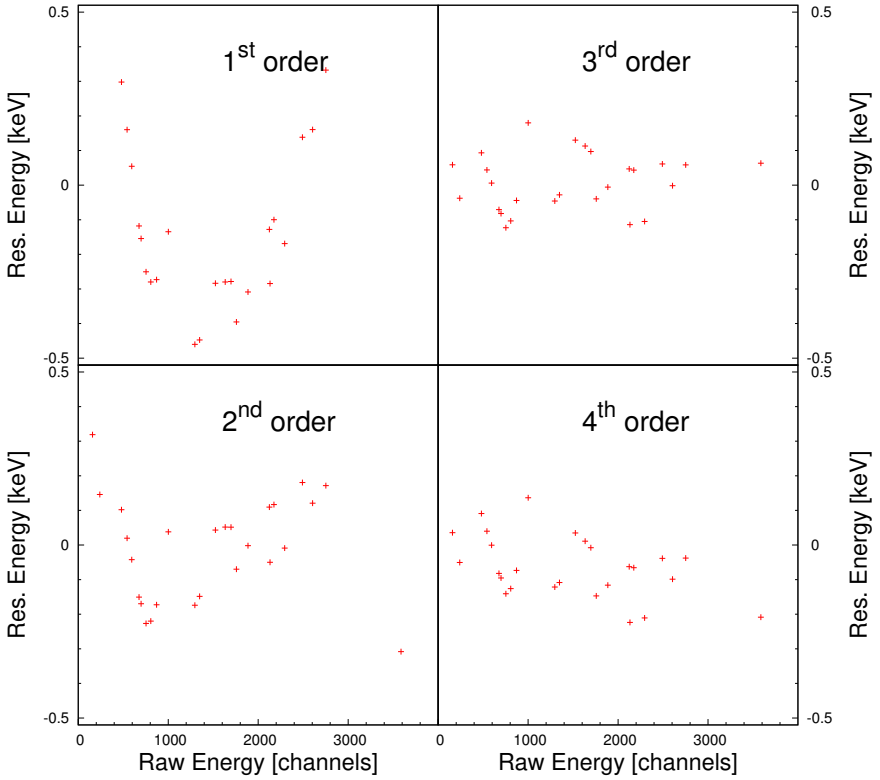

Figure 3.2.: Energy calibration of the GALILEO detector SC00 by using different polynomial functions: in each pad the difference between the calibrated and the real energy as function of the ADC channel for the differential polynomial orders. For polynomial order equal to 1 and 2 a trend is clearly visible, while it seems disappearing for high order polynomials.

procedure is shown for the detector SC00, presenting for each order of the calibration function the residuals $E_{cal} - E_{real}$. In this case the polynomial chosen has been the third-order: the trend that can be seen in the first two polynomial disappears in the third; also the spread of the residuals saturates with the third order polynomial and the fourth polynomial does not present any improvement. For these reasons, for most of the detectors the third-order polynomial appeared to be the best option.

Resolution

One of the dominant characteristic of HPGe detectors is their excellent energy resolution when applied to γ-spectroscopy, especially compared to the resolution of scintillators. The resolution is evaluated through the measurement of the full width at half maximum (FWHM) of the peaks. The FWHM for HPGe is usually between $0.8-1.2$ keV at 122 keV and $1.7-2.3$ at 1333 keV [28].

From experimental data, the energy resolution of GALILEO detectors is expected to be about 2.4 keV at 1332 keV, and its energy dependence can be express in function of the γ-ray energy E_γ via the following empirical expression

$$FWHM = \sqrt{a + bE_\gamma + cE_\gamma^2}\,, \tag{3.1}$$

with a, b, c fitting parameters. After the energy calibration of GALILEO detectors, the trend of the energy resolution has been investigated. For the study six γ sources have been used, reported in Table 3.1 (except for the ^{88}Y). The relation between the FWHM and the energy of the detected γ ray is shown in Figure 3.3. From the interpolation of the experimental data with the function of Eq. (3.1) the fitting parameters result to be $a = 0.449 \pm 0.001$, $b = (5.0 \pm 0.4) \times 10^{-4}$, $c = (-8.1 \pm 2.4) \times 10^{-9}$.

This parametrization allows the estimation of the expected FWHM for the peaks. This will be useful during the data analysis in order to better measure the the area of the stopped peaks, that will be a fundamental part of the RDDS method.

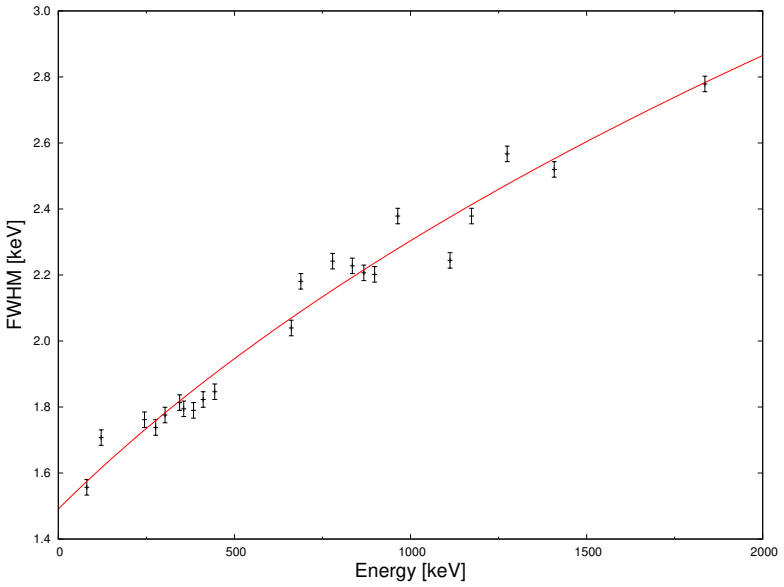

Figure 3.3.: Full Width at Half Maximum (FWHM) of the HPGe detectors as a function of the γ-ray energy. The experimental data has been interpolated (red curve) with Eq. (3.1)

.

3.1.2. Efficiency

Germanium detectors efficiency is highly dependent on the energy of the detected γ-ray. The region in which they are most efficient is usually around 200-300 keV, while their performances worsen at high energy because the probability that a photon escapes the crystal without losing its entire energy is larger [28]. In addition, in order to reduce the counting rate coming from the X-rays mostly due to the Ta target fronting and the Au stopper, 400 μm thick absorbers (200 μm of tin and 200 μm of brass) were placed in front of the GALILEO detectors.

Seven different sources are used for the calibration and a normalization is necessary for a correct estimation of the efficiency. In fact, since the absolute photopeak efficiency is defined as the ratio between the observed events and the emitted γ rays, it is calculated via

$$\varepsilon(E_\gamma) = \frac{I(E_\gamma)}{BR(E_\gamma) \times A \times \Delta t}\,, \tag{3.2}$$

where $I(E_\gamma)$ is the integral of the full-energy peak, obtained via gaussian fit, $BR(E_\gamma)$ is the branching ratio of the transition, A is the activity of the source (see Table 3.1), and Δt is the real time of the acquisition run. The efficiency calibration was performed for each ring and then for the total number of detectors, confirming the previous results.

Many possible functions have been suggested to estimate the efficiency [37], each of them valid for a specific range. Considering the γ-ray energy range of the used radioactive sources, two functions seemed to be more suitable for the purpose: on one side the Radware function [38], that is defined as

$$ln\varepsilon = \left\{ \left[A + B\, ln\frac{E}{100keV} \right]^{-F} + \left[C + D\, ln\frac{E}{1MeV} + E\, ln\frac{E}{1MeV} \right]^{-F} \right\}^{-1/F} \tag{3.3}$$

where A, B, C, D, E, F are free parameters; on the other, the Fazekas function [39] that is written as

$$ln\varepsilon = \sum_i a_i (lnE)^{i-1} \tag{3.4}$$

with $i = 1 - 9$ and a_i as free parameters. The experimental data is fitted with the two functions, using different degrees of the polinomial for the Fazekas function. In particular, in Figure 3.4 the Radware and the fourth-order Fazekas functions are compared. The Radware function seems to fit accurately the experimental data, in particular the low-energy peak, while the fourth-order Fazekas function fails to reproduce that region, even at higher order; such a different trend is due to the fact that in Eq. (3.3) Radware function treat separately the contributions from low- and high-energy gamma rays. On the other hand, we have to highlight that for the energy of the gamma-ray transitions of interest the two functions gives similar results.

3.2. Compton Suppression

As already introduced in Chapter 2, the use of the bismuth germanate scintillators (BGO) as an anti-Compton shield is fundamental to increase the Peak-To-Total (P/T) ratio of the final spectrum. If the BGO detects events with an amplitude above a certain threshold, it means that the photon did not lose all of its energy inside the HPGe: these events must be

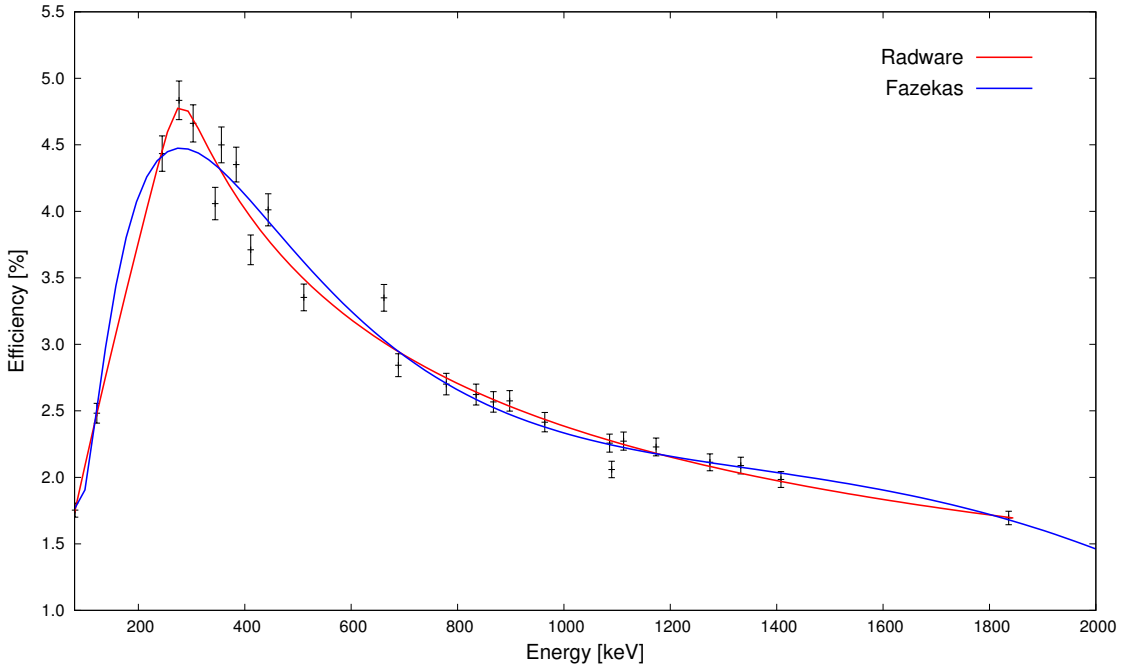

Figure 3.4.: Absolute γ ray detection efficiency as a function of the radiation energy for all GALILEO detectors. The experimental points are fitted with Radware [38] (in red) and Fazekas [39] (in blue) functions.

discarded to improve the quality of the γ-ray energy spectrum. For this reason the choice of the threshold for the Compton suppression is very important: on one hand, a too selective threshold would reject also good events, reducing the statistics; on the other hand, a too permissive threshold would reduce the peak-to-total (P/T) ratio, avoiding the identification of rarer channels which would be overwhelmed by the Compton scattering background of higher energy transitions. Figure 3.5 shows the events seen by the HPGe SC00 and its anti-Compton shield within a coincidence time windows of 20 ns. The energies are reported in channels, since this procedure was performed before the calibration.

To correctly choose the threshold, a systematic study about the effects of the Compton suppression on the P/T ratio and on the efficiency is performed using three sources (^{60}Co at 1332 keV, ^{137}Cs at 661 keV and ^{152}Eu at 121 keV). For each detector a matrix similar to Figure 3.6 was created, a specific macro was then used to project the HPGe events depending on the energy of the BGO and finally calculate the integral of the chosen peak. As an example of such investigation, the trend of the absolute efficiency is reported in Figure 3.6 for three different energies: for high values of the Compton-suppression threshold the efficiency reach a plateau; while for a BGO energy lower than about 50 ADC channels (approximately 10 keV) the absolute efficiency rapidly drops because good events have been discarded. Individual thresholds were set for each HPGe detectors in order to have a good compromise between efficiency and P/T at low energy.

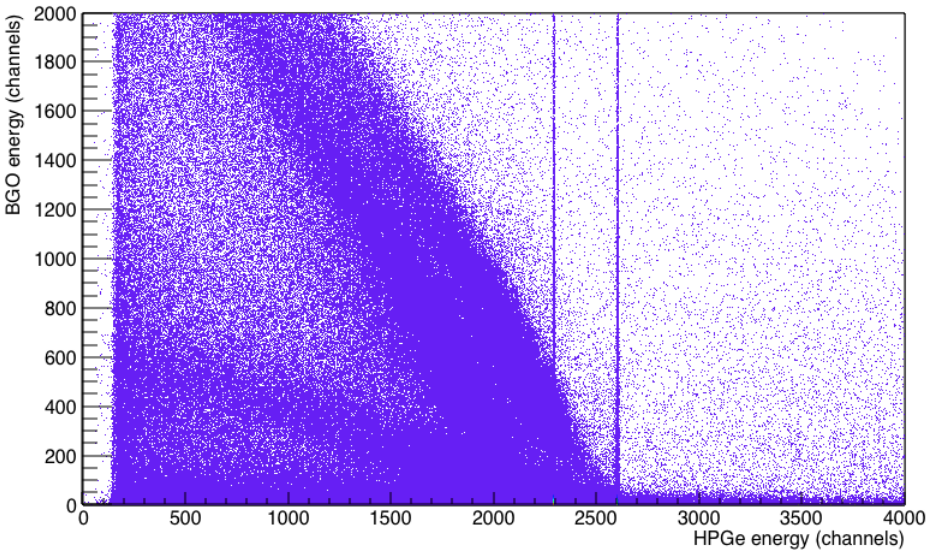

Figure 3.5.: γ-ray energy observed by BGO anti-Compton shields as a function of the energy detected by SC00 detector for the ^{60}Co source. The vertical lines at about 2300 and 2600 channels correspond to random coincidences , while the diagonal lines correspond to the Compton edge of the ^{60}Co source. The energy are reported in channel because this procedure was performed before the energy calibration.

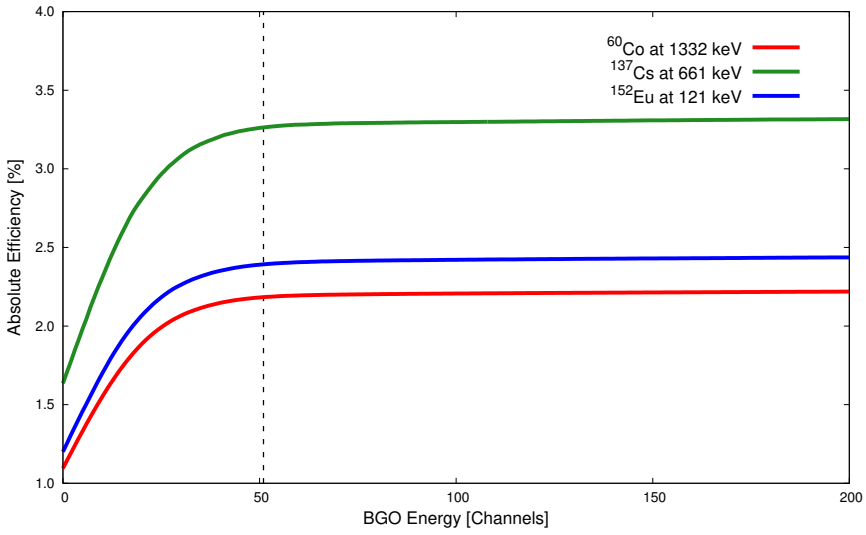

Figure 3.6.: Absolute efficiency of the HPGe as a function of BGO energy threshold. The vertical line represents the chosen threshold, set at 51 ADC channels.

3.3. Pile up rejection

A very important feature for a detector is the response time, which is the time that the detector takes to form the signal after the radiation detection. If the formed signal has a sharp pulse and the rising time of the signal is small (in the range of ns), the detector is considered to have a good timing [40]. Another important characteristic is the duration of the signal: in this period another event cannot be accepted because either the detector is insensitive or the second signal would pile up to the first, leading to an overestimation of the energy.

In this experiment, thanks to the digital electronics, it was possible to record a portion of the triggering signals, called *short trace*, and to discriminate between single events and pile-up events. To do so, the energy extracted from the full signal in the electronic, called *long trace*, was compared to the one extracted off-line from the short trace: if the energy of the long trace is higher than the short trace energy it means that another radiation entered the crystal during the acquisition time. Two matrices of the short trace as a function of long trace are presented in Figure 3.7, showing the events acquired with a ^{60}Co source and in-beam events. In principle, the two energy should be proportional, meaning that no other events arrived during the acquisition window. However, if the energy measured with the long trace deviates for the one extracted from the short traces, it means that another event piled up to the first, leading to an overestimation of the energy. A threshold is chosen to discard those events.

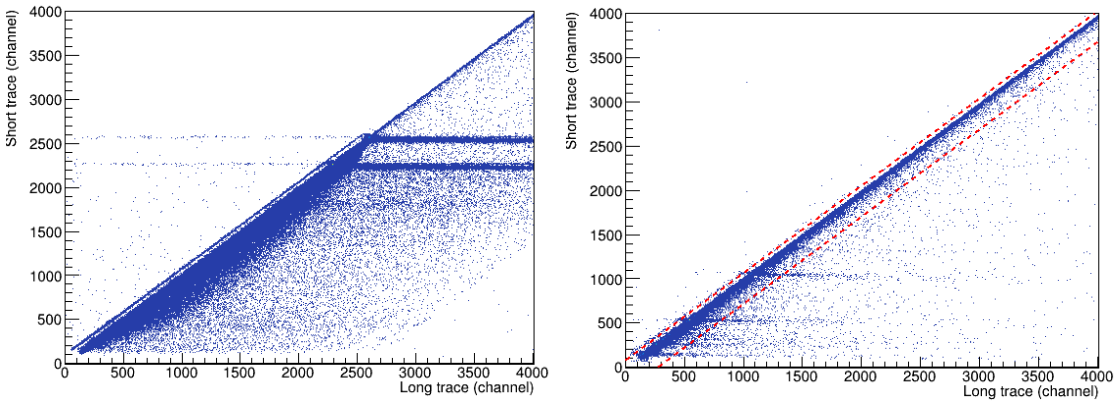

Figure 3.7.: On the left, the comparison between the long trace and the short trace of the signal for detector SC00 for a calibration run with a ^{60}Co source, with a rate of about 2000 Hz per detector. The horizontal lines correspond to random coincidence with the ^{60}Co transitions. On the right the same graphic for a beam run, at a rate between 3000 and 5000 Hz. The red lines represent the threshold chosen for the acceptance window of the events.

3.4. Stability of the HPGe

For lifetime measurements, it is necessary to compare different runs and any variation of the calibration may affect the relative intensity of each component of the γ-ray transitions. Thus any modifications in the electronics of the apparatus or in other external factors (e.g. temperature, humidity, etc.) could have affected the stability of the HPGe signals [40].

In order to verify the stability, three peaks have been chosen in the γ-ray energy spectrum, corresponding to γ-ray transitions of ^{181}Ta (136 keV) and ^{197}Au (279 keV and 576 keV). These peaks have been chosen because of their large statistics, which do not require any additional selectivity conditions, and because they were positioned at the beginning, middle and end of the energy region of interest. Then, a dedicated program fits the peaks for each run and each detector, and measures the centroids position in ADC channels. The results for detector SC00 are presented in Figure 3.8, showing the residuals with respect to the centroids average. What one can deduce is that HPGe detectors remain stable in an interval of 1 channel ($\sim$0.5 keV) for low energy, 0.25 channel ($\sim$0.12 keV) for medium-high energy and about 0.5 channel ($\sim$0.25 keV) at higher energy. The cause of such variations is mainly due to the HPGe detectors preamplifiers which seems really sensitive to the external conditions [36].

3.5. Time alignment

Considering the high γ-ray multiplicity given by fusion-evaporation reactions, the coincidence analysis is crucial for the lifetime measurement. For this reason the time alignment of the HPGe is necessary. To align the detectors a dedicated program was used; this program projects the time difference between the detector SC00 and each detector domain and then perform a gaussian fit to determine the centroid position. Then every detector is shifted in time of the value of the centroid. Figure 3.9 shows the time difference between the SC00 and each detector timing before and after the alignment.

In this experiment, Neutron Wall is used to tag neutrons: in fact, the events of interest in this experiment are from a fusion-evaporation reaction and are expected to be in coincidence with at least a neutron. To correctly select the channel of interest, the two apparatus must be aligned. The same procedure used for the HPGe is applied to the Neutron Wall detectors in order to center the time difference between GALILEO and Neutron Wall to zero.

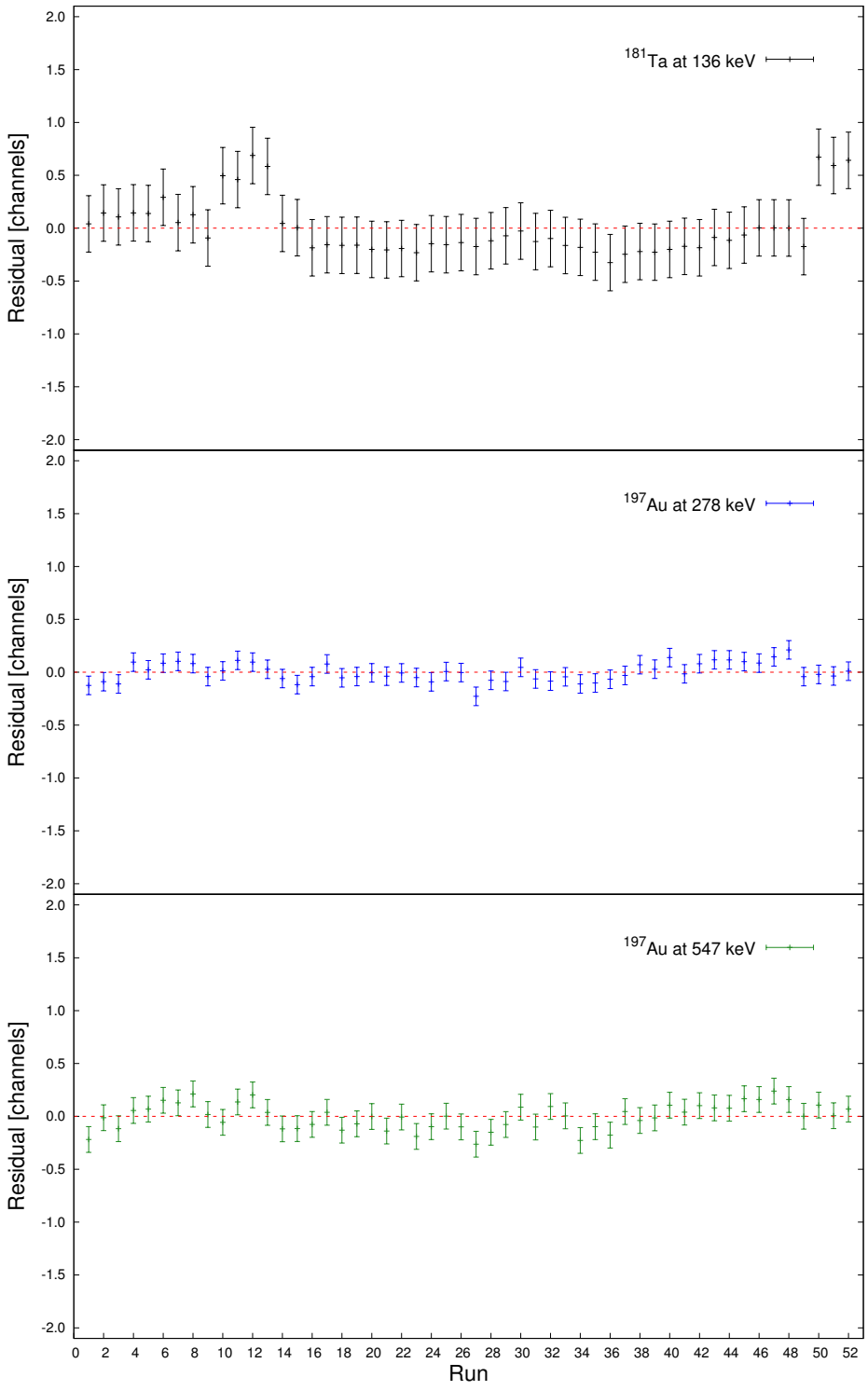

Figure 3.8.: Residuals from the average value of the three selected peaks, originating from the Coulomb excitation and in the region of interest for detector SC00. The peaks energy and their origin are indicated on the figure.

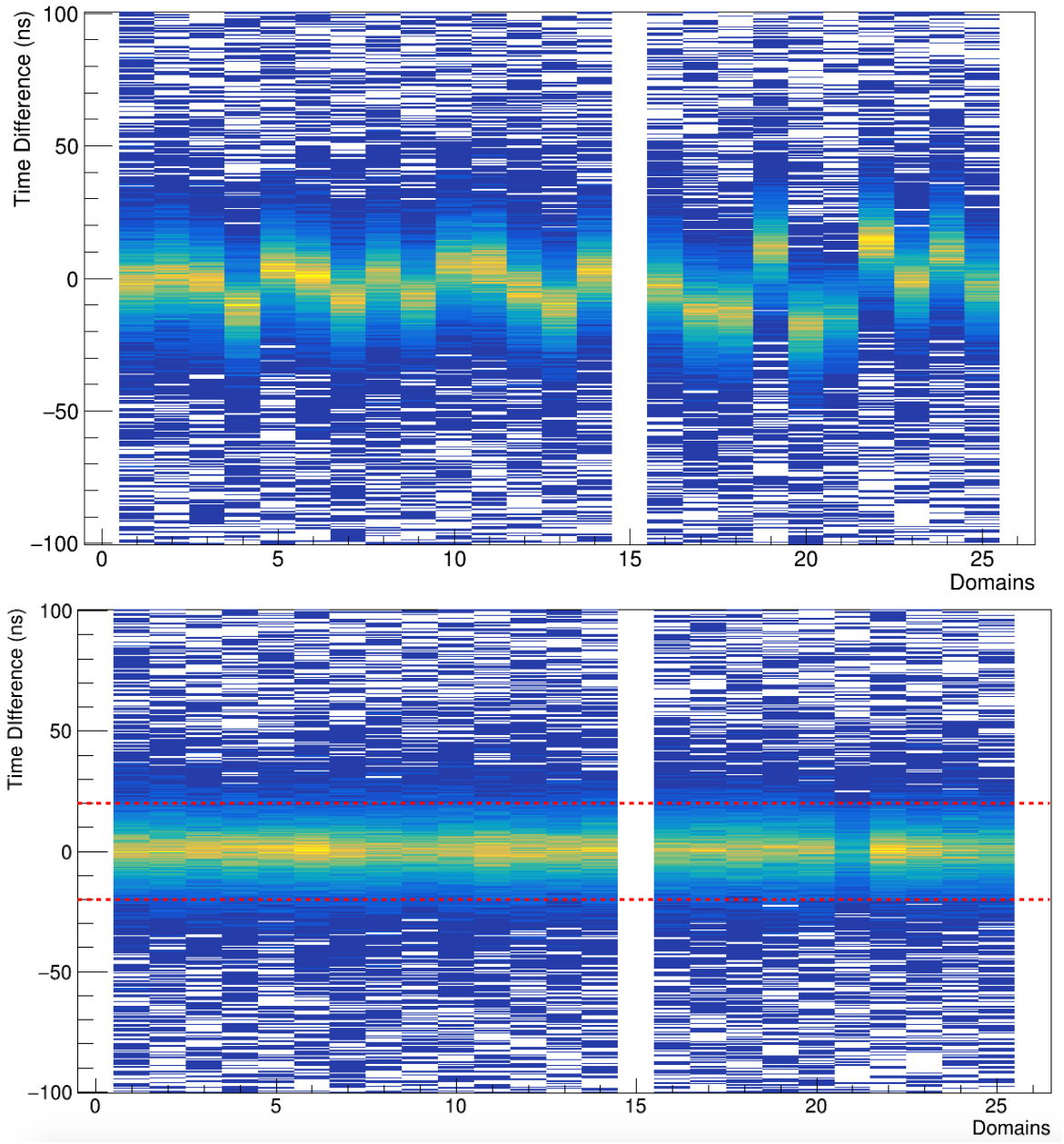

Figure 3.9.: On the top the time difference between the SC00 and each GALILEO detector (also called domains), before the alignment. On the bottom, the time difference after the alignment. The red line represents the coincidence window, set at 20 nm for this experiment.

3.6. Neutron Wall calibration

The discrimination between photons and neutrons is based on two characteristics: the Time of Flight (TOF) of the particles and the Zero-Cross-Over (ZCO). These two characteristic are very different for photons and neutrons and allow the distinction of the two different radiations.

Every detector has a different conversion from voltage to the ADC channels, so a calibration is necessary to compare data from different detectors. The calibration has to be done both for the TOF and for the ZCO, the two quantities of interest already described in Chapter 2. For the calibration, the peak corresponding to the photon is chosen, due to the fact that the γ peak has more statistics and is more distinguishable. The TOF and the ZCO of the photon have been aligned at 2000 ns and at 0 channel respectively. The uncalibrated and calibrated spectra for the TOF and the ZCO are shown is Figure 3.10 and 3.11 respectively.

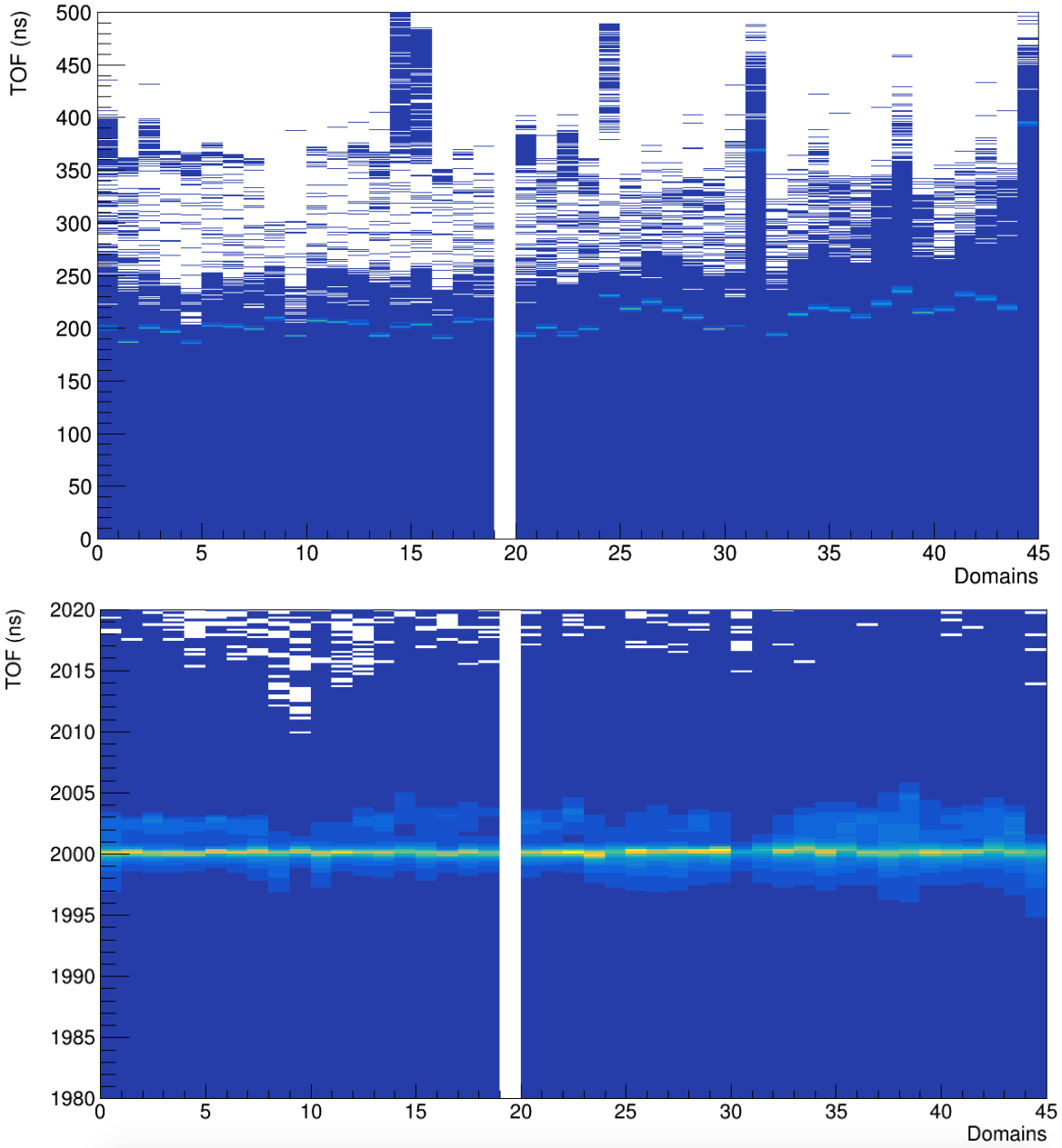

Figure 3.10.: The (top) uncalibrated spectra of the TOF are compared to the (bottom) calibrated spectra. The TOF is aligned at 2000 ns. Detector 19 was not present in the ADC due to electronic problems.

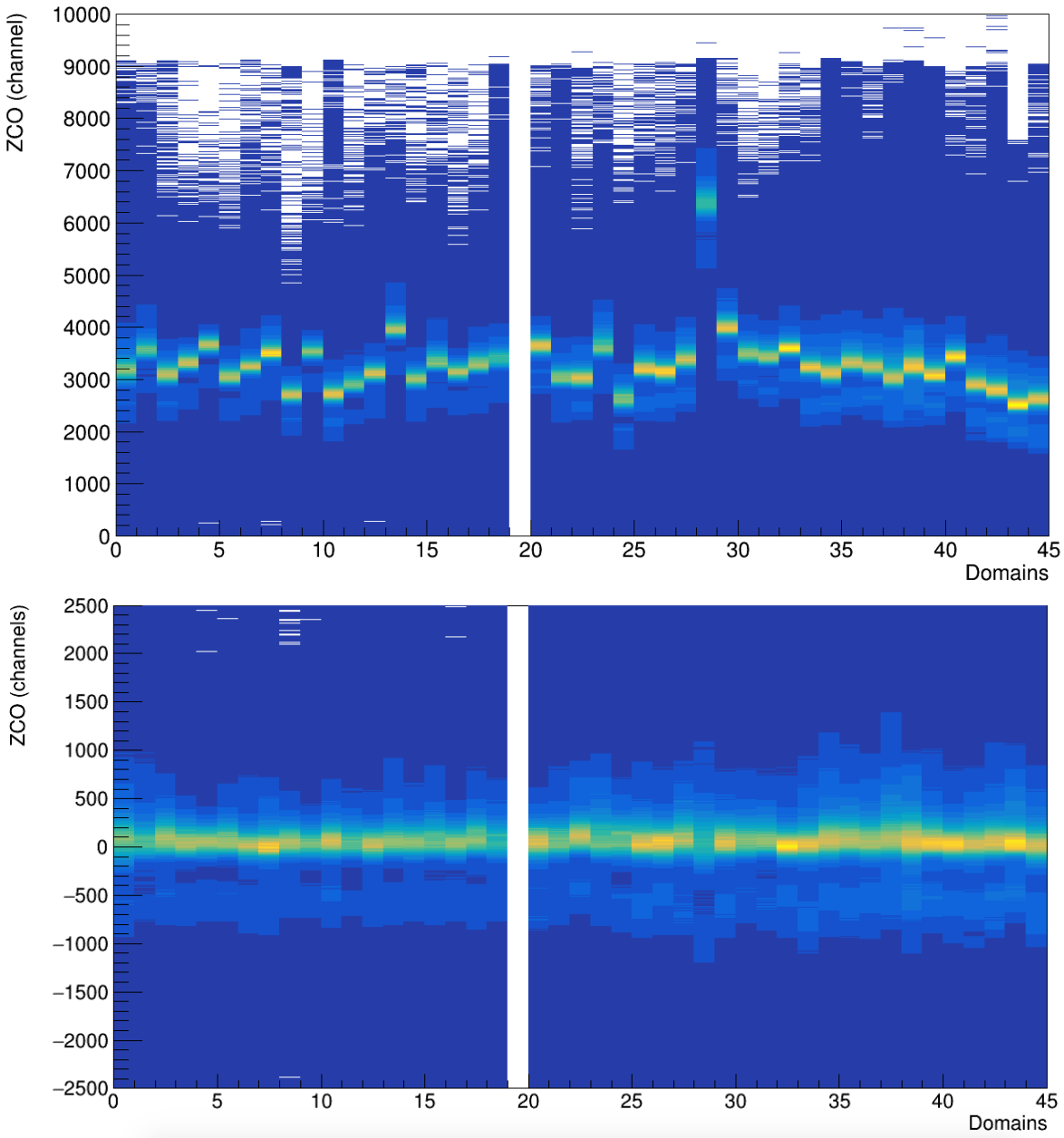

Figure 3.11.: The (top) uncalibratd spectra of the ZCO are compared to the (bottom) calibrated spectra. The ZCO is aligned at 0 channel. Detector 19 was not present in the ADC due to electronic problems.

3.7. The plunger device

The plunger is a fundamental instrument for lifetime measurements with the Recoil Distance Doppler-Shift (RDDS) method, that will be introduced in the next chapter. In the analysis, two different methods will be used for extracting the lifetime of the excited states: the Decay Curve Method (DCM) and the Differential Decay Curve Method (DDCM), and both will be further explained in Chapter 4. The main difference between these two methods is that, while the DCM depends on the real distance between the target and the stopper, the DDCM depends just on the relative distances between the plunger motor position with respect to an internal reference [41]. To perform the DCM method and to compare the results with those obtained with the DDCM method, a calibration of the plunger is required.

The distance between the two foils is measured using the capacitance method [42]: the target and the stopper work as planar capacitor plates. A pulsed signal with a fixed amplitude ($\sim$5 V) is sent to one of the two foils and the charge induced in the other foil is measured. The measurement is repeated for several target-stopper distances down to the contact point. In this way the charge, and thus the capacitance, are measured. The measurement is performed at several motor positions x, in order to calibrate the feedback system. For small target-stopper distances, the system can be approximated to a planar capacitor, and the charge $Q(x)$ depends on the motor position x via equation

$$Q(x) = C(x)V = \varepsilon_0 \varepsilon_r \frac{A}{x} V \ , \tag{3.5}$$

where ε_0 and ε_r are the dielectric constant in vacuum and the relative permittivity, respectively, A is the area of the foils and V is the voltage of the pulsed signal. The calibration of the plunger is shown on the top of Figure 3.12 for the two experiments.

From this calibration, it is possible to estimate the position of the contact point ($1/Q(x) = 0$) of the two foils by plotting the inverse of the induced charge as a function of the motor position. As shown in the bottom pad of Figure 3.12, the behaviour of data is linear just in a certain region, which is taken into account for the estimation of the offset.

With this procedure, the offset for the two experiments results to be 6 ± 1 μm for the *week 11* experiment and 10.7 ± 0.6 μm for the *week 30* experiment. However, Figure 3.12 shows also a rapid change on the trend of the calibration points while approaching to motor position $x = 0$, as highlighted in the inset. This may be due to the oxidation of the gadolinium side of the target which makes an insulation layer [35]. For this reason, the plunger zero offset will be directly checked with the experimental data in Chapter 4.

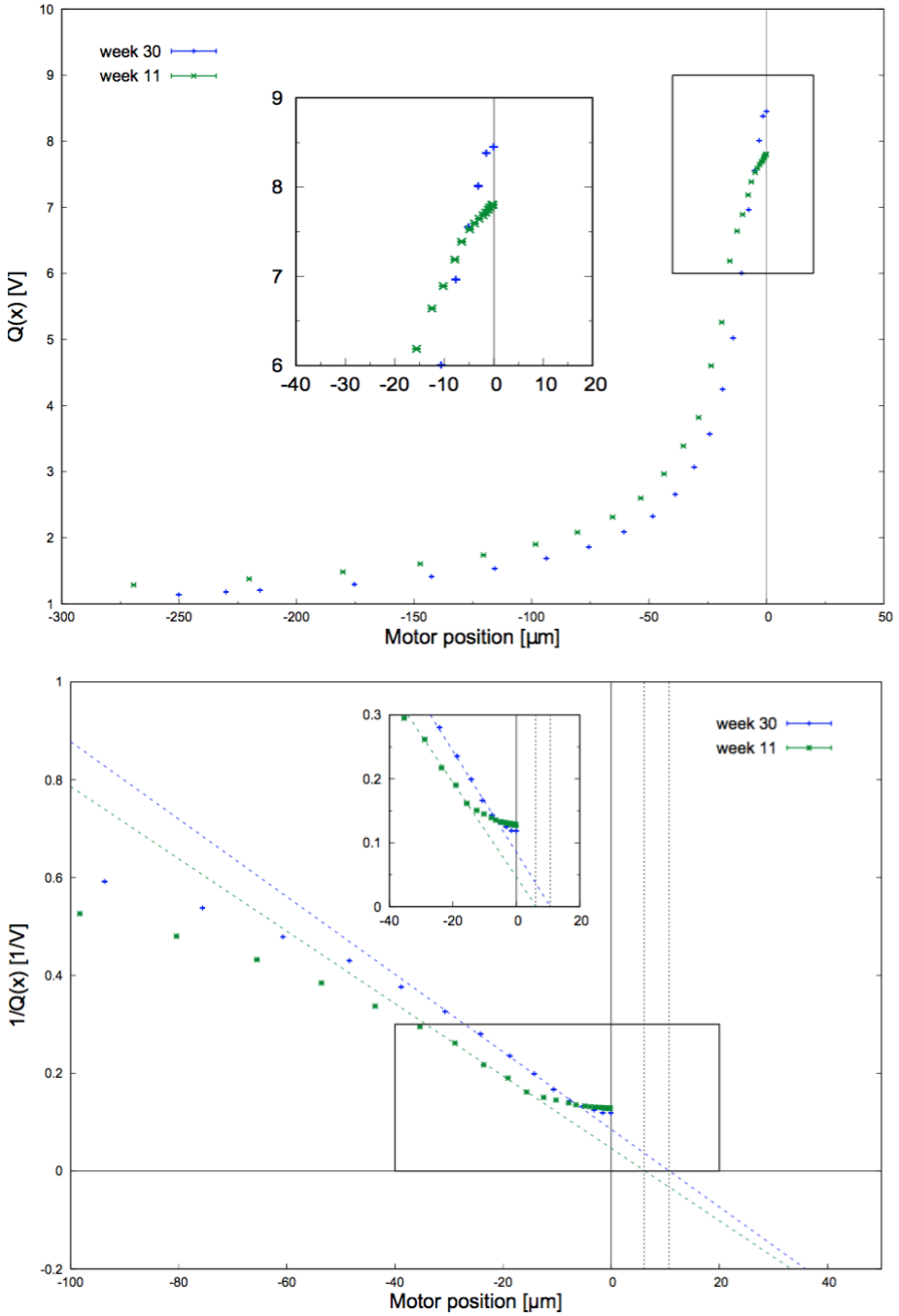

Figure 3.12.: On the top, the charge value depending on the motor position, presenting in blue the data for *week 30* and in green for *week 11*. The calibration procedure is repeated from the region of sensitivity to the contact point. On the bottom, the inverse of the charge value depending on the motor position. The data point for the fit are chosen in the linear region. The non linearity at large distance is due to the non-sensitivity of the region, while at really short distance is due to oxidation of the gadolinium layer.

4 Analysis and Results

Shape coexistence is a well known phenomenon in the neutron-deficient region near and at Z=82. This feature is established for Hg isotopes lighter than ^{188}Hg while it disappears for isotopes heavier than ^{194}Hg; despite theoretical models and experimental fingerprints indicate the absence of such phenomenon for the nuclei between ^{188}Hg and ^{194}Hg, no firm experimental data can exclude the presence of shape coexistence in the intermediary region. For these reasons, in order to shed light on the possible presence of this phenomenon and on the mechanisms at its origin, the lifetime measurement of the first excited levels of the ^{188}Hg is of key importance.

The nucleus of interest has been populated via two different fusion-evaporation reactions and the lifetime measurements were performed via Recoil Distance Doppler Shift (RDDS) technique using the GALILEO plunger device and then analysed via Decay Curve Method (DCM) and Differential Decay Doppler Shift Method (DDCM).

In this chapter, the determination of the ^{188}Hg velocity and the neutron-gamma discrimination are performed, in order to allow the correct identification of the γ-ray transitions of interest and to reduce the probability of contamination. Then the analysis of the $2_1^+ \rightarrow 0_{g.s.}^+$, $4_1^+ \rightarrow 2_1^+$, $6_1^+ \rightarrow 4_1^+$ and $8_1^+ \rightarrow 6_1^+$ transitions of ^{188}Hg and the results are presented.

4.1. Determination of the ^{188}Hg velocity

In a fusion-evaporation (FE) reaction, after the compound nucleus (CN) is created, it starts its de-excitation first by evaporating particles; then the evaporation residue (ER) continues its de-excitation through gamma decay. Considering that for the experiment the plunger device was employed, the photons were emitted either when the ER was still in-flight or while it was stopped in the Au foil [41]. In the first case, the peaks in the energy spectrum face both a Doppler broadening and a Doppler shift according to the equation

$$E_\gamma = E_0 \frac{\sqrt{1-\beta^2}}{1-\beta\cos\theta}\,, \tag{4.1}$$

where E_γ is the detected energy, E_0 is the real energy of the emitted γ ray, β is the ratio between the ER velocity and the speed of light, and θ is the angle between the velocity vector of the nucleus and the direction of the emitted γ ray. Because of the angular momentum

conservation, in FE reactions the ER flies in forward direction at small angles with respect to the beam axis, so in Eq. (4.1) the angle θ can be approximated by the angle of the detectors[1].

Thus, in order to perform the Doppler correction, the evaluation of the velocity of the nucleus of interest in necessary. Moreover, the speed of the recoils is of key importance for the RDDS technique in order to estimate the time of flight between the two foils. The velocity of ^{188}Hg was estimated by observing the relative position of the in-flight (Doppler-shifted) and stopped components of certain transitions. Since GALILEO detectors are placed backwards with respect to the direction of the beam, the $\cos\theta$ is negative and the shifted components of the transitions are expected to be at lower energy E_γ than the stopped E_0. From equation Eq. (4.1) one can deduce the energy shift via

$$\frac{E_\gamma - E_0}{E_0} \approx \beta \cos\theta \ , \tag{4.2}$$

and predict the position of the in-flight peak. The shifted and the stopped components for the $2_1^+ \rightarrow 0_{g.s.}^+$ transition of ^{188}Hg are shown in Figure 4.1 as a function of the GALILEO detectors ring. The stopped component remains at the same energy (412.8 keV) while the shifted component changes depending on the ring and so on the angle of detection.

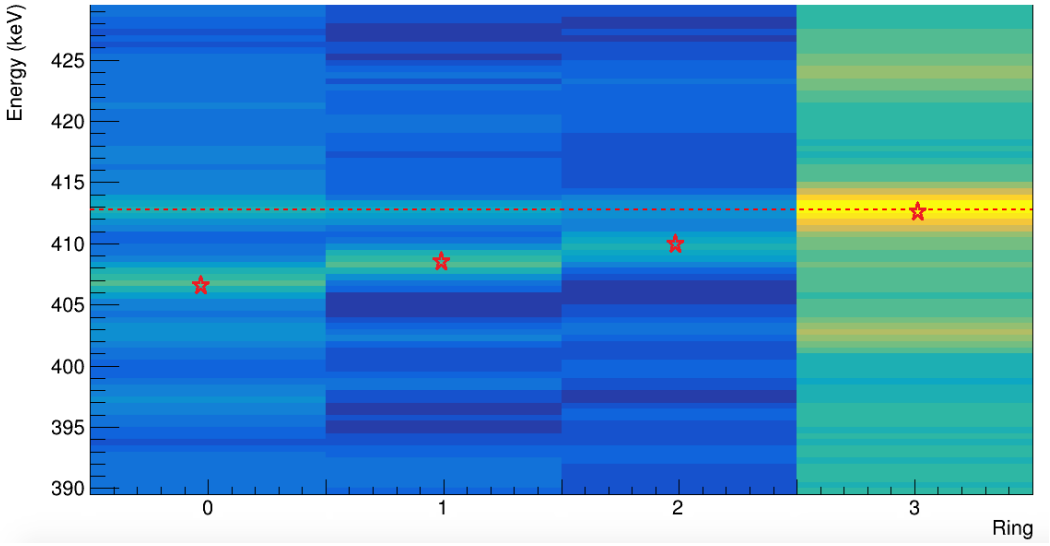

Figure 4.1.: γ-ray energy spectrum depending on the detectors ring. The stopped component (red line) of the $2_1^+ \rightarrow 0_{g.s.}^+$ transition of ^{188}Hg remains at 412.8 keV while the in-flight component (star) changes depending on the angle. In the ring 3, placed at 90°, the in-flight and stopped components coincide.

In order to improve the estimation of the ER velocity, the procedure was performed considering the $2_1^+ \rightarrow 0_{g.s.}^+$, $4_1^+ \rightarrow 2_1^+$, $6_1^+ \rightarrow 4_1^+$ and $8_1^+ \rightarrow 6_1^+$ transitions of ^{188}Hg and then taking into account the average value of the E_γ/E_0 ratio. The resulting E_γ/E_0 ratios for the *week*

[1]For FE reactions, a more precise analysis can be performed using an event-by-event kinematic reconstruction [43] when the EUCLIDES spectrometer is used. The employment of EUCLIDES [44], a 4π array of segmented Si ΔE-E detectors, allows the measurement of the energy and of the angle of the charged particles that are evaporated during the de-excitation process by the CN. Then, by knowing such kinematics information of the evaporated particles, the trajectory of the ER can be determined.

30 dataset are presented in Figure 4.2 as a function of the angle θ. To check the possible deterioration of the target during the experiment, the procedure also was repeated for all the runs. The velocity of ^{188}Hg remains constant for the whole experiment and the measured β are 1.71(8)% for *week 11* and 1.59(1)% for *week 30*.

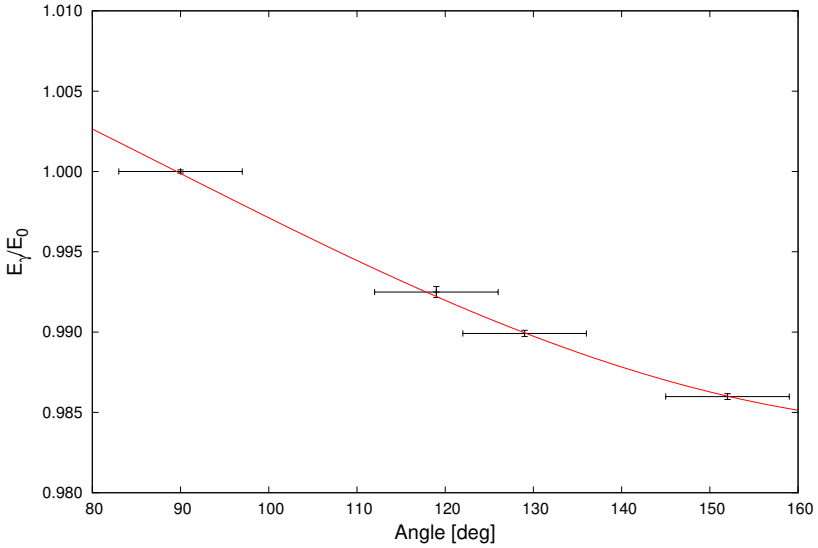

Figure 4.2.: The ratio between in-flight and stopped components of the ^{188}Hg transitions as a function of the HPGe detectors angle. For the estimation of the ^{188}Hg velocity the $2_1^+ \rightarrow 0_{g.s.}^+$, $4_1^+ \rightarrow 2_1^+$, $6_1^+ \rightarrow 4_1^+$ and $8_1^+ \rightarrow 6_1^+$ transitions of the nucleus were taken into account and their ratios were averaged. The error on the angle is referred to the angular diameter of the detectors. The curve represents the fit obtained with Eq. (4.1)

4.2. Neutron-gamma discrimination

As already introduced in Chapter 2, in this experiment the Neutron Wall array has been used to tag the evaporated neutrons in order to discriminate between FE and Coulomb-excitation events and so to select the channel of interest.

With liquid scintillators, as the NW detectors, it is possible to easily distinguish between photons and neutrons using two characteristics: the Time of Flight (TOF) and the Zero-Crossover (ZCO). In Figure 4.3 a ZCO versus TOF matrix is shown for all NW detectors. The black and red polygons represent two possible gates for the selection of the channel of interest: the red one, the largest, leads to a higher statistics but it includes many γ-ray events; the black one is more restrictive and so it entails a cleaner spectrum. In order to reduce possible contaminations which may introduce systematic errors, the second one has been chosen.

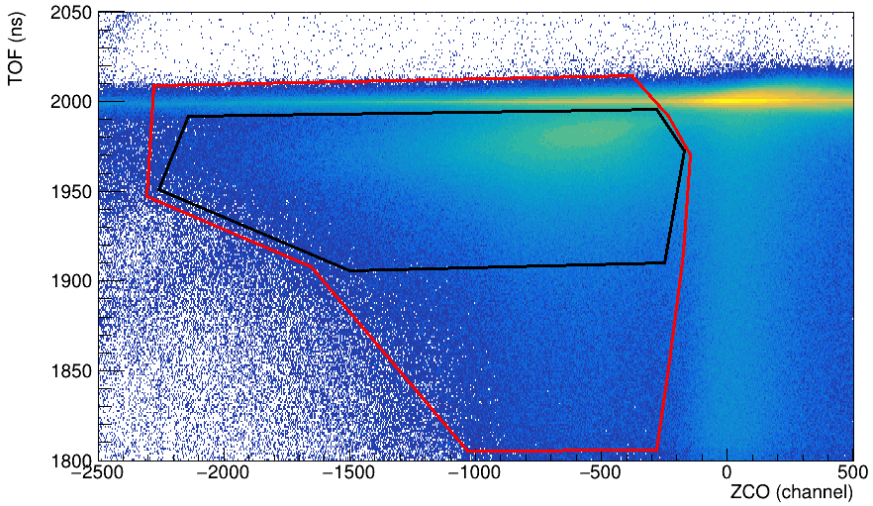

Figure 4.3.: ZCO versus TOF matrix. The red and the black polygons represent two possible cuts to optimise the selection of the channel of interest. The black one was chosen in order to obtain a cleaner spectrum.

In Figure 4.4 the effect of the neutrons selection on the γ spectrum is shown. The events due to the Coulomb excitation of ^{181}Ta and ^{197}Au are strongly suppressed, much more than those due to fusion-evaporation leading to ^{188}Hg. In particular, one can notice that the transition of ^{181}Ta at 415 keV is very close in energy to the ^{188}Hg transition at 412 keV, which corresponds to the $2_1^+ \rightarrow 0_{gs}^+$, and covers it. Thanks to the powerful selection capabilities of the apparatus, the transitions of ^{188}Hg become visible, making the in-coincidence analysis feasible.

4.3. The RDDS method

The Recoil Distance Doppler Shift (RDDS) method is a well established experimental techniques in nuclear γ-ray spectroscopy for measuring the lifetime of excited nuclear states in the range of picoseconds [41]. One of the main characteristics of this method is that lifetimes are deduced directly from measured quantities and the estimations are model independent.

In a fusion-evaporation reaction, as in the present experiment, the compound nucleus is populated after the beam interacts in the target and then, due to the momentum transferred, it leaves the target with a velocity v to finally stop in a foil at a defined distance x from the target. The distance can be changed using the plunger device. A schematic description of this procedure is shown in Figure 4.5. The radiation emitted by the excited nucleus during the flight is Doppler-shifted depending on the velocity of the nucleus and on the angle θ where the γ-ray detector is positioned, as in Eq. (4.1). This technique results in two different components per each γ-ray transition: one peak is related to the γ rays emitted in flight, while the second is due to those emitted by the nucleus stopped in the Au foil. The relative intensity of the in-flight peak (I_{if}) and the stopped one (I_s) is related to the probability that the nucleus decays during the flight or after the nucleus stop in the foil. From the integral of

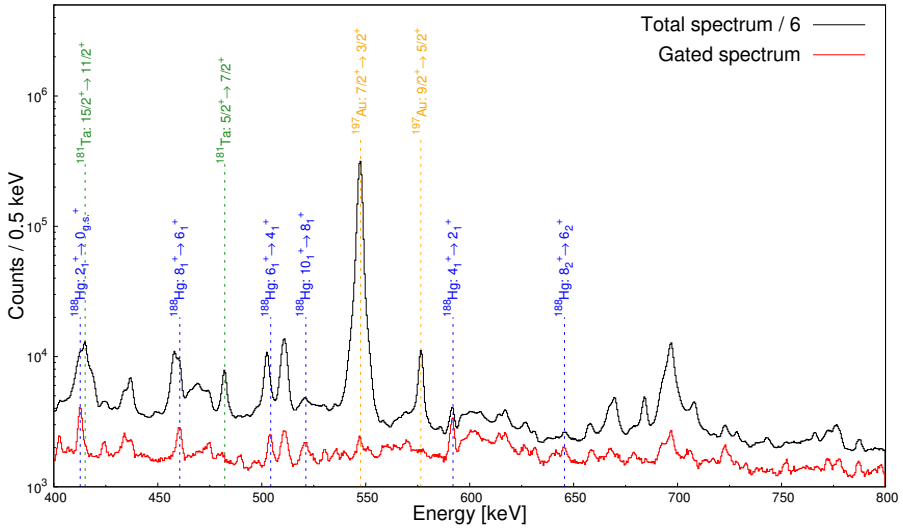

Figure 4.4.: Effect of the neutrons gate on the γ-ray energy spectrum. In black the spectrum without any condition has been normalized in order to be comparable with the other. In red the gated spectrum with the condition of being in coincidence with at least a neutron. In the latter, the statistics is considerably reduced but peaks corresponding to ^{188}Hg transitions are more visible and the events related to the Coulomb excitation of the target and stopper are drastically reduced. Taken from [45].

the two components one can define the *decay curve* [41]

$$R(t) = \frac{I_s(t)}{I_s(t) + I_{if}(t)} \tag{4.3}$$

and the *flight curve*

$$F(t) = \frac{I_{if}(t)}{I_s(t) + I_{if}(t)} \tag{4.4}$$

where the sum of the two components works as normalisation[2].

The most common approaches for the analysis of RDDS data are the Decay-Curve Method (DCM) and the Differential Decay-Curve Method (DDCM) that will be further presented.

4.3.1. Decay-Curve Method

In the DCM the experimental data obtained via RDDS technique are fitted with dedicated functions that describe the decay process. Let us consider the case where the level of interest is directly populated by the reaction and has no feeders[3]; the decay curve follows the typical

[2] In principle one can use other normalizations. For example, one can normalize over the number of reactions using the integral of a peak related to Coulomb excitation.

[3] The described case can be used also for measuring lifetime via $\gamma\gamma$-coincidence technique. Such procedure will be used in the followings.

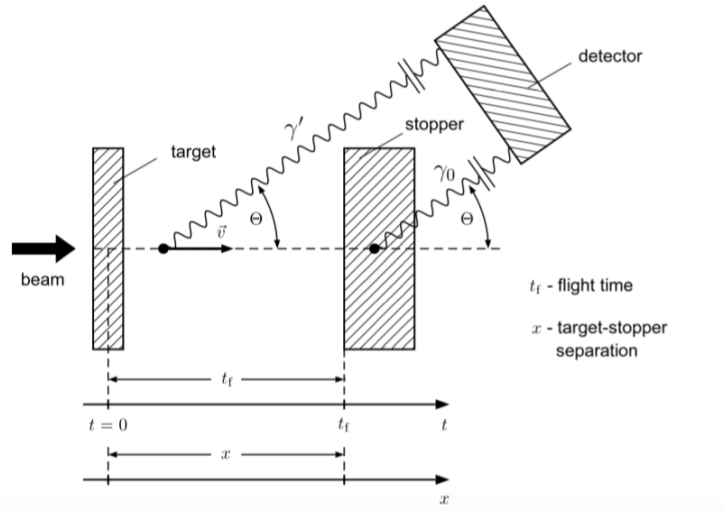

Figure 4.5.: Schematic description of the RDDS method. After the beam interacts in the target, the evaporated fragment leaves the target with a velocity v and then it stops in a foil at a defined distance x from the target. During the flight, the excited nucleus emits γ rays that, when detected, result Doppler-shifted, depending on the velocity v and on the angle θ. After a flight time t_f, the nucleus stops in the plunger stopper and the emitted γ rays are detected at the correct energy. Figure adapted from [41].

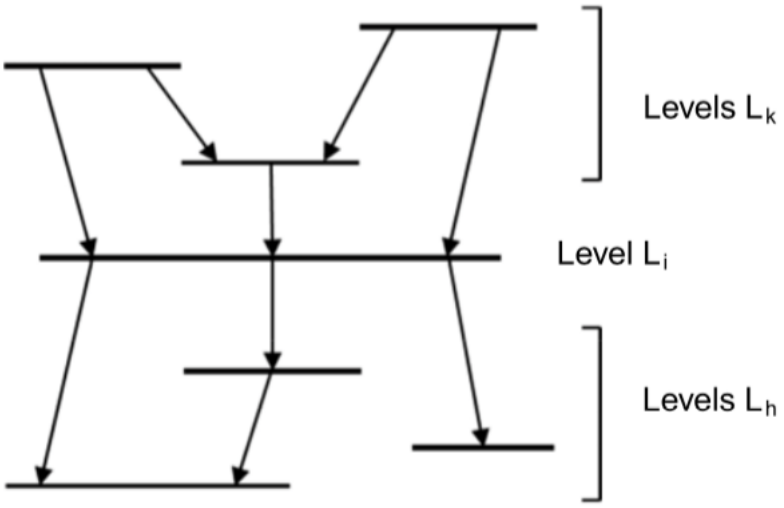

Figure 4.6.: Schematic description of a possible level scheme, describing the complexity of the decay chain. Figure taken from [41].

exponential trend of radioactive decays:

$$R(t) = n(0)e^{-t/\tau}\,, \tag{4.5}$$

where τ is the lifetime of the level and $n(0)$ is its initial population. The lifetime can be deduced by fitting the intensity ratios obtained per each distance with Eq. (4.5) and keeping τ and $n(0)$ as free parameters. In fusion-evaporation reactions (see Appendix B) the higher-spin states are first populated and later they decay to lower-spin states, so the determination of the lifetime requires the solution of a complex system of differential equations

$$\frac{d}{dt}n_i(t) = -\lambda_i \cdot n_i(t) + \sum_{k=i+1}^{N} \lambda_k \cdot n_k(t) \cdot b_{ki}\ , \tag{4.6}$$

where i is referred to the level of interest, k is referred to the feeding level and N is the higher feeding level considered; b_{ki} is the branching ratio of the transition and $\lambda_j = \tau_j^{-1}$ and $n_j(t)$ are the decay constant and the population of the $j-th$ state, respectively. A schematic view of a possible level scheme is presented in Figure 4.6. The solution of the differential problem of Eq. (4.6) is given by the Bateman equation [46]; for a simple case where every state has just one feeder the solution is

$$n_i(t) = \sum_{k=1}^{i} \left[n_k(0) \times \left(\prod_{j=k}^{i-1} \lambda_j \right) \times \left(\sum_{j=k}^{i} \frac{e^{-\lambda_j t}}{\prod_{p=k,p\neq j}(\lambda_p - \lambda_j)} \right) \right]\ . \tag{4.7}$$

In the general case the solution with respect to the decay curve $R_i(t)$ is [41]

$$R_i(t) = P_i e^{\lambda_i t} + \sum_{k=i+1}^{N} M_{ki} \left[\frac{\lambda_i}{\lambda_k} e^{-\lambda_k t} - e^{-\lambda_i t} \right]\ , \tag{4.8}$$

where P_i is the direct-feeding intensity of the level of interest, while M_{ki} are the coefficients that represent the ratio of the decay constants. While fitting the experimental data with the proper decay curve, the knowledge of the absolute target-stopper distance is crucial, so a calibration of the plunger is required (see Chapter 3). A way to get rid of such requirement is the measurement via DDCM, which is not affected by the plunger zero-offset, as explained in the dedicated section.

The determination of the lifetime using the DCM is very complicated and requires not only the knowledge of every possible feeders, but also the decay constant of those levels. The presence of an unknown feeder or the wrong estimation of a decay constant would entail an incorrect estimation of the lifetime of the state of interest. This problem can be easily avoided with $\gamma\gamma$-coincidence measurements.

Coincidence measurement

The $\gamma\gamma$-coincidence measurement consists in gating on a specific feeding level in order to eliminate the contribution from the other feeders, known or unknown, and also to reduce the inclusion of systematic errors. This procedure results particulary efficient when the gate is applied on the level immediately preceding the level of interest, so that no other feeders contribute, reducing the systematical errors [47]. This situation is schematized in Figure

4.7: the level B feeds the state of interest A and every side-feeding are excluded from the determination of the lifetime τ_A. When gating on the in-flight component of the B level

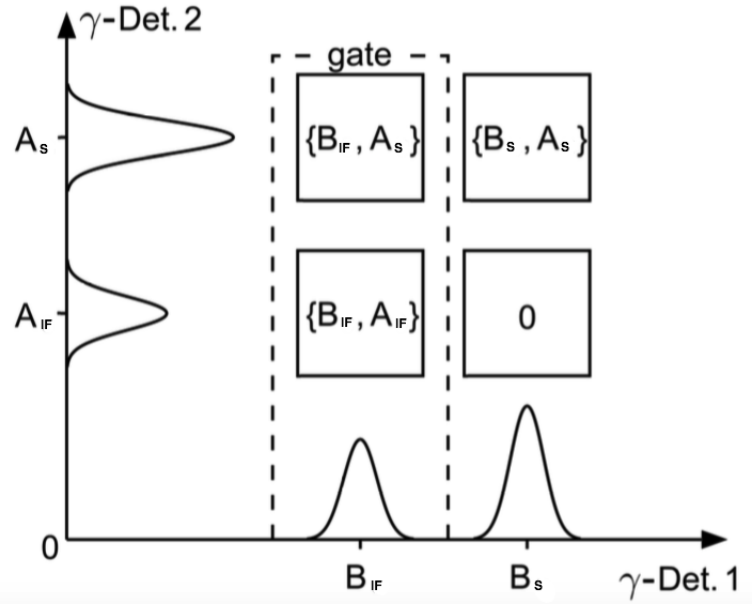

Figure 4.7.: Schematic drawing of an in-coincidence measurement. The gate is performed on the in-flight component B_{IF} of the feeder and then the in-flight A_{IF} and the stopped A_S components of the transition are observed. Figure adapted from [41].

(B_{IF}), two components of the A level are present: the in-flight $\{B_{IF}, A_{IF}\}$ and the stopped $\{B_{IF}, A_S\}$; on the other hand, when gating on the stopped component of the B level (B_S), only the stopped component of the A level is present, $\{B_S, A_S\}$. Indeed, since the decay of the A level follows the decay of the B level, there cannot be an in-flight component of the A level if the decay of the B level happens with the nucleus at rest. Thus, the gate should be preferentially made on the only in-flight component of the B level otherwise there would be an overestimation of the A_S component, introducing a systematic error that leads to an overestimation of the lifetime.

With the in-coincidence method it is possible to reduce the probability of systematic errors, especially in exotic nuclei as the ^{188}Hg where just the lifetimes of few levels have been measured and the presence of unknown feeders is possible. However, the drawback of this method is that the statistics is considerably reduced and so a longer beam time is required.

4.3.2. Differential Decay-Curve Method

The DDCM [41, 48] is a technique for lifetime measurement which presents two great advantages with respect to DCM: first, it depends only on the relative distances between the acquired points, and is not affected by an incorrect estimation of the plunger zero offset; second, the shape of the fitting curve can be chosen arbitrarily, with the condition of being monotone in the region of sensitivity.

The lifetime of the level of interest i can be calculated via [48]

$$\tau_i(x) = -\frac{R_i(x) - \sum_k b_{ki}\alpha_{ki}R_k(x)}{\frac{d}{dx}R_i(x)}\frac{1}{v}\,, \tag{4.9}$$

where b_{ki} and $R_k(x)$ are the branching ratio and the ratio of the feeding transitions, $\frac{d}{dx}R_i(x)$ is the first derivative of the fitting function calculated in x, v is the velocity of the investigated nucleus and the factor

$$\alpha_{ki} = \frac{\omega_k(\Theta)\cdot\varepsilon(E_{\gamma k})}{\omega_i(\Theta)\cdot\varepsilon(E_{\gamma i})} \tag{4.10}$$

depends on the efficiency $\varepsilon(E_\gamma)$ of the detectors and on the angular distribution $\omega(\Theta)$. This method is particularly sensitive in the region where the fitting-function slope is far from being zero and every distance of the plunger leads to a lifetime value, so the final results is the weighted average of the previous values, reducing significantly the statistical error. As in the case of DCM, the DDCM can be also used in $\gamma\gamma$-coincidence measurement. In this case the Eq. (4.9) can be simplified removing the contribution of the feeders $R_k(x)$.

4.4. Lifetime results

In the past, several spectroscopic studies were performed to derive the complex level scheme of the ^{188}Hg [7, 8], but the information on the lifetimes is restricted to just few excited states. Figure 4.8 shows the most complete level scheme [7] with the known states and transitions.

As already mentioned, in this thesis the data coming from two different experiments are presented: during the first experiment, named *week 11*, the measurements were performed at seven different nominal distances (20, 60, 100, 200, 300, 400 and 600 μm); during the second experiment, called *week 30*, the measurements were mainly concentrated at shorter distances (7, 17, 25, 37, 50, 60, 150 μm), in order to be more sensitive in the measurement of shorter lifetimes, and then a final long distance (2000 μm) in order to check the presence of isomers.

4.4.1. Lifetime of the 2_1^+

As introduced in Chapter 1, the lifetime measurement of the 2_1^+ state is fundamental for the study of shape coexistence. For the determination of the lifetime the data sets corresponding to the two different experiments have been taken into account. To avoid contaminations an the inclusion of unwanted feeding, the measurement was performed in coincidence by gating on the in-flight component of the $4_1^+ \to 2_1^+$ transition. Additionally, a background subtraction was performed, in order to limit the contributions of random coincidences that would lead to an overestimation of the components areas. In Figure 4.9 an example of a $\gamma - \gamma$ matrix for the *week 30* experiment with a plunger distance of 150 μm is shown. In order to increase the statistics, on the x axis the Doppler-corrected γ-rays energy is summed up for ring 0, 1 and 2: in this way it is possible to gate on the in-flight component of the transition for the three rings at the same time. In the analysis, the ring 3, placed at 90°, is always excluded because the stopped and the in-flight components are at the same energy and so it cannot be used for the RDDS method. In Figure 4.10 the evolution of the $2_1^+ \to 0_{g.s.}^+$ transition components is shown as a function of different distances.

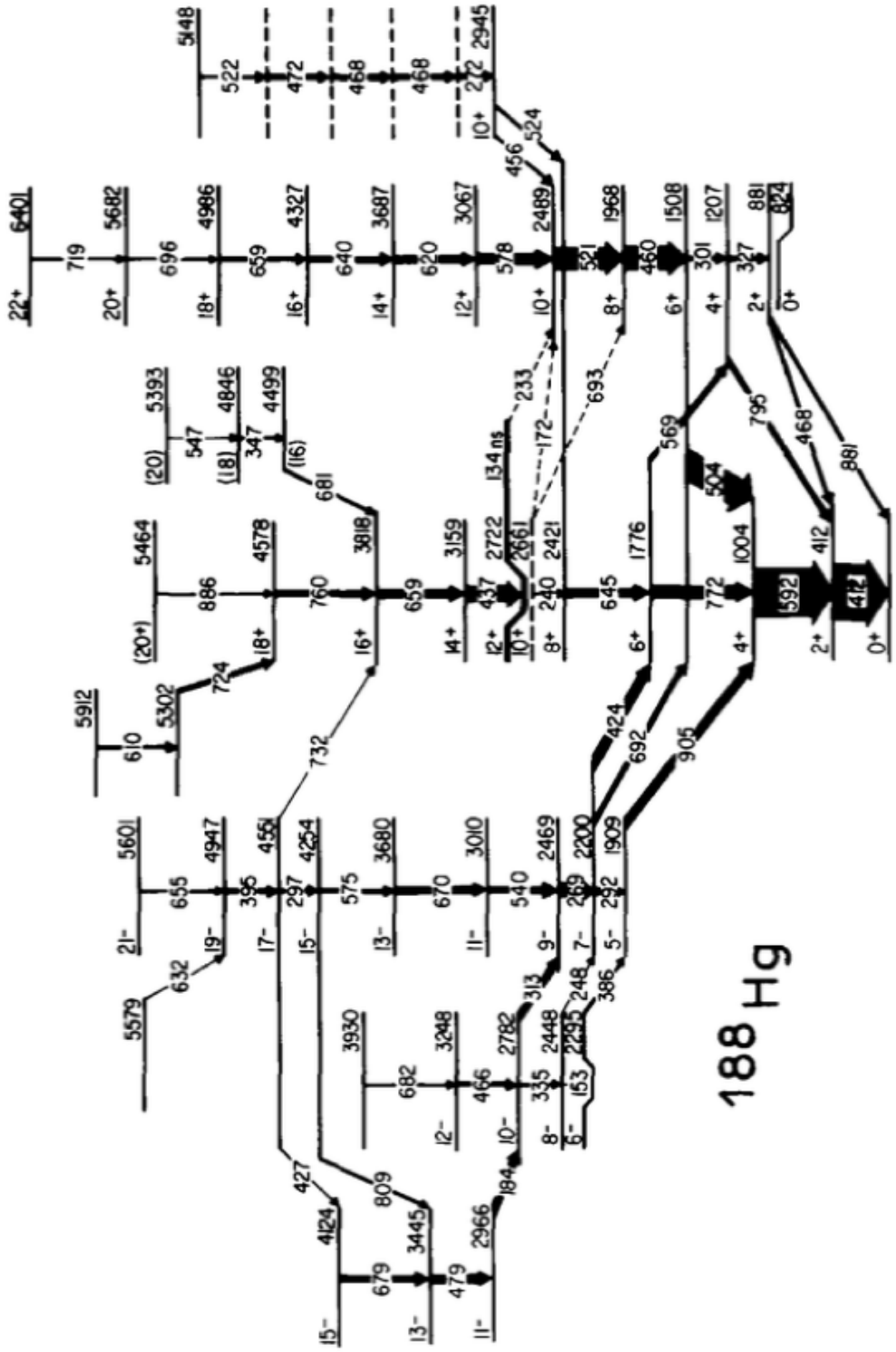

Figure 4.8.: Level scheme of the ^{188}Hg isotope, reported by F. Hannachi in Ref. [7]. The energy of the states and of the transitions are reported in keV.

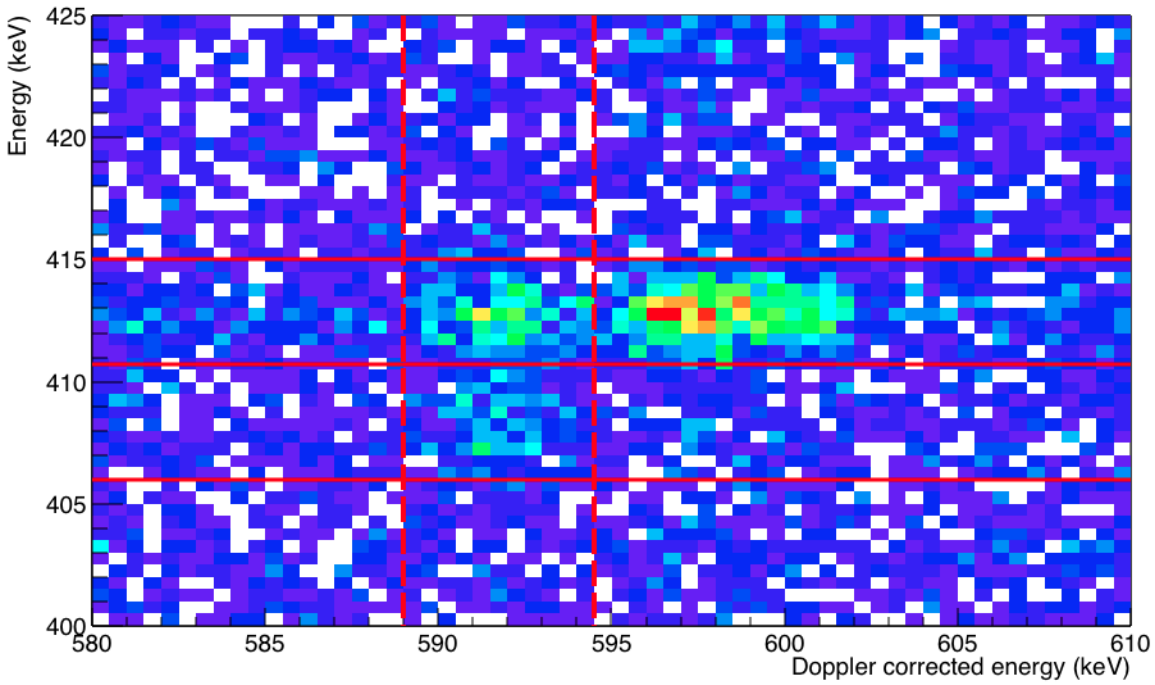

Figure 4.9.: A neutron-gated prompt $\gamma - \gamma$ matrix for the *week 30* experiment at a plunger distance of 150 μm. On the x-axis the Doppler-corrected energy summed up for ring 0, 1 and 2, while on the y axis the energy measured by ring 0 detectors is presented. The gate is performed on the in-flight component of the $4_1^+ \rightarrow 2_1^+$ transition at about 592 keV (dashed lines) to observe the $2_1^+ \rightarrow 0_{g.s.}^+$ transition components (solid lines) at 412.8 keV (stopped) and 409.6 keV (in-flight)

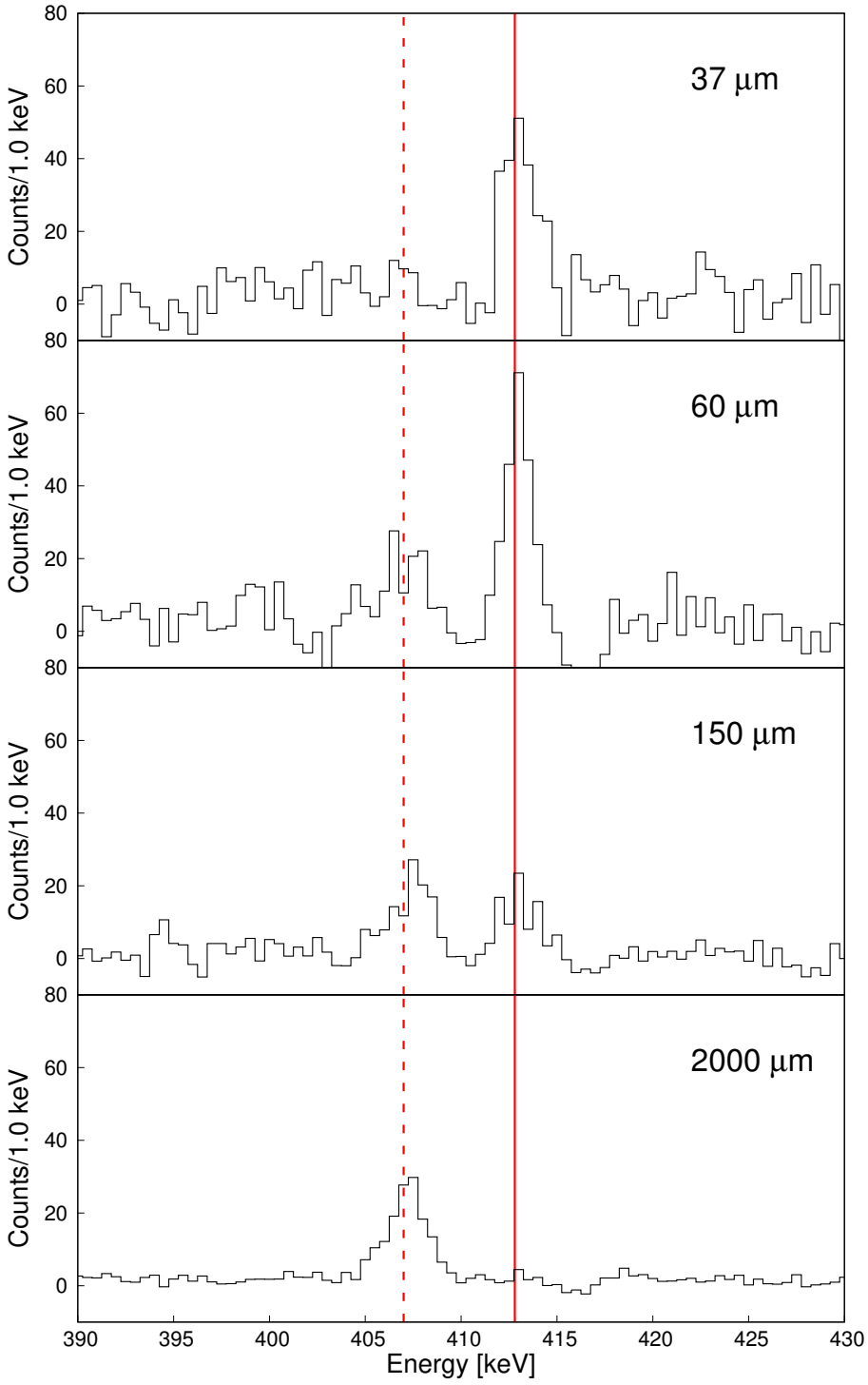

Figure 4.10.: γ-ray spectra, obtained by gating on the in-flight component of the $4_1^+ \rightarrow 2_1^+$ transition, as a function of the plunger distance for the *week 30* experiment. The in-flight (dashed line) and stopped (solid line) components of the $2_1^+ \rightarrow 0_{g.s.}^+$ transition are marked. The spectra are background subtracted.

		DCM [ps]	DDCM [ps]
week 30	Ring 0	35(8)	37(4)
	Ring 1	44(10)	46(5)
	Ring 2	35(6)	38(4)
	Average	37(4)	39.6(25)
week 11	Ring 0	44(2)	35(1)
	Ring 1	34(2)	41(2)
	Ring 2	45(5)	43(2)
	Average	39.4(14)	37.3(8)

Table 4.1.: Results for the $2_1^+ \rightarrow 0_{g.s.}^+$ lifetime measurements with their errors for both *week 30* and *week 11* experiments, using two different methods.

The decay curve, defined in Eq. (4.3), are fitted via

$$R(t) = A\, e^{-t/\tau} + 1 - A \ , \tag{4.11}$$

where A and and τ are free parameters. This parametrization is chosen in order to normalize the function, so the ratio cannot be higher than 1, in agreement with its definition (see Eq. (4.3)). The lifetime is obtained both via DCM and DDCM and the results for the three rings and the two different method are reported in Table 4.1. Such procedure was used both for data of *week 11* and *week 30*, obtaining similar results. The final results, obtained by averaging the values coming from the different rings and the two methods, are 38(2) ps for *week 30* and 37.9(7) ps for *week 11*.

The lifetime of the 2_1^+ state for the ^{188}Hg was already directly measured in a previous experiment performed at the Argonne National Laboratory [49] and it resulted to be 28(13) ps, but this result was never published. Another value of the lifetime was extracted via Coulomb excitation measurement performed at ISOLDE and resulted to be 20(3) ps [12]. Since there is a mismatch between the Coulomb-excitation measurement and the results obtained in this work, the cause of such discrepancy (contaminations, unexpected feeders, etc.) were investigated: all the results coming from the analysis of the experiments *week 11* and *week 30* are in agreement between themselves and support the lifetimes mentioned before. In the next section it will be explained how the evaluation of the lifetime of the 4_1^+ state also supports the lifetime measurement of the 2_1^+ of this thesis.

4.4.2. Lifetime of the 4_1^+

The first attempt to measure the 4_1^+ state lifetime was done by gating on the in-flight component of the $6_1^+ \rightarrow 4_1^+$ transition. However, among all distances of the two experiment, only the 50 μm has useful information for the lifetime measurement: at short distances, in fact, the in-flight component of the $6_1^+ \rightarrow 4_1^+$ transition has low statistics and so an in-coincidence measurement is not possible; at longer distances, instead, the stopped component of the $4_1^+ \rightarrow 2_1^+$ transition was negligible, meaning that the lifetime of the 4_1^+ was shorter than the 6_1^+ lifetime.

Considering such situation, an estimation of the 4_1^+ lifetime was deduced indirectly by gating on the in-flight component of the $6_1^+ \rightarrow 4_1^+$ transition and then measuring the lifetime of the $2_1^+ \rightarrow 0_{g.s.}^+$. Indeed, when measuring the 2_1^+ lifetime it is necessary to take into account

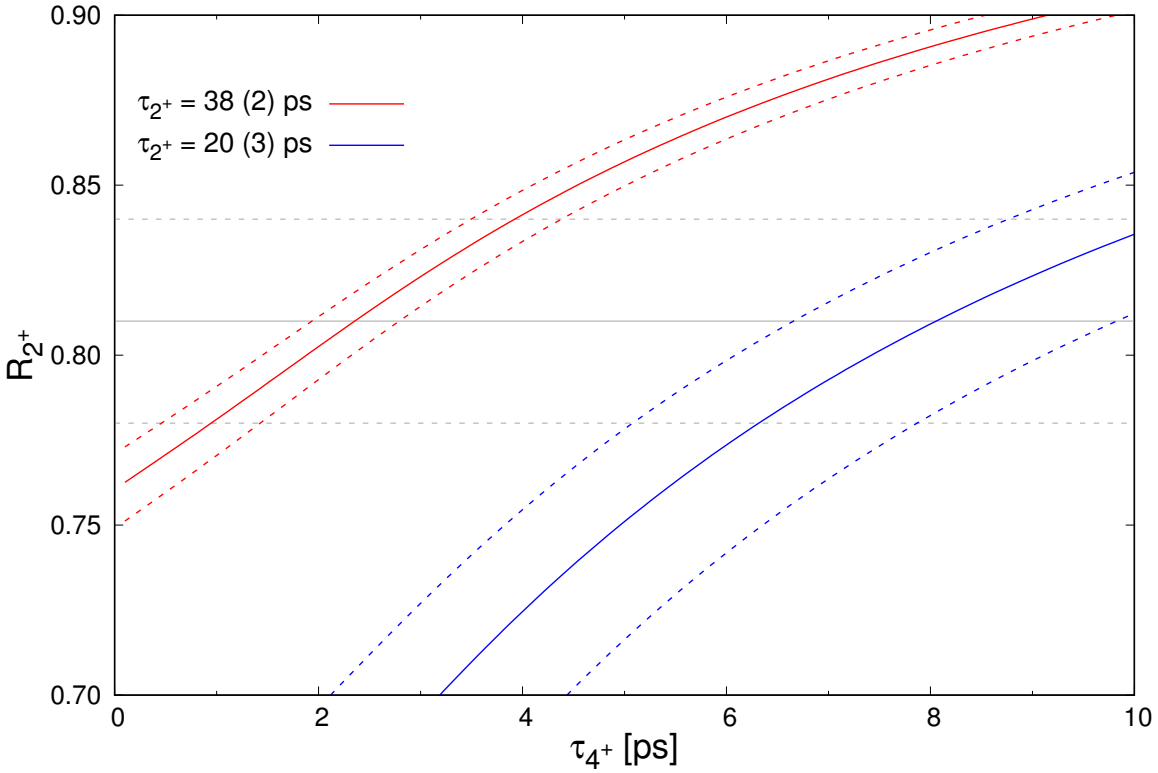

Figure 4.11.: Estimation of the 4_1^+ lifetime. The experimental ratio for the $2_1^+ \rightarrow 0_{g.s.}^+$ transition obtained by gating on the in-flight component of the $6_1^+ \rightarrow 4_1^+$ transition is shown (solid grey line) with its band error (dashed grey lines). The expected ratio of the $2_1^+ \rightarrow 0_{g.s.}^+$ transition estimated as a function of the 4_1^+ state lifetime is presented for $\tau_{2_1^+} = 38(2)$ ps (red) and for $\tau_{2_1^+} = 20(3)$ ps (blue). If the 2_1^+ lifetime is 38(2) ps, the 4_1^+ lifetime is expected to be shorter than 4 ps; while if the 2_1^+ lifetime is 20(3) ps [12], the 4_1^+ lifetime should be longer than 5 ps.

the contribution of the $4_1^+ \rightarrow 2_1^+$ transition. The equation for this specific case is

$$R_2(t) = e^{-\lambda_4 t} + \frac{\lambda_4}{\lambda_4 - \lambda_2}\left[e^{-\lambda_2 t} - e^{-\lambda_4 t}\right] . \tag{4.12}$$

Knowing the lifetime of the 2_1^+ level, measured in the previous section, and its ratio at the distance of 50 μm, the only unknown variable is the 4_1^+ lifetime. In Figure 4.11 the ratio value as a function of the 4_1^+ lifetime is shown: the estimation predicts the lifetime being shorter than 4 ps for the level for a 2_1^+ lifetime of 38(2) ps (red line); if we consider a 2_1^+ lifetime of 20(3) ps (blue line) [12], the 4_1^+ lifetime should be longer than about 5 ps.

A direct measurement has been performed by gating on the in-flight component of the $8_1^+ \rightarrow 6_1^+$ transition and taking into account the contribution of the 6_1^+ (see next paragraph). The equation used to fit the data is similar to Eq. (4.12), corrected for the λ_i of the respective level, and the decay curve is reported in Figure 4.12. The lifetime resulted to be 2.8(7) ps.

In this case, the lifetime measured via RDDS is perfectly in agreement with the result

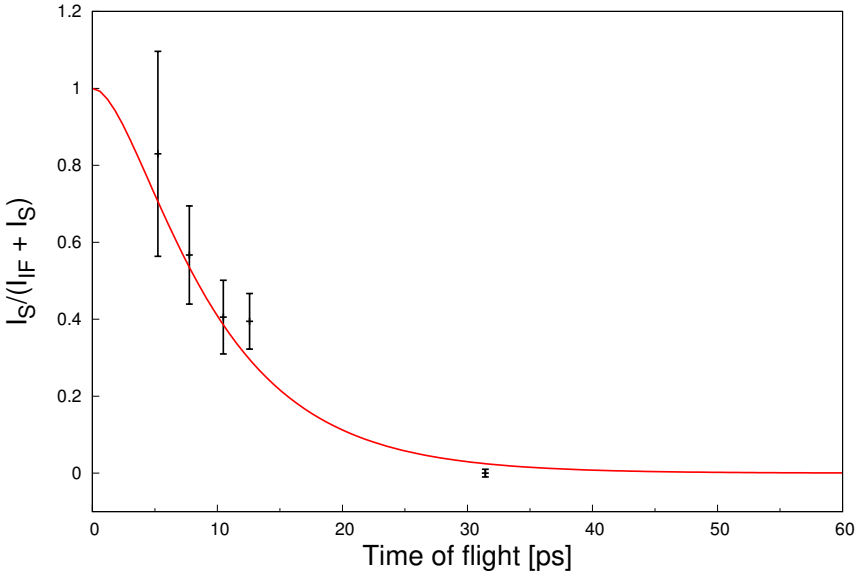

Figure 4.12.: Decay curve for the $4_1^+ \rightarrow 2_1^+$ transition when gating on the in-flight component of the $8_1^+ \rightarrow 6_1^+$ transition for ring 0. The red curve is the fitting function, similar to the Eq. (4.12).

obtained by Bree and collaborators [12] via Coulomb excitation measurement, who measured a lifetime of 2.4(1) ps. This result not only confirms the estimation of the 4_1^+ lifetime being shorter than 4 ps, but also supports the lifetime measurement of the 2_1^+ previously discussed.

4.4.3. Lifetime of the 6_1^+

For the measurement of this level a gate on the in-flight component of the $8_1^+ \rightarrow 6_1^+$ transition has been performed and only the short distances have been used, since the lifetime resulted to be short. Moreover, only the ring 0 and ring 1 have been used: in the ring 2 the two components were not clearly distinguishable, due to the fact that the Doppler shift at 119° is small and, when gating on the feeding transition, the possibility of a contamination from the stopped component leads to a overestimation of the lifetime. The results are reported in Table 4.2, while in Figure 4.13 the two decay curves are shown with the respective DDCM results. The final result for the 6_1^+ lifetime is 7.5(2) ps.

	DCM [ps]	DDCM [ps]
Ring 0	7.0(5)	7.0(6)
Ring 1	7.8(4)	7.9(5)
Average	7.5(3)	7.5(4)

Table 4.2.: Results of the 6_1^+ state lifetime for week 30, ring 0 and 1. The results have been obtained both DCM and DDCM.

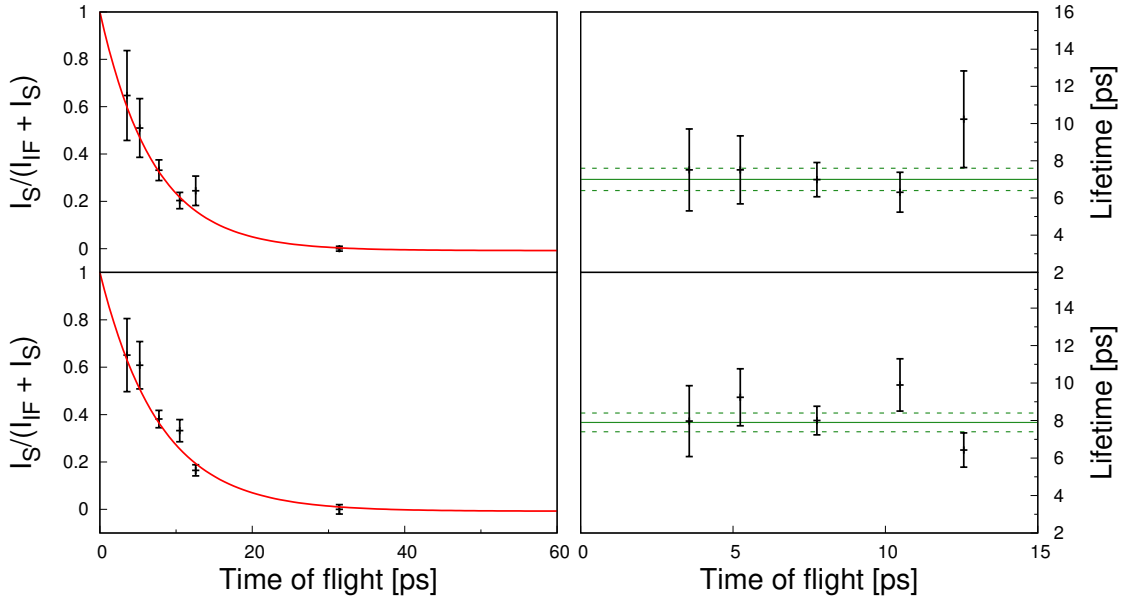

Figure 4.13.: Lifetime measurements of 6_1^+ state of the ^{188}Hg, performed via (left) DCM and (right) DDCM for the *week 30* dataset. The red curve is the fit obtained with Eq. (4.11); the green solid line represent the average value, while the dashed ones are the error bars. The results are (top) $\tau_{DCM}(6_1^+) = 7.0(5)$ ps and $\tau_{DDCM}(6_1^+) = 7.0(6)$ ps for ring 0, while they are (bottom) $\tau_{DCM}(6_1^+) = 7.8(4)$ ps and $\tau_{DDCM}(6_1^+) = 7.9(5)$ ps for ring 1.

4.4.4. Lifetime of the 8_1^+

For the lifetime measurement of the 8_1^+ excited state a gate has been placed on the in-flight component of the $10_1^+ \rightarrow 8_1^+$ transition. It appeared immediately clear that a possible contamination was present, since even at the long distance of 2000 μm (∼400 ps) in the spectrum there was still a consistent stopped component, that would have led to a really long lifetime. The reason behind such unexpected behaviour can be due to contaminations by other transitions: as highlighted in the partial level scheme of Figure 4.14, the energy of the $10_1^+ \rightarrow 8_1^+$ transition cannot be resolved from a transition at 522 keV in a side band between unassigned-spin states (blue). Then, at 152° (ring 0) the Doppler effect shifts the in-flight component of the 468 keV peak (blue) at about 461.5 keV, which is too close to the energy of the stopped component of the $8_1^+ \rightarrow 6_1^+$ transition to be separated, especially taking into account the Doppler broadening of the in-flight component. The same condition affects the γ-ray energy spectrum obtained with the detectors at 129° (ring 1). Finally the contamination disappears for ring 2 at 119° and the stopped component of the $8_1^+ \rightarrow 6_1^+$ transition is absent at long distance. For this reason, the lifetime has been measured using only the ring 2 data. The decay curve and the respective DDCM results are shown in Figure 4.15. The results are $\tau_{DCM}(8_1^+) = 6.6(7)$ ps and $\tau_{DDCM}(8_1^+) = 6.4(7)$ ps and the average value is 6.5(5) ps.

Since the 522 keV transition between unassigned-spin states cannot be distinguished from

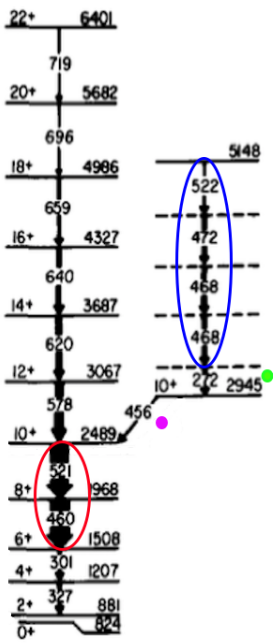

Figure 4.14.: Level scheme of ^{188}Hg showing two side bands. The transitions of interest (see text) are the $8_1^+ \rightarrow 6_1^+$ and the $10_1^+ \rightarrow 8_1^+$ (red circle), while the transitions that contaminate the measurement are those with unasigned spin in the right band at 468 keV (blue circle). Figure adapted from Ref. [7].

	DCM [ps]	DDCM [ps]
Ring 2	6.6(7)	6.4(7)

Table 4.3.: Results for the $8_1^+ \rightarrow 6_1^+$ lifetime for *week 30*, ring 2. The results are compatible.

the $10_1^+ \rightarrow 8_1^+$ transition (521 keV), in principle a contamination of the former transition should be considered when measuring the lifetime of the 8_1^+ state. However, the state that decay to the 10_3^+ with a 272 keV transition (green dot) is expected to have a long lifetime and so its contribution can be assumed to be negligible. Finally, another problem may be due to the $10_3^+ \rightarrow 10_1^+$ transition (purple dot) whose stopped component (456 keV) has the same energy of the in-flight component of the $8_1^+ \rightarrow 6_1^+$ transition; however, since the gate is performed on the in-flight component of the 8_1^+ feeder, the presence of such a stopped component is avoided. This is a good example of the capabilities of the $\gamma\gamma$ coincidence method.

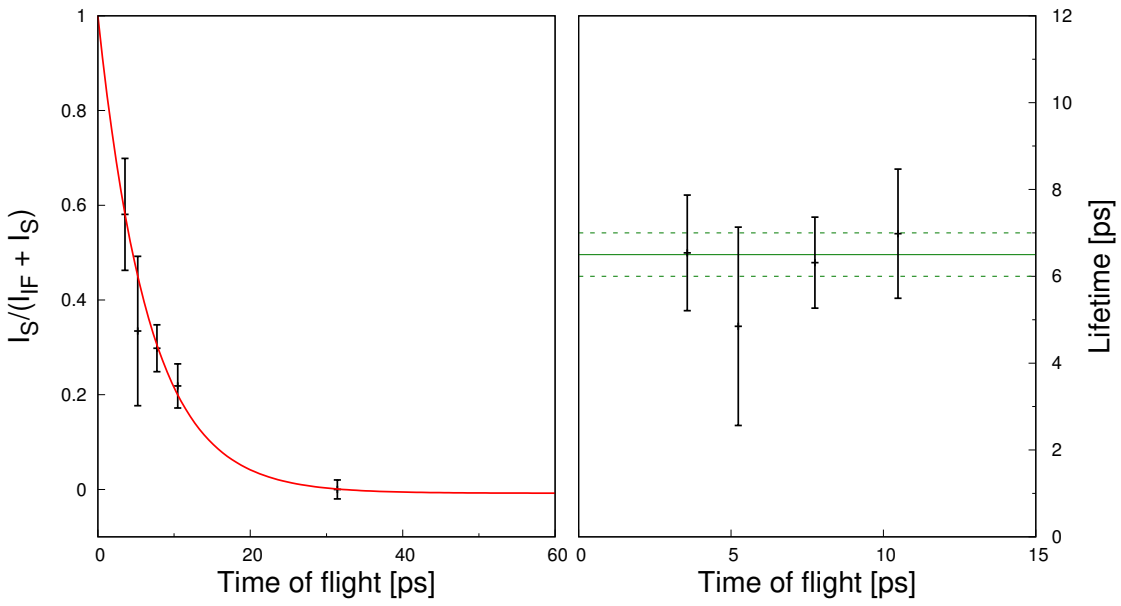

Figure 4.15.: Decay curve and lifetime measurement for the $8_1^+ \rightarrow 6_1^+$ transition for ring 2. The results are reported in Table 4.3

5 Theoretical Interpretation

In Chapter 4, the experimental method has been described and the lifetime of the first 2^+, 4^+, 6^+ and 8^+ states has been determined from the experimental data. However, to better understand on the nuclear structure of the ^{188}Hg and in particular on the possible presence of shape coexistence in this nucleus, a theoretical interpretation is needed. For this reason the state-of-the-art beyond-mean-field calculations have been performed using the symmetry-conserving configuration-mixing method in collaboration with Dr. Tomás Raúl Rodríguez Frutos from the Departimento de Física Teórica, Universidad Autónoma de Madrid (Spain). This theoretical approach has already been used successfully in the study of nuclear structure of both neutron-rich and -deficient species [50–52] and also in the investigation of shape coexistence [53].

In this chapter the reduced transition probability $B(E2; I \rightarrow I-2)$ will be presented and compared to the results of previous experiments in the neutron-deficient mercury isotopic chain. A rapid introduction to the basic ingredients of the theoretical model will be given before comparing our experimental results to this new theoretical approach. Then for ^{188}Hg the new predictions will be presented and compared to previous calculations [11, 12], which were already introduced in Chapter 1. Finally, the experimental results for the $B(E2)$ values will be compared with the theoretical results.

5.1. B(E2) systematics along the Hg isotopic chain

As already introduced in Chapter 1, the reduced transition probability $B(E2; 2_1^+ \rightarrow 0_{g.s.}^+)$ of ^{188}Hg represents an important fingerprint for the determinations of the presence of shape coexistence. The neutron-deficient Hg isotopes have been investigated in several experiments, via both lifetime [10, 14–17, 19] and Coulomb excitation (CE) [12] measurements, that allowed the extraction of the $B(E2)$ values of the low-lying transitions.

The present experiment represents the first estimation of the $B(E2; 2_1^+ \rightarrow 0_{g.s.}^+)$ and $B(E2; 4_1^+ \rightarrow 2_1^+)$ values via direct lifetime measurement and also the first measurement of the $B(E2; 6_1^+ \rightarrow 4_1^+)$ and $B(E2; 8_1^+ \rightarrow 6_1^+)$ values for the ^{188}Hg. The results of this experiment are presented in Figure 5.1 and compared to previous experimental results in the region.

From Figure 5.1, it is clear the mismatch between the lifetime measurement of this thesis and the Coulomb excitation of N. Bree et al. [12] regarding the 2_1^+ excited state. On the

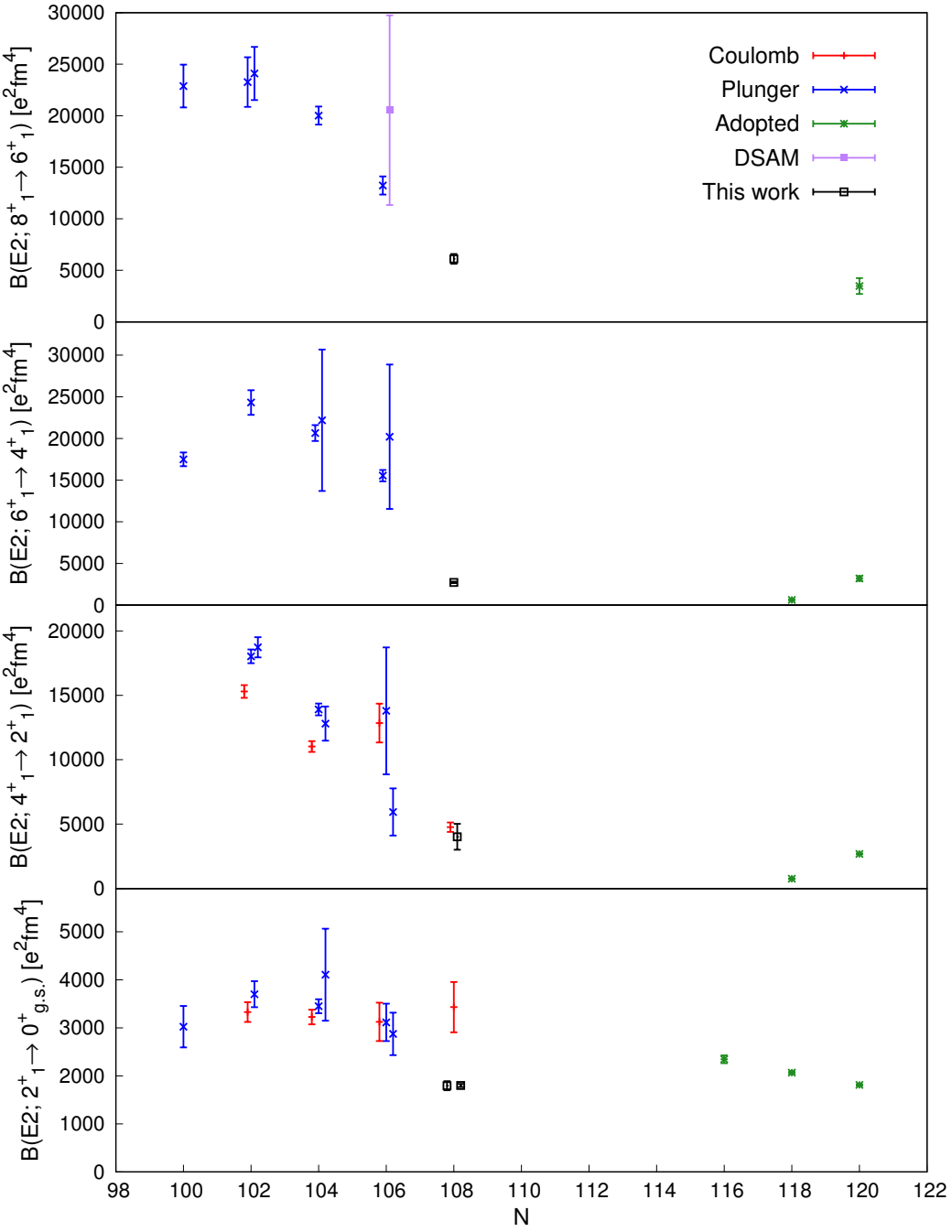

Figure 5.1.: Systematics of the esperimental reduced transition probabilities $B(E2)$ values of the low-lying transitions for the neutron-deficient mercury isotopic chain. From the bottom, the $B(E2)$ values are reported for the $2_1^+ \rightarrow 0_{g.s.}^+$, $4_1^+ \rightarrow 2_1^+$, $6_1^+ \rightarrow 4_1^+$ and $8_1^+ \rightarrow 6_1^+$ transitions: the results in blue and purple were obtained via RDDS [10, 14–17] and DSAM [19], respectively; in red the values measured by N. Bree et al. via Coulomb excitation [12]; in green the "adopted" results for the nuclei close to stability are taken from Ref. [20]. The results of this work are also presented (black).

	$B(E2; I \to I-2)$ $[e^2\mathrm{fm}^4]$			
	$2_1^+ \to 0_{g.s.}^+$	$4_1^+ \to 2_1^+$	$6_1^+ \to 4_1^+$	$8_1^+ \to 6_1^+$
ISOLDE	3432(210)	4761(368)	–	–
This work	1795(94) 1800(33)	4016(1004)	3352(89)	6108(470)

Table 5.1.: Experimental reduced transition probabilities $B(E2)$ values for the low-lying transitions of ^{188}Hg: the results obtained in this work (*week 30* top, *week 11* bottom) are compared with the previous Coulomb-excitation measurement performed at ISOLDE [12].

other hand, as discussed in Chapter 4, not only the results obtained from the two experiments of this thesis (*week 11* and *week 30*) are consistent with themselves and the presence of contaminations was excluded after a thorough analysis, but also the procedure to extract the lifetime of the 4_1^+ state supports the mentioned lifetime (see Figure 4.11). Moreover the $B(E2; 4_1^+ \to 2_1^+)$ value is compatible with the previous Coulomb-excitation measurement, supporting the validity of the described method. Finally, the reduced transition probability $B(E2; 6_1^+ \to 4_1^+)$ and $B(E2; 8_1^+ \to 6_1^+)$ have been measured for the very first time in this work: these two new outcomes seem to follow the parabolic trend of the previous measurements in lighter nuclei. However, for a better comprehension of the nuclear structure of ^{188}Hg the comparison with theoretical models is mandatory. The experimental $B(E2)$ values obtained in this work are summarized in Table 5.1 together with the results from the Coulomb-excitation measurement.

5.2. Symmetry-conserving configuration-mixing methods

Self-consistent mean-field studies have been largely used in the investigation on shape mixing by analysing potential-energy surfaces using high quality phenomenological effective interactions, as for example Gogny, Skyrme or relativistic [51]. On one hand, this approach has a strong predictive power on bulk properties, such as the nuclear mass or the radius. However, since the pure mean field approach is defined in an intrinsic frame, it does not give information on spectroscopic properties, such as excitation energies or transition probabilities in the laboratory frame. To describe those properties, the inclusion of Beyond Mean Field (BMF) correlations is necessary in order to restore the symmetries and take into account the mean-field many-body states configuration mixing.

In this work, the neutron-deficient ^{188}Hg has been studied using the Symmetry-Conserving Configuration-Mixing (SCCM) method with the Gogny D1S nuclear interaction [51, 53]. The first step in this method is the calculation of a set of intrinsic wave functions with different deformations in the triaxial (β_2, γ) plane. The intrinsic wave functions are the solutions of the particle-number projected Hartree-Fock-Bogoliubov equations with constraints in the quadrupole deformations. This is the so-called particle-number variation after projection (PN-VAP) method [54] and it provides a first interpretation of the structure of the nucleus in terms of shapes by analyzing the PN-VAP energy as a function of (β_2, γ). In Figure 5.2 (left), the total excitation energy is presented as a function of the deformation parameters (β_2, γ), where β_2 quantify the deformation of the nucleus while γ measures the degree of triaxiality (i.e. 0° corresponds to an axial prolate direction, 60° to an axial oblate direction and the

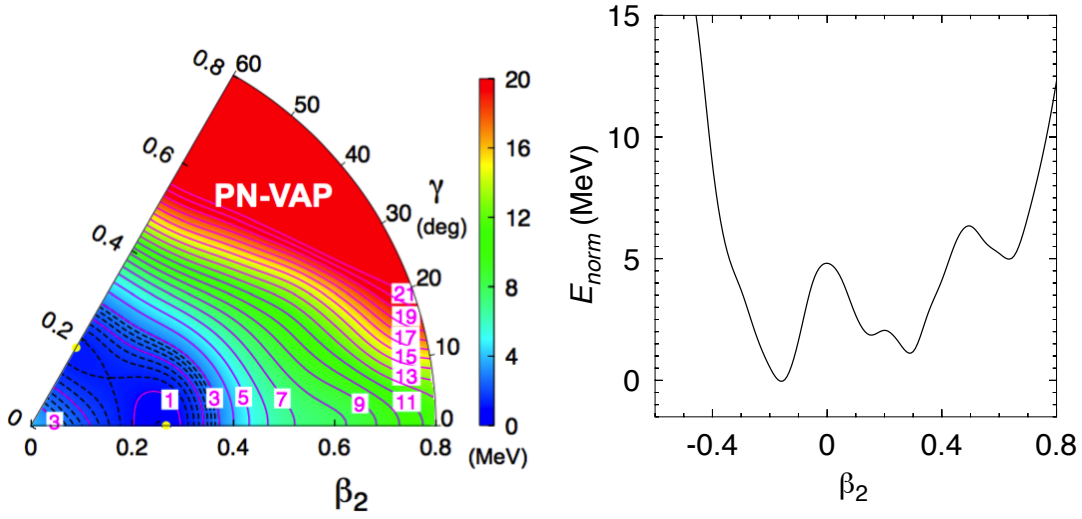

Figure 5.2.: (Left) The total energy as a function of the deformations for the ^{188}Hg. In the present case the nucleus shows an absolute minimum at $\beta_2 \sim 0.20$ and $\gamma = 60°$, corresponding to an axial oblate deformation. (Right) The total energy plotted on the axial direction, where negative (positive) values of β_2 correspond to oblate (prolate) deformations.

values in between it indicates triaxiality), while on the right, the total energy plotted on the axial direction is presented (negative values of β_2 correspond to an oblate deformation, positive values to a prolate deformation), in order to ease the identification of the absolute minimum. In the present case, the absolute minimum of the potential energy surface (PES) is at $\beta_2 \sim 0.20$ and $\gamma = 60°$, that represents an oblate state. However, we observe a rather flat PES connecting the absolute oblate minimum with a secondary prolate minimum ($\beta_2 \sim 0.25$) at an excitation energy of 1.18 MeV along the γ degree of freedom. This softness and the presence of two minima could indicate a probable shape coexistence and/or mixing in this nucleus, as shown in Figure 5.2 [55].

The next step of this method is the symmetry restoration: in fact, mean-field states break both the particles number and the angular momentum symmetries of the Hamiltonian, meaning that those states are not eigenstates of the particles number and the angular momentum operators. This symmetry-breaking leads to an apparent "paradox" since the number of nucleons is well known in the ^{188}Hg, as well as the angular momentum J of the excited states. Pure mean-field calculations cannot predict such quantum numbers and it is necessary to project onto their eigenstates. The angular momentum restoration (commonly called PNAMP) has the effect of lowering the prolate band, that becomes the ground state of the nucleus as shown in Figure 5.3. The first level of the oblate state can be found at an excitation energy of 1.14 MeV [55].

In addition to the symmetry restoration, shape mixing is also performed within the generator coordinate method [56]. The final results after these projections and mixing indicate the presence of five bands, presented in Figure 5.4. For each of these bands the collective-wave functions (CWF) are plotted under the level scheme. The CWF represent the weights of each intrinsic deformation, i.e. the probability of finding each state (J_i^P) in a given deformation.

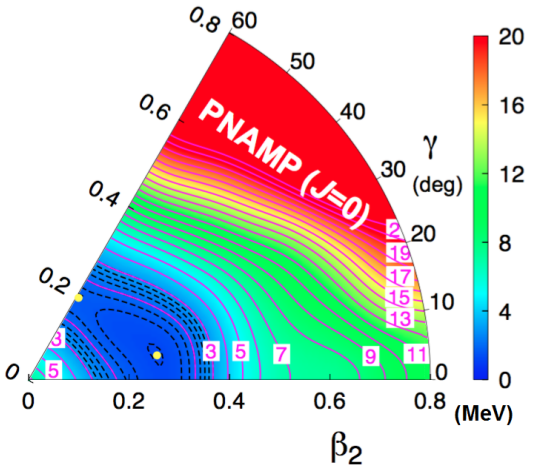

Figure 5.3.: Total energy as a function of the deformation after the angular momentum restoration for the ^{188}Hg. In the present case, the nucleus corresponds to a triaxial minimum ($\gamma = 10°$) at $\beta_2 \sim 0.25$.

Indeed, after restoring the symmetries and the mixing between different mean-field many-body states, it emerges that the ground state 0_1^+ is slightly triaxial ($\gamma \sim 10°$) and prolate deformed ($\beta_2 \sim 0.3$), so presenting a bit of mixing in the γ direction towards more oblate configurations; the excited state 0_2^+ is mostly oblate ($\gamma = 60°$, $\beta_2 \sim 0.15$) with a bit of mixing towards less oblate configurations; then a third 0_3^+ excited state presents a more triaxial and less mixed deformation ($\gamma \sim 20°$, $\beta_2 \sim 0.25$). The model also predicts the presence of two bands with $\Delta J = 1$: one is built on the top of a 2_3^+ state ($\gamma \sim 10°$, $\beta_2 \sim 0.25$) and one on a 4_4^+ state ($\gamma \sim 10°$, $\beta_2 \sim 0.30$).

The most significant result of these calculations is the appearance of two collective bands (the 0_1^+ triaxial-prolate deformed and the 0_2^+ oblate) that are rather close in energy ($\Delta E \sim 0.2$ MeV) which corresponds to the potential well found in Figure 5.2. This is a distinctive signature of shape coexistence [55].

The difference between the SCCM approach and the other methods (see Chapter 1) can be attributed to three main reasons [55]:

- The chosen interactions are not the same. In fact, T. Nikšić and collaborators [11] uses the RHB method with a Skyrme interaction, adapted for the shape coexistence; in their work the bulk properties (e.g. binding energies, charge radii, etc.) are well described in this mass region, however no spectroscopic properties could be reproduced. In the work of Bree and collaborators [12], instead, the experimental results are compared to both IBM and BMF-Skyrme calculations.

- A different method was also used in order to compute the set of intrinsic wave functions. While in the present study the PN-VAP is used, other works commonly use the Lipkin-Nogami (LN) [57, 58], which is an approximation of the previous one.

- The SCCM calculations includes the triaxial degree of freedom, while in the previous papers the restriction to axial deformations limits the possibility of mixing through the γ direction. This latter difference is crucial to explain the disagreement.

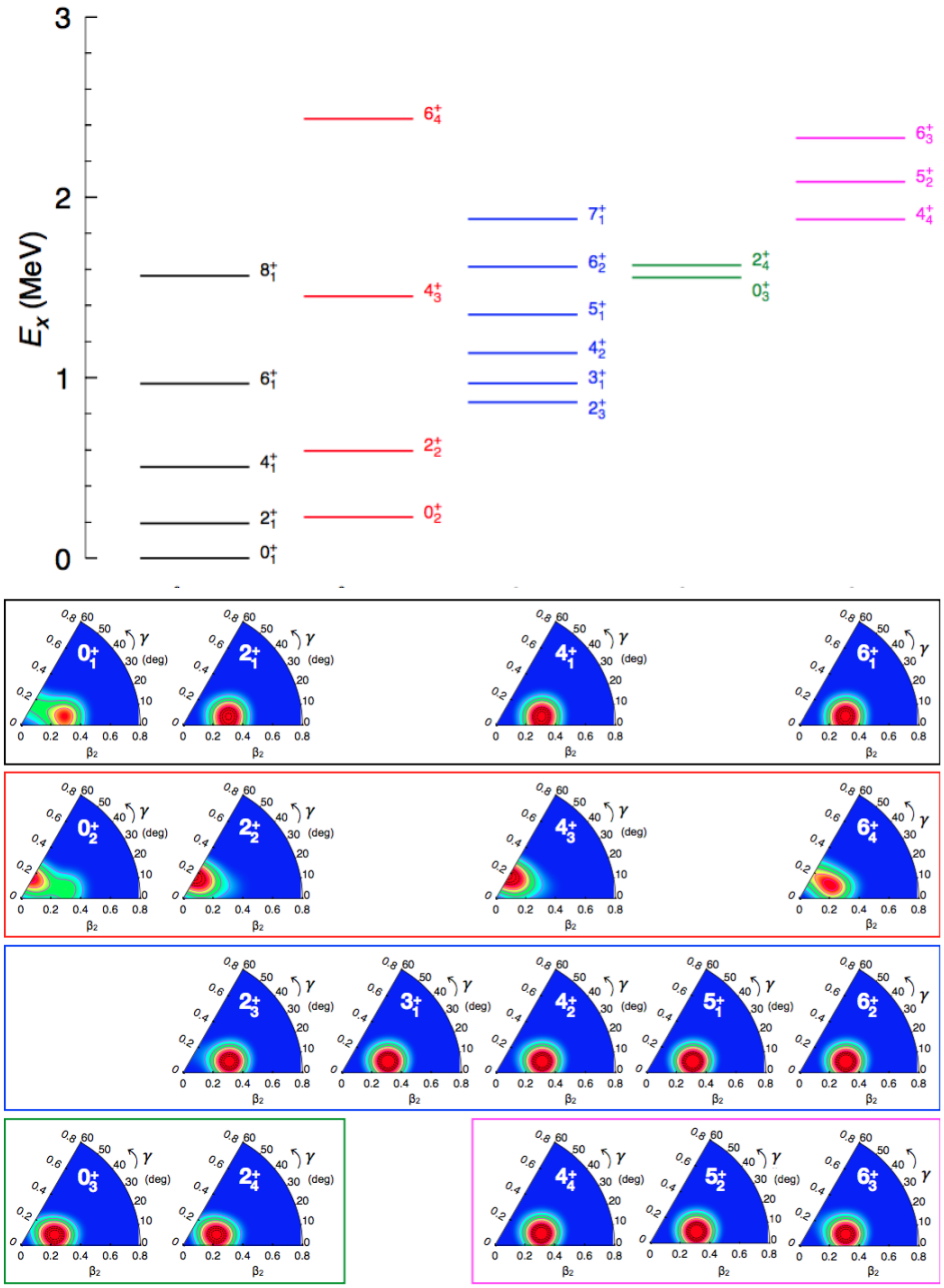

Figure 5.4.: (Top) Excitation energy of the computed levels of the ^{188}Hg. From the SCCM calculations, five bands are predicted: three with $\Delta J = 2$, built on the top of a 0^+ level and two $\Delta J = 1$ built on the top of a 2^+ and a 4^+ state. The ground-state band appears to be triaxial prolate deformed, crossed by an intruder band within an energy range of ~ 0.2 MeV that results being oblate deformed [55]. (Bottom) Deformation of each computed state as a function of the (β_2, γ) coordinates. It is possible to notice that states belonging to the same band have a similar deformation.

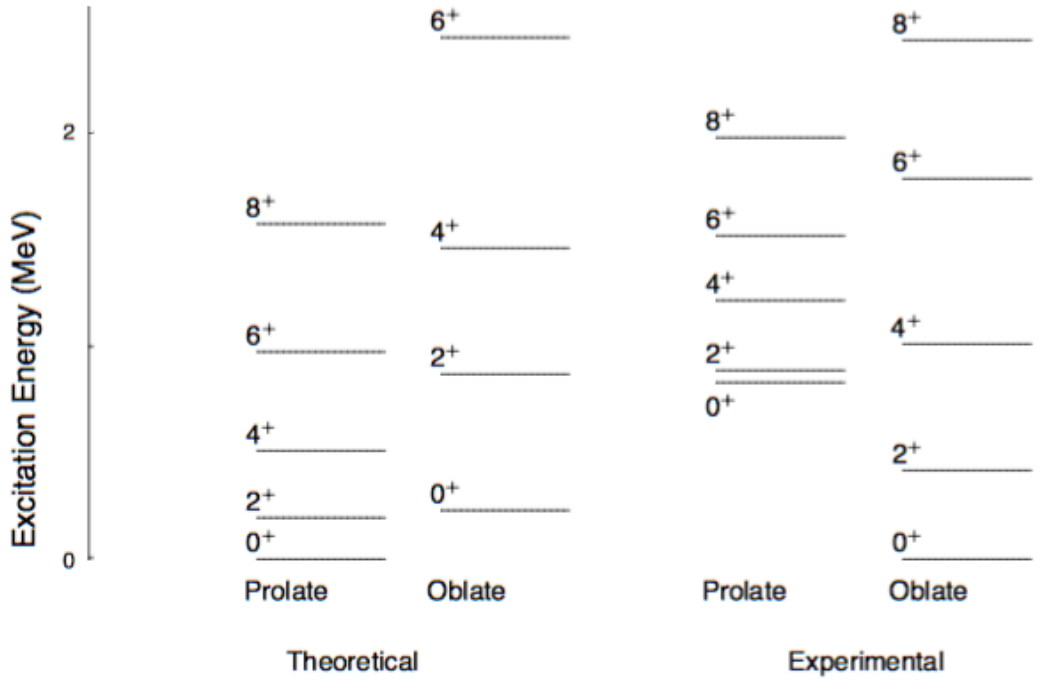

Figure 5.5.: Energy level obtained from the SCCM calculations and from experimental measurements. The theory foresees the ground-state band to be prolate deformed and the first excited 0^+ state to be at an excitation energy of about 0.2 MeV and oblate deformed; spectroscopy measurements predicts the ground-state band to be oblate deformed and the first excited band to be at an excitation energy of 0.824 MeV. This exchange of the bands can be due to an overestimation of the deformation of the triaxial-prolate band [55].

5.3. Comparison with the experimental results

In order to better understand the structure of the ^{188}Hg, the experimental results are compared with the theoretical calculations. First, let us compare the level scheme predicted by the SCCM calculations after the restoration of the symmetries with the experimental values (see Figure 5.5). The theory foresees the ground state to be prolate deformed and the first excited 0^+ state to be at about 0.2 MeV and to be oblate deformed, while from experimental measurements the ground state band results to be oblate deformed and the first excited 0^+ to be prolate deformed at an excited energy of 0.824 MeV. Moreover, the third 0^+ band and the two $\Delta J = 1$ bands are not observed.

A possible interpretation about why the observed bands are exchanged is the overestimation of the deformation in the triaxial-prolate band. This overestimation entails a lowering of the prolate band that becomes the ground state of the nucleus [55]. A small change in the prediction of this band towards smaller value would keep the oblate band as the ground state after the mixing, in agreement with previous theoretical calculations [11] and experimental measurements.

	Theory		This work	
	Prolate	Oblate	*week 30*	*week 11*
$B(E2; 2^+ \to 0^+)$	11411	3325	1795(94)	1800(33)
$B(E2; 4^+ \to 2^+)$	22382	5793	4016(1004)	
$B(E2; 6^+ \to 4^+)$	26109	7403	3352(89)	
$B(E2; 8^+ \to 6^+)$	28774	12615	6108(470)	

Table 5.2.: Reduced transition probabilities obtained from theoretical calculations for the ground-state (prolate) band and the first excited (oblate) band [55]. The experimental values obtained in this work are also reported, in order to ease the comparison. The $B(E2)$ values are reported in $e^2\text{fm}^4$.

This exchange between the bands is also suggested by the comparison with the reduced transition probabilities $B(E2; I \to I-2)$ (Table 5.2). Indeed, the $B(E2)$ value for the theoretical $2_2^+ \to 0_2^+$ transition is in agreement with the CE measurement for the $2_1^+ \to 0_{g.s.}^+$ transition, while the result obtained in this thesis results to be an underestimation of the reduced transition probability.

In the same way, the theoretical $B(E2; 4_2^+ \to 2_2^+)$ value is in agreement with the experimental values for the $B(E2; 4_1^+ \to 2_1^+)$. The slightly overestimation of the theoretical value is acceptable considering the mismatch between the theoretical and experimental excitation energies.

The reduced transition probability for the $6_1^+ \to 4_1^+$ transition was not comparable with the theoretical calculations. In fact, this transition link the two bands, in particular from the first excited (prolate) and the ground-state band (oblate); because of the lowering of the prolate band in the theoretical calculations, the 4^+ of the oblate band results at higher energy with respect to the 6^+ of the prolate band, and so the transition results suppressed.

Finally, the theoretical $B(E2; 8_1^+ \to 6_1^+)$ value resulted way larger than the experimental value. Again, this disagreement is mainly due to the overestimation of the γ transition in the theoretical calculations: this correction would reduce the theoretical $B(E2; 8_1^+ \to 6_1^+)$ of about a factor 3.5.

6 Conclusions

Up to now, the problem of shape coexistence in the neutron-deficient mercury isotopic chain is still open. The Hg nuclei from $N = 100$ to $N = 106$ have been widely studied both via lifetime measurement and from the extraction of E2 matrix elements. The experimental results confirmed the presence of such phenomenon. On the contrary, there is no information about the isotopes with $110 \geq N \geq 114$ because the presence of isomers limits the investigation of the low-lying states of these nuclei populated via fusion-evaporation reactions. The appearance of shape coexistence in ^{188}Hg is strongly suggested both by the observation of an intruder band close in energy to the ground-state band and by different theoretical calculations.

The aim of this thesis was to study the shape coexistence in the nucleus of interest via lifetime measurement with the Recoil Distance Doppler-Shift method. From experimental measurement with the plunger, the lifetime of the 2_1^+ level resulted to be 38(2) ps (*week 30*) and 37.9(7) ps (*week 11*). The lifetime of the 4_1^+ state was also directly measured for the first time, and the result $\tau = 2.8(7)$ ps was in agreement with the Coulomb excitation measurement. Finally, the lifetimes of the 6_1^+ and 8_1^+ were measured for the very first time and resulted to be 7.5(2) ps and 6.5(5) ps, respectively. From these results, it was possible to extract the reduced transition probabilities of the transitions, in order to compare them with the theoretical calculations.

The ^{188}Hg was studied using the Symmetry-Conserving Configuration-Mixing (SCCM) method that predicts the ground-state band to be prolate deformed and the first excited band to be oblate deformed with an excitation energy of about 0.2 MeV. These calculations foresee the presence of shape coexistence in the nucleus.

From the comparison with the experimental data, the presence of the two bands is confirmed but an exchange between these two is also observed, where the prolate band results to be the first excited band and the oblate band results to be the ground-state band, in agreement with previous theoretical calculations. Moreover, the reduced transition probabilities for the $2_1^+ \rightarrow 0_{g.s.}^+$ transition seemed to be in agreement with the Coulomb-excitation measurement, that foresees a shorter lifetime and hence a larger transition probability. A possible explanation of this mismatch between the measurement of this thesis and the previous measurement could be the presence of an unknown contamination, either due to a different channel populated in the fusion-evaporation reaction or to an unobserved transition at the same energy of the in-flight component of the $4_1^+ \rightarrow 2_1^+$, where the gate is performed.

It is possible to conclude that the presence of shape coexistence in the ^{188}Hg isotope has been confirmed. However, the origin of this phenomenon is not yet clearly identified and so a deeper investigation of the theoretical wave functions as well as the determination of the higher lying states lifetimes are needed. Moreover, since the ^{190}Hg is expected to be the lightest isotope where shape coexistence should not be observed, additional information on the collectivity evolution can be obtained by enlarging the investigation to such a nucleus. Thus, future studies on the "border-line" species may shed light on the mechanism behind the shape coexistence in Hg neutron-deficient nuclei.

A

Nuclear models

The nucleus is a many-body quantum system and its behaviour is determined by the rules of quantum mechanics. The most natural choice for the degrees of freedom is to use the nucleonic ones: the A sets position $\vec{r}_i$, spin $\vec{s}_i$ and isospin $\vec{\tau}_i$. The wave function can be generalized as [59]

$$\psi(\vec{r}_1, \vec{s}_1, \vec{\tau}_1, \ldots, \vec{r}_A, \vec{s}_A, \vec{\tau}_A)\,, \tag{A.1}$$

while the Hamiltonian is usually written as the sum of two components

$$\hat{H} = \sum_{i=1}^{A} \frac{\hbar^2}{2m}\nabla^2 + \frac{1}{2}\sum_{ij} V(\vec{r}_i, \vec{r}_j) \tag{A.2}$$

where the first term describes the kinetic energy of the nucleons and the second is related to the nucleon-nucleon interaction. It is clear that the solution of the Schrödinger equation for this system is feasible only for light nuclei while for heavier systems the numerical calculation power of current computers is not sufficient. For this reason, many models have been developed during the years in order to describe the nuclear interaction and also to predict experimental observables (e.g. mass, the radius, the energy of the excited states, etc.). In this appendix two models will be discussed: the nuclear shell model and the collective model.

A.1. The shell model

From experimental observations of the binding energy of the nuclei as a function of proton and neutron number, it appears clear that some nuclei are more stable than others, corresponding to certain "magic" numbers of protons (Z) and neutrons (N). This is a direct consequence of the fact that the nucleus is a system of fermions (the nucleons) in a potential following the Pauli exclusion principle. This idea is also supported by the analogy with the atomic model, where the ionization energy of the electrons shows a significant increase at Z = 2, 10, 18, 36, 54, 86, corresponding to the noble gases. However, there is a fundamental difference between the atomic and the nuclear shell model: in the former the potential is supplied by an external agent (i.e. the Coulomb field of the nucleus) while in the latter the nucleons move in a potential that is created by the nucleons themselves.

At first two different potentials were proposed as candidates for the nuclear potential: the

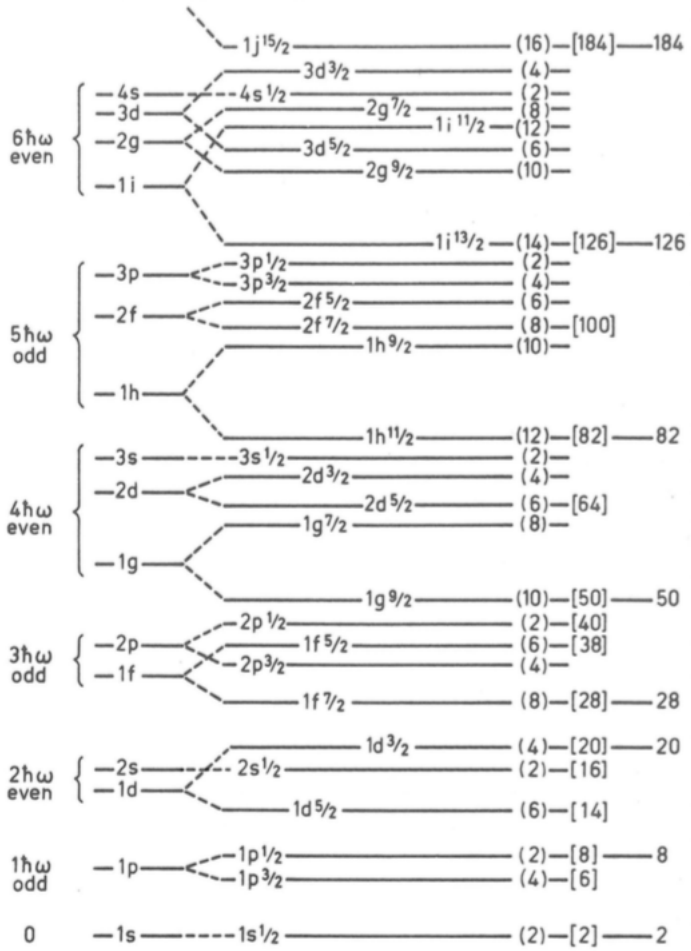

Figure A.1.: Single particle levels. The spin-orbit term has the effect of lowering the $j = l \pm \frac{1}{2}$ orbital of a given shell. In this way, along with 2, 8 and 20, new magic numbers appear: 28, 50, 82, 126 and 184. Figure adapted from Bohr and Mottelson [60].

infinite well and the harmonic oscillator. As in the atomic case, the degeneracy $2(2L+1)$ of each level corresponds to the number of nucleons that can fit in a level according to the Pauli exclusion principle. These two potentials could well describe the light nuclei up to Z=20 but failed in the prediction of the higher magic numbers. A more realistic potential was then suggested to better describe the properties of the nucleus [29]

$$V(r) = \frac{-V_0}{1 + exp[(r-R)/a]} \tag{A.3}$$

where $R = 1.25A^{1/3}$ fm is the nuclear radius, a fm is the skin thickness, while the well depth V_0 MeV is adjusted in order to reproduce the proper nucleons separation energies. This potential, known as Wood-Saxon potential, predicts the magic numbers 2, 8, 20, 40, 58, 92, 112, that is still far from the experimental results.

It was clear that something fundamental was still missing. The solution came from the works of Mayer [61, 62] and Haxel, Jensen and Suess [63] independently, who suggested the addition of a spin-orbit term to the potential. Once again, the idea was suggested by the spin-orbit interaction observed in atomic physics and by scattering experiments that confirmed the presence of a nucleon-nucleon spin-orbit force. The spin-orbit term is written as

$$V_{so}(r)\hat{l} \cdot \hat{s} \tag{A.4}$$

where the $\hat{l} \cdot \hat{s}$ causes the reordering of the levels. It is convenient to label the state with the angular momentum $\hat{j} = \hat{l} + \hat{s}$ and to re-write the spin-orbit term as

$$\hat{l} \cdot \hat{s} = \frac{1}{2}(\hat{j}^2 - \hat{l}^2 - \hat{s}^2) \tag{A.5}$$

so that $\hat{j}^2$, $\hat{l}^2$ and $\hat{s}^2$ can form a set of commuting angular operators that admit a set of common eigenvalues and eigenstates. The spin-orbit term has the effect of lowering the $j = l \pm \frac{1}{2}$ orbitals of a given large oscillator shell, leading to new shell-closure numbers at 28, 50, 82 and 126. The single-particle spectrum is show in Figure A.1.

The nuclear shell model has an incredible predictive power and provides a well-defined procedure for the calculation of nuclear observables (i.e. energy level) for light nuclei and for nuclei near the shell closure. However, when the number of valence nucleons outside the closed shell becomes larger, the number of possible single-particle configurations increases severely and shell-model calculations are not feasible with nowadays computing capabilities. In order to describe the features of medium mass nuclei, two possible paths have been considered, both based on the nuclear deformations. On one hand, one can consider the single-particle motion of nucleons in a deformed-nucleus field (deformed shell model, also known as Nilsson model); on the other hand, one can focus on the macroscopic motion and excitation of a deformed nucleus. This latter approach, also known as collective model, will be discussed in the following section.

A.2. Collective model

The idea of describing the nucleus as a liquid droplet and to link the collective modes of motion to nuclear excited states, first came from A. Bohr in 1952 [64] and it is considered the foundation of the collective model, that was further developed with B.R. Mottelson [60].

The basic idea behind this model is to consider various properties of a nucleus described in terms of a deformable surface coupled to the motion of individual nucleons. The radius of the nucleus can be parametrized using spherical harmonics [64]:

$$R(\theta,\phi) = R_0 \left(1 + \sum_{\lambda,\mu} \alpha_{\lambda,\mu} Y_{\lambda,\mu}(\theta,\phi)\right) , \tag{A.6}$$

where R_0 is the radius of the nucleus in a spherical configuration and $\alpha_{\lambda,\mu}$ are the coordinates that define a multidimensional space. If $\alpha_{\lambda,\mu}$ is sufficiently small, the Bohr Hamiltonian built with the generalized coordinates and momenta in a quadrupole deformation space can be written as [64]

$$H_B = T + V = \sum_{\lambda,\mu} \left(\frac{1}{2B_\lambda}|\pi_{\lambda,\mu}|^2 + \frac{C_\lambda}{2}|\alpha_{\lambda,\mu}|^2\right) , \tag{A.7}$$

where B_λ and C_λ are the mass and the stiffness parameters, respectively, while $\pi_{\lambda,\mu}$ are the conjugated momenta associated to the variables $\alpha_{\lambda,\mu}$.

This model represents a complementary approach to the shell model, that well describes the existence of the magic numbers and the pronounced stability of certain nuclei in proximity of the shell closures. Bohr recognized the importance of combining these two models for a correct description of nuclear properties. Indeed in his work of 1952 he wrote [64]:

> *The necessity of combining the two models is clearly indicated by the observed behaviour of nuclear quadrupole moments. On one hand, as already mentioned, the quadrupole moments give definite evidence of shell structure; [...] on the other hand, for many nuclei, the magnitude of the quadrupole moments is too large to be accounted for in terms of individual nucleons and suggests that the equilibrium shape of the nucleus itself deviates from spherical symmetry.*

The solution for a correct description of the quadrupole deformation was found in a change of the coordinates that allows separating the vibrational and the rotational part.

Quadrupole deformation

The fundamental collective type of low-lying excitations is the quadrupole excitation ($\lambda = 2$), where the nucleus has the shape of an ellipsoid randomly oriented in the space. The five coordinates that map the surface are $\{\alpha_{2,\mu}\} = \{a_0, a_2, \theta_1, \theta_2\theta_3\}$ where θ_i describes the orientation of the ellipsoid, while a_i parametrize the deformation. Another more commonly used set of coordinates is the Hill-Wheeler coordinates $\{\beta, \gamma, \theta_i\}$ that is related to the previous set as [64]:

$$a_0 = \beta cos\gamma \, , \tag{A.8}$$

$$a_2 = \frac{\beta}{\sqrt{2}} sin\gamma \tag{A.9}$$

where β describes the total deformation of the nucleus while γ describes the deviations from rotational symmetry. A schematic view of different quadrupole-deformed shapes as a function of the two coordinates (β, γ) is presented in Figure A.2. At $\gamma = 0°$ the nucleus is found in a *prolate* shape (cigar-like shape) while at $\gamma = 60°$ the nucleus is found in an *oblate* shape

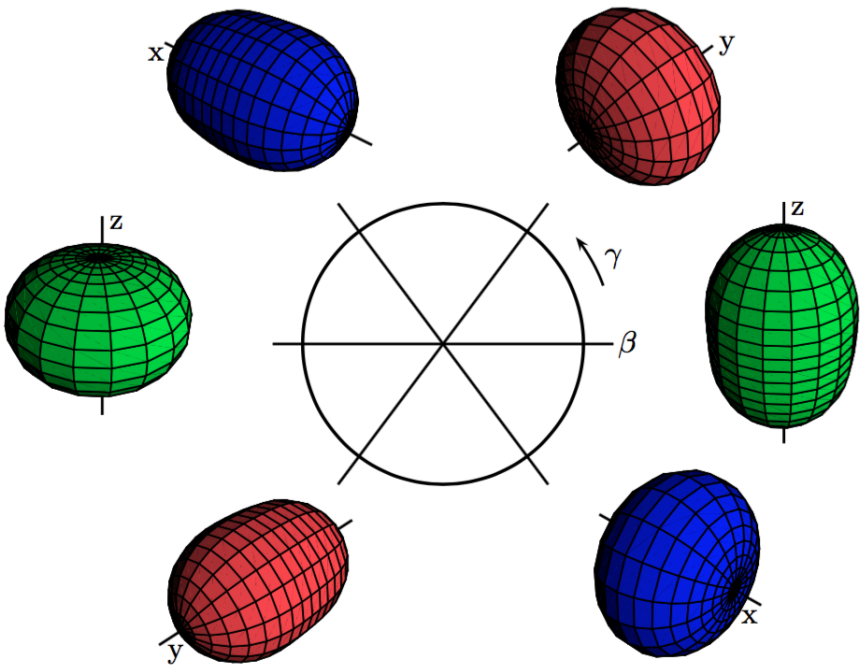

Figure A.2.: Illustration of the quadrupole-deformed shapes as a function of the Hill-Wheeler coordinates $\{\beta, \gamma\}$, with $\beta = 0.4$ and $\gamma = n \cdot 60°$, $n \in \{0, 1, 2, 3, 4, 5\}$. Different colors represent different principal axes of symmetry (green for z, red for y, blue for x). Figure taken from the work of L. Fortunato [65].

(disk-like shape). For $0° < \gamma < 60°$ the nucleus has a triaxial shape, meaning that it is an ellipsoid with the rotational axis that does not match any of its symmetry axes.

B

Nuclear reactions

Nuclear reactions are complex quantum mechanic processes that depend on many factors, such as the nuclear structure of the reaction partners and the energies involved in the collision. However, some common ways to classify the reaction mechanisms is through the impact parameter b, the transferred angular momentum L or the energy E. The classification of the different nuclear reactions based on the impact parameter is schematized in Figure B.1: when the b is large, the nuclei are mainly affected by the Coulomb force and elastic scattering is observed, as in Rutherford scattering or Coulomb excitation; at smaller value of b the nuclear forces start to be more effective and few nucleons can be transferred through the reaction, as in the case of stripping, pick up, break-up and knock out; finally, at small value of b, the two nuclei overlap completely and a compound nucleus can be formed at a high excitation energy: this is the case for fusion-fission or fusion-evaporation reactions [29].

The following sections will be focused on Coulomb excitation and fusion-evaporation reactions that are related to the case of this thesis.

Coulomb excitation

In Coulomb excitation (CE) reactions the target nucleus is excited by the interaction with the electromagnetic field of the projectile nucleus and vice versa [29]. The primary advantage in using sub-barrier CE, also called *safe Coulex*, is that it is possible to consider the strong force component negligible in the excitation process. Indeed, in a semi-classical approach, at these energies the two nuclei do not overlap and the electromagnetic interaction is dominant. In such approximation, the cross section can be expressed as

$$\sigma \approx \left(\frac{Ze^2}{\hbar c}\right)^2 \frac{B(E\lambda; 0 \to \lambda)}{e^2 b_{min}^{2\lambda-2}} \frac{1}{1-\lambda} \tag{B.1}$$

where the multipolarity of the transition is $\lambda \geq 2$, b_{min} is the minimum impact parameter and $B(E\lambda; 0 \to \lambda)$ is the reduced transition probability.

The proportionality of σ and $B(E\lambda)$ allows to calculate the reduced transition probability from cross-section measurement. Moreover, at the considered energies, the excited states are populated directly from the ground state and, due to the multipolarity dependence of the cross section, $E2$ transitions are particularly favoured. Therefore, in even-even nuclei the Coulomb excitation process populates predominantly the first 2^+ states. This is fundamental

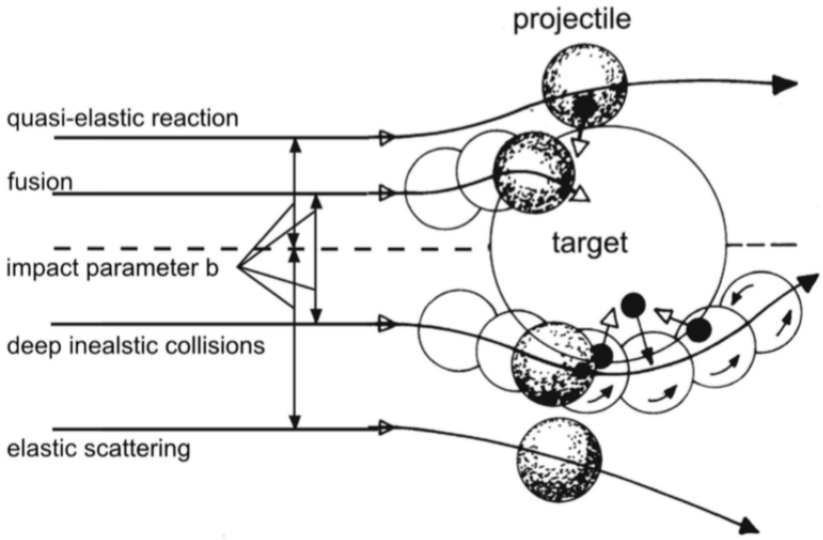

Figure B.1.: Representation of different heavy reactions depending on the impact parameter b. At larger value of b, the Coulomb force dominates and the elastic scattering is observed. At smaller value of b, the strong forces become important and the transfer of few nucleons from a nucleus to the other can happen. When the two nuclei overlap completely the fusion is observed. Figure from [66].

in the study of shape coexistence via Coulomb excitation (see Chapter 1).

Fusion-evaporation reactions

A fusion-evaporation (FE) reaction can occur because of a strong overlap between the projectile and the target distributions, leading the two colliding partners to fuse together in the compound nucleus (CN). As schematically represented in Figure B.2, the resulting CN is formed in a highly excited state with high angular momentum and the excitation energy is redistributed between the nucleons, as they rearrange themselves. If the excitation energy is sufficiently low to make the nucleus stable against fission, the de-excitation process takes place through the evaporation of particles (protons, neutrons, alphas, etc.). When the excitation energy is not sufficient for any further particle evaporation, the final nucleus is still formed in a highly excited state, the so called *entry region*. Then, as soon as the excitation energy of the evaporation residue is below the neutron-separation energy, the γ-ray emission becomes the dominant de-excitation mode so the directly-populated high-spin states decay to lower-spin states. Thus, if the statistics is sufficient, with this reaction mechanism it is possible to study nearly every state of the nucleus, while in Coulomb-excitation only the lower states are populated. This is fundamental in the study of the ^{188}Hg (see Chapter 4).

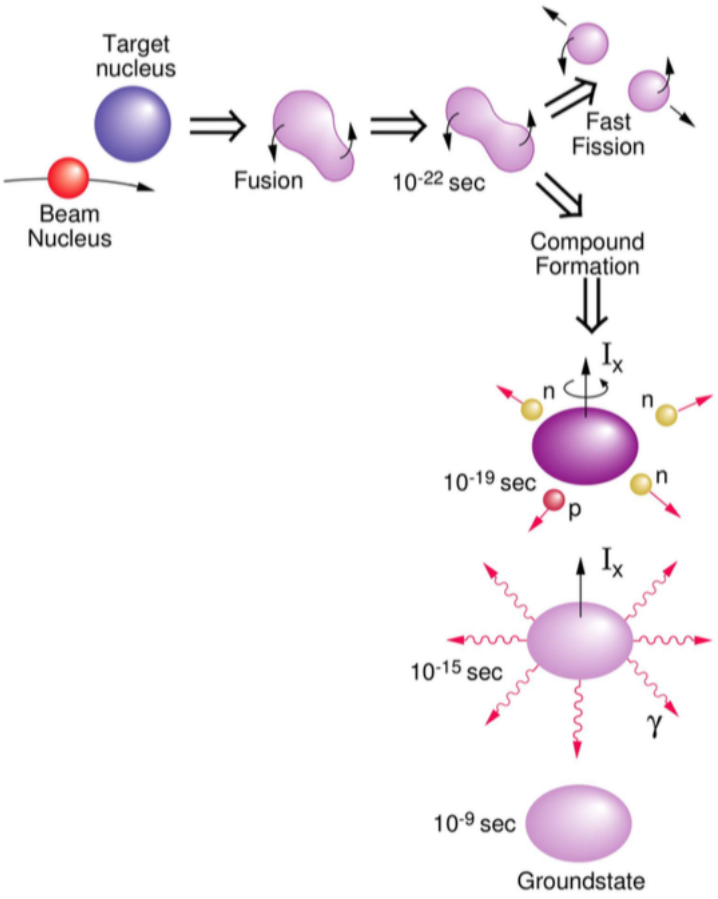

Figure B.2.: Schematic view of a fusion-evaporation reaction. After the target and projectile nuclei interact, the compound nucleus starts the de-excitation process evaporating first particles (protons, neutrons, alpha) and then γ ray. If the energy of the reaction is too high the formed nucleus beaks into fission fragments.

C Electromagnetic radiation

As a product of a nuclear reaction between the ion beam and the target, in most of the cases the final nucleus is in an excited state. In order to get rid of the excess of energy, the nucleus evaporates particles (n, p, α) and/or emits electromagnetic (e.m.) radiation.

A γ ray is a photon emitted after a nuclear reaction, with a typical energy in the range of 0.1 to 10 MeV. For example, let us consider a nucleus of mass M in an initial excited state E_i that emits a γ ray decaying to a state of E_f. For conservation laws we know that

$$\begin{aligned} E_\gamma &= E_i - E_f - T_R \\ \vec{p_R} + \vec{p}_\gamma &= 0 \end{aligned} \tag{C.1}$$

where T_R and p_R are the energy and momentum of the recoil respectively. Considering that for photons the relation between energy and momentum is $E_\gamma = cp_\gamma$, Eq. (C.1) can me rewritten as

$$E_\gamma = E_i - E_f - \frac{E_\gamma^2}{2Mc^2} \equiv \Delta E - \frac{E_\gamma^2}{2Mc^2}\,. \tag{C.2}$$

The positive solution of Eq. (C.2) provides the energy of the emitted γ ray

$$E_\gamma = Mc^2\left(-1 \pm \sqrt{1 + \frac{\Delta E}{2Mc^2}}\right) \tag{C.3}$$

that is different from the bare ΔE, because of the radioactive nucleus recoils emitted in the opposite direction with respect to the γ ray. Considering the energy range for γ ray and that the mass of the nucleus is of the order of 10−100 GeV, in most cases $\Delta E \ll Mc^2$, so Eq. (C.3) can be expanded in

$$E_\gamma = \Delta E + \frac{(\Delta E)^2}{2Mc^2}\,. \tag{C.4}$$

C.1. Classical interpretation

From the nuclear de-excitation via γ-ray emission, an electric and/or magnetic character can be identified from the spacial symmetry of the radiation. Such properties can be deduced from a classical interpretation of the e.m. force.

Let us consider a distribution of charge or current: when such distribution is static, it

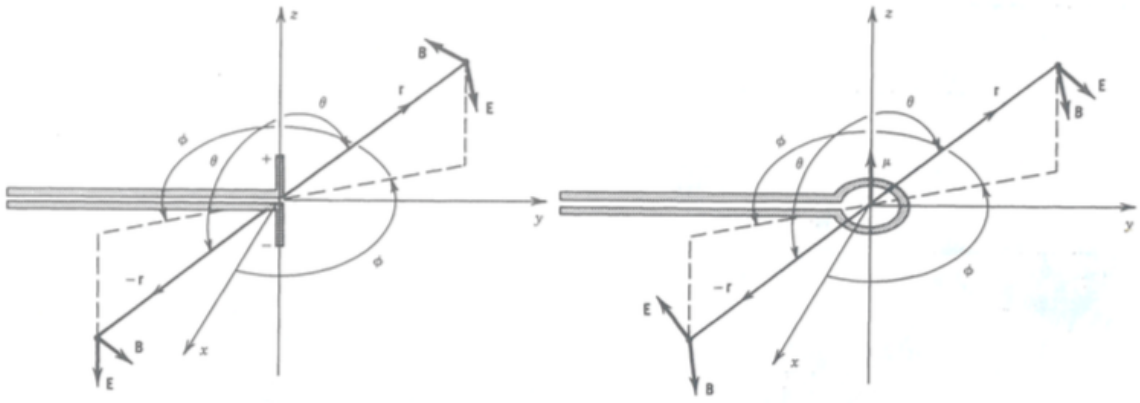

Figure C.1.: On the left is shown the electric field generated by an electric dipole. On the right the magnetic field generated by a magnetic dipole. Figure taken from [29].

generates a static electric or magnetic field respectively; however, when the distribution varies in time, it generates a radiation field. These fields can be analysed in terms of multipole characters; for example, let us consider the lowest multipole order: the dipole. In Figure C.1 are shown an electric field $\vec{E}$ and magnetic field $\vec{B}$. The electric dipole consists of two equal and opposite charges $+q$ and $-q$ separated by a distance $\vec{z}$, and the electric moment is $\vec{d} = q\vec{z}$. If we consider a parity transformation $\vec{r} \to -\vec{r}$ we see that $\vec{d} \to -\vec{d}$. A magnetic dipole consists in a circular current loop enclosing an area A, and the dipole moment is $\vec{\mu} = i\vec{A}$ that can also be written as $\vec{\mu} = q\vec{r} \times \vec{v}$. If we consider again a parity transformation $\vec{r} \to -\vec{r}$ and $\vec{v} \to -\vec{v}$, the magnetic dipole does not change. Such property of dipoles can be extended to higher order multipolarity: we define the index L of the radiation so that 2^L is the multipole order (e.g. $L = 0$ correspond to the monopole, $L = 1$ to the dipole and so on). The parity π depends on the L index and is

$$\begin{aligned} \pi(EL) &= (-1)^L \\ \pi(ML) &= (-1)^{L+1} \end{aligned} \tag{C.5}$$

for electric and magnetic fields, respectively. We can notice that, at the same order, the two fields have opposite parity.

Let us consider a dipole that varies sinusoidally in time, producing a radiation field. The radiation will propagate in $\vec{E} \times \vec{B}$ direction. The average power radiated depends on the frequency of the oscillating dipole ω and on the amplitude of the moments $\vec{d}$ and $\vec{\mu}$. Thus, the radiation power for electrical dipole is

$$P = \frac{1}{12\pi\epsilon_0}\frac{\omega^4}{c^3}d^2\,, \tag{C.6}$$

where ϵ_0 is the dielectric constant in vacuum, while for magnetic dipole it is

$$P = \frac{1}{12\pi\epsilon_0}\frac{\omega^4}{c^5}\mu^2\,. \tag{C.7}$$

Considering the symmetry of Eq. (C.5), these formulas can be generalized both for the e.m. character and for higher multipole orders. The radiation power becomes

$$P(\sigma L) = \frac{2(L+1)c}{\epsilon_0 L[(2L+1)!!]^2}\left(\frac{\omega}{c}\right)^{2L+2}[m(\sigma L)]^2\,, \tag{C.8}$$

where σ can be equal to E or M to represent electric or magnetic multipole moment and $m(\sigma L)$ is the generalized multipole moment.

C.2. Quantum interpretation and selection rules

Starting from the classical model, other important features of e.m. radiation can be obtained considering a quantum approach. This can be obtained by replacing in Eq. (C.8) the generalized multipole moment with the multipole operator. Such operator changes the nucleus from the initial state ψ_i to the final state ψ_f, so the matrix element, also known as multipole operator, can be written as

$$m_{fi}(\sigma L) = \int \psi_f^* m(\sigma L)\psi_i d\vec{r}. \tag{C.9}$$

If we divide Eq. (C.8) for the single photon energy $\hbar\omega$ we obtain the probability per unit time for photon emission. However, to calculate such quantity it is necessary to know the multipole operator, which is a very complex object. The calculations can be simplified by considering only a single photon emission between two shell-model states and also assuming the radial part to be constant. In this way the probability becomes [67]:

$$\begin{aligned}
\lambda(EL) &= \frac{8\pi(L+1)}{L[(2L+1)!!]^2}\frac{e^2}{4\pi\epsilon_0\hbar c}\left(\frac{E_\gamma}{\hbar c}\right)^{2L+1}\left(\frac{3}{L+3}\right)^2 cR^{2L} \\
\lambda(ML) &= \frac{8\pi(L+1)}{L[(2L+1)!!]^2}\left(\mu_p - \frac{1}{L+1}\right)^2\left(\frac{\hbar}{m_p c}\right)^2\frac{e^2}{4\pi\epsilon_0\hbar c}\left(\frac{E_\gamma}{\hbar c}\right)^{2L+1}\left(\frac{3}{L+3}\right)^2 cR^{2L-2}
\end{aligned} \tag{C.10}$$

where the nuclear radius is considered to be $R = R_0 A^{1/3}$ with A the atomic mass, m_p is the proton mass, μ_p is the magnetic moment of the proton and E_γ is the energy of the γ ray. These estimations are known as *Weisskopf estimates* and they are often used as a reference to compare measured transition rates. For example, if the measured rate is much higher than the Weisskopf estimates, one can deduce that more than a single nucleon is involved in the transition so the nuclear structure presents a collective behaviour. In Table C.2 are shown the Weisskopf estimates for electric and magnetic transitions for different multipolarity order as a function of the energy and the atomic mass of the nucleus, while in Figure C.2 the Weisskopf estimates are shown for $A = 188$. The figure clearly highlights the dependence of the transition probability on the angular momentum and on the character of the radiation: for a fixed initial and final level, transitions with lower angular momentum are more probable than those with higher angular momentum and electric transitions are favoured with respect to magnetic transitions for a fixed angular momentum.

The electromagnetic field transmits not only energy, but also angular momentum and every photon carries a certain angular momentum. If we consider an electromagnetic transition

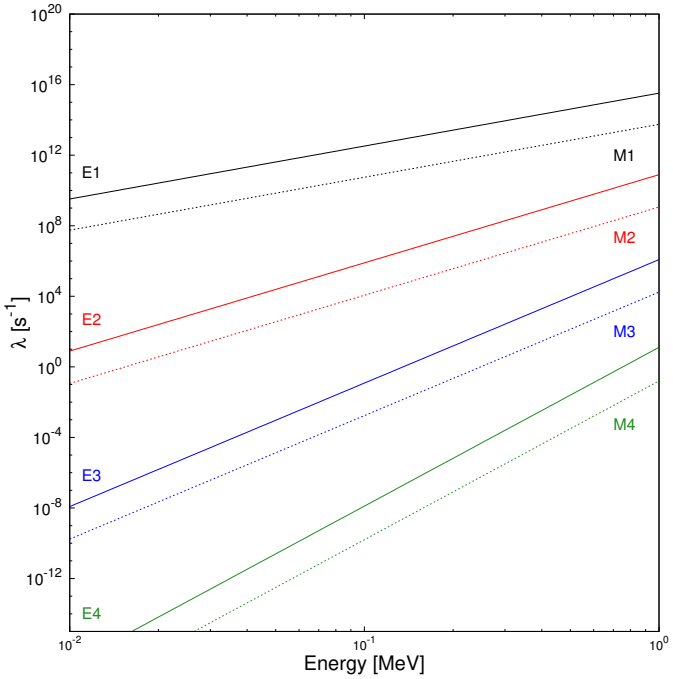

Figure C.2.: Weisskopf estimates for $A = 188$ for electric (E) and magnetic (M) multipoles, depending on the γ ray energy.

Electric multipole $[s^{-1}]$	Magnetic multipole $[s^{-1}]$
$\lambda(E1) = 1.0 \times 10^{14} A^{2/3} E^3$	$\lambda(M1) = 5.6 \times 10^{13)} E^3$
$\lambda(E2) = 7.3 \times 10^{7} A^{4/3} E^5$	$\lambda(M2) = 3.5 \times 10^{7} A^{2/3} E^5$
$\lambda(E3) = 34 A^2 E^7$	$\lambda(M3) = 16 A^{4/3} E^7$
$\lambda(E4) = 1.1 \times 10^{-5} A^{8/3} E^9$	$\lambda(M4) = 4.5 \times 10^{-6} A^2 E^9$

Table C.1.: Values of Weisskopf estimates depending on the energy (E) and the atomic number (A).

from state ψ_i with angular momentum $\vec{I}_i$ to ψ_f with angular momentum $\vec{I}_f$, since the angular momentum is conserved, this transition must be

$$\vec{I}_f = \vec{I}_i + \vec{L}\,. \tag{C.11}$$

Thus, considering the sum rules for quantum mechanics, the values of the momentum that the emitted photon can carry are

$$|I_i - I_f| \leq L \leq I_i + I_f \tag{C.12}$$

Finally, another important consideration must be made: since a photon carries an intrinsic angular momentum $L = 1$, transitions with $\Delta L = 0$ are not allowed with the emission of a single photon. However, this kind of transitions can happen via internal conversion, as it will be explained in the following paragraph.

C.3. Internal conversion

Internal conversion (IC) is an electromagnetic process that competes with the γ emission for the nuclear de-excitation: when the electromagnetic field produced by the nucleus interacts with an atomic electron, it causes the emission of the latter. For this reason the inner electrons are more likely to be involved in this phenomenon. Thus, at the contrary of β decay, during internal conversion no electron is created, but it already exists in the atom and so the chemical environment can influence the process [29].

The kinetic energy of the emitted electron results to be

$$T_e = \Delta E - B_e\,, \tag{C.13}$$

where ΔE is the transition energy and B_e is the binding energy of the electron. Since the binding energy is higher for more internal shell (for example K-shell), the electron kinetic energy is lower than for external shell transition, as L or M. Figure C.3 shows a typical electron spectrum emitted by a radioactive nucleus, where the continuous background from β decay and δ-electron emission can be distinguished from the discrete peaks of IC. In particular it can be seen that more internal shell electrons (K) are detected at lower energy with respect to more external (L, M) but with a higher statistics.

After the electron emission, the vacancy left in the atomic shell is rapidly filled by the electrons from higher shells, causing the emission of the characteristic X-ray that can be observed in the lower energy part of the spectrum.

As already introduced, internal conversion competes with γ-ray emission during the de-excitation process. The total decay probability of a nuclear level can be written as:

$$\lambda_t = \lambda_\gamma + \lambda_e \equiv \lambda_\gamma(1 + \alpha) \tag{C.14}$$

where λ_γ is the probability of γ decay, λ_e is the probability of internal conversion and then α is defined as the internal conversion coefficient (ICC). The α coefficient can be also written as a sum of many terms corresponding to the different shells contributions.

From experimental data and non relativistic theoretical calculations, the ICC for electric

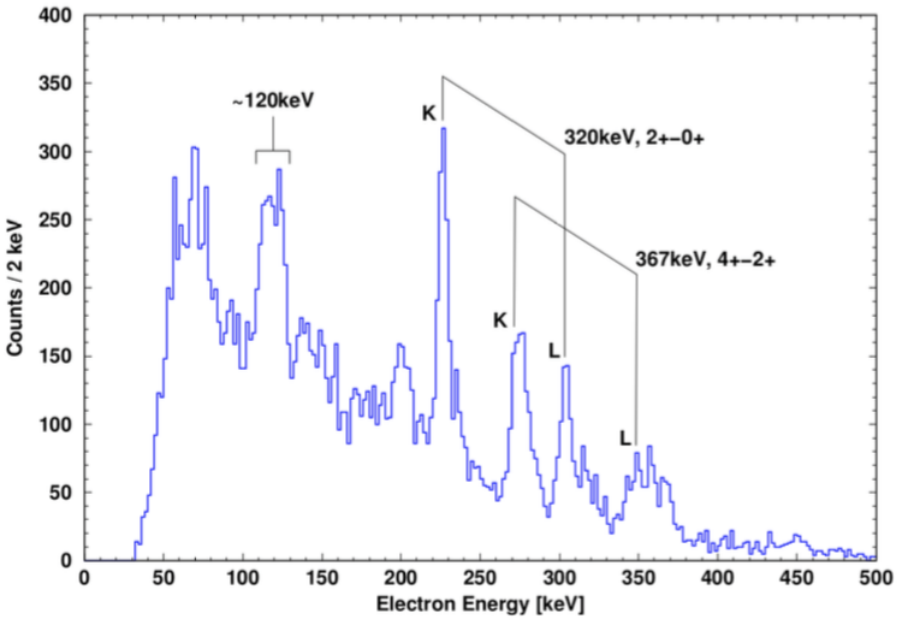

Figure C.3.: Prompt single conversion electron energy spectrum from the reaction ^{170}Yb(^{28}Si,4n)^{194}Po, tagged with ^{194}Po α-decay. The four peaks in figure correspond to two different discrete transitions of electrons from the K and L electronic shells. Figure taken from [68].

(E) and magnetic (M) multipoles result to be [29]

$$\begin{aligned} \alpha(EL) &\cong \frac{Z^3}{n^3}\left(\frac{L}{L+1}\right)\left(\frac{e^2}{4\pi\epsilon_0\hbar c}\right)^4\left(\frac{2m_ec^2}{E}\right)^{L+5/2} \\ \alpha(ML) &\cong \frac{Z^3}{n^3}\left(\frac{e^2}{4\pi\epsilon_0\hbar c}\right)^4\left(\frac{2m_ec^2}{E}\right)^{L+3/2} \end{aligned} \tag{C.15}$$

where Z is the atomic number and n is the principal quantum number of the bound electron wave function. From Eq. (C.15) it is possible to deduce some important properties of this phenomenon:

1. the e.m. field interacts with existing electrons, so the internal conversion is more competitive in heavy nuclei, since it depends on Z^3;

2. unlike γ-ray emission, the conversion coefficient decreases with increasing transition energy, since it depends $1/E_\gamma$;

3. unlike γ-ray emission, the conversion coefficient increases for higher multipole orders, since it depends on L;

4. since IC is more effective for internal electrons, the conversion coefficient decrease for higher atomic shell and it depends on $1/n^3$.

E0 transition

As anticipated in the previous section, electric monopole (E0) transitions are forbidden via single γ-ray emission, since a photon cannot carry a null angular momentum, while they can occur via internal conversion. In E0 transitions the angular momentum of the nucleus does not change but the the nuclear surface is altered, so such process gives important information on the nuclear radius and on deformations.

A particular case of E0 transition is the $0^+ \rightarrow 0^+$ transition, where the only angular momentum allowed is $L = 0$. The transition is still allowed via internal transition or, if the energy of the transition is higher than two times the electron mass, via pair production. Since the γ-ray emission is forbidden, the definition of the ICC from Eq. (C.14) loses its meaning and another quantity is necessary to quantify the phenomenon. The quantity used to characterize the E0 transitions is the monopole strength [69]

$$\rho^2 = \left| \frac{\langle \phi_f | \sum e_j r_j^2 | \phi_{ij} \rangle}{eR^2} \right|^2 \tag{C.16}$$

where ϕ_f and ϕ_{ij} are the final and initial states, R is the nuclear radius, e is the electron charge and r_j is the proton position. A large monopole strength is an indicator of a strong mixing between states characterized by different shapes, as highlighted by

$$\rho \propto \frac{\Delta\langle r^2 \rangle Z}{R^2} \tag{C.17}$$

where $\Delta\langle r^2 \rangle$ is the the difference between the mean square of the charge radius of the two coexisting shape.

C.4. Gamma-matter interaction

Many nuclear properties can be deduced by studying the level scheme of a nucleus via γ spectroscopy. Different detectors can be used for the detection of γ rays, each of them with different characteristics based on the properties of the material. In particular, the mechanisms of the radiation interaction with matter is fundamental to better understand how these detectors work.

In the energy range of interest for nuclear studies with γ ray, which is about from 10 keV$-$10 MeV, there are three ways in which the electromagnetic radiation interacts with matter: the photoelectric absorption, the Compton scattering and the pair production. Each of these phenomenons is dominant in a different range of energy, as showed in Figure C.4.

In the photoelectric effect, a photon is absorbed by the atom while an atomic electron, called photoelectron, is emitted. The kinetic energy of the photoelectron is:

$$T_e = E_\gamma - B_e \,, \tag{C.18}$$

where E_γ is the energy of the absorbed photon and B_e is the binding energy of the atomic electron. The cross section of the process depends on the atomic number of the material and on the energy of the γ ray

$$\sigma \approx \frac{Z^n}{E^{3.5}} \tag{C.19}$$

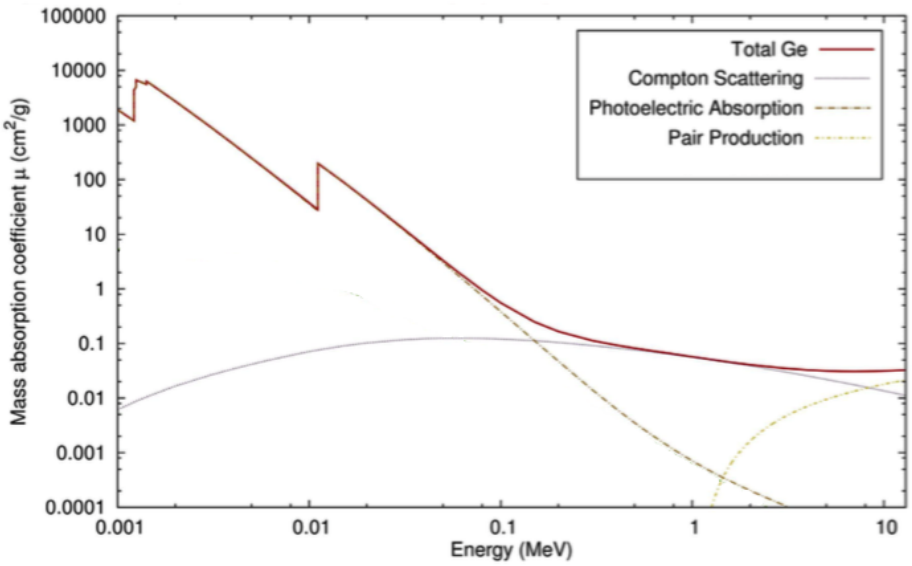

Figure C.4.: Mass absorption coefficient for germanium material as a function of the energy for the different interaction modes. At lower energy the photoelectric is dominant, while the Compton scattering becomes important at about 100 keV. Finally for energy higher than $2m_ec^2$ the pair production mechanism appears and it dominates at higher energy (about 10 MeV). Figure adapted from [70].

and the photoelectric effect is significant around 100 keV while its importance decrease at higher energy. Moreover, the dependence of the cross section on the atomic number implies that heavier material are more effective for the detection of γ ray: this is one of the reasons why germanium detectors ($Z = 32$) are usually preferred to silicon detectors ($Z = 14$).

In Compton scattering, a photon scatters from an electron: in this process, the photon loses energy and changes direction, while the electron carries the energy loss by the photon. The energy of the scattered photon depends on the scattering angle, as showed in the Compton-scattering formula

$$E_\gamma^{'} = \frac{E_\gamma}{1 + (E_\gamma/mc^2)(1 - \cos\theta)} \tag{C.20}$$

The angular distribution of the scattered photons is predicted by the Klein-Nishina [71] formula and results to linearly depend on the atomic number of the material. This process is dominant at energy between 0.1 and 10 MeV.

Finally, in pair production a photon interacting with matter creates a couple of electron and positron. From empirical results, the cross section of this process is observed to be proportional on Z^2. This process has a threshold of two times the mass of the electron and is dominant at high energy (above 10 MeV). Both in pair production and in Compton scattering, it can happen that the photon does not lose all the energy in the process and can escape from the detector. These events affect the spectrum, appearing as a continuous background or as additional full-energy peaks at 511 keV (single-escape peak) or 1022 (double-escape peak).

Bibliography

[1] K. Heyde and J. Wood. *Shape coexistence in atomic nuclei.* Review of Modern Physics 83, 1467 (2011).

[2] P. Van Duppen and M. Huyse. *Shape coexistence around Z=82 closed shell probed by α-decay.* Hyperfine Interactions 129, 149 (2000).

[3] M. Dufour and A. Zuker. *Realistic collective nuclear Hamiltonian.* Physical Review C 54, 1641 (1996).

[4] I. Angeli and K. Marinova. *Table of experimental nuclear ground state charge radii: An update* (2013).

[5] A. Andreyev et al. *A triplet of differently shaped spin- zero states in the atomic nucleus ^{186}Pb.* Nature 405, 430 (2000).

[6] T. Kibedi and R. H. Spear. *Electric monopole transitions between 0+ states for nuclei throughout the periodic table.* Atomic Data and Nuclear Data Tables 89, 77 (2005).

[7] F. Hannachi et al. *High-spin excitaion of $^{187,188}Hg$.* Nuclear Physics A 481, 135 (1988).

[8] K. Hardt et al. *Observation of the weakly deformed $\nu i^2_{13/2}$ band in ^{188}Hg.* Zeitschrift für Physik A Atoms and Nuclei 312, 251 (1983).

[9] R. Julin, K. Helariutta and M. Muikku. *Intruder states in very neutron-deficient Hg, Pb and Po nuclei.* Journal of Physics G 27 (2001).

[10] L. Gaffney et al. *Shape coexistence in the neutron-deficient isotope studied via lifetime measurements in $^{184,186}Hg$ and two-state mixing canculations.* Physical Review C 89, 024307 (2014).

[11] T. Nikšić, D. Vretenar, P. Ring and G. Lalazissis. *Shape coexistence in the relativistic Hartree-Bogoliubov approach.* Physical Review C 65, 054320 (2002).

[12] N. Bree et al. *Shape Coexistence in the Neutron-Deficient Even-Even $^{182-188}Hg$ Isotope Studied via Coulomb Excitation.* Physical Review Letter 112, 162701 (2014).

[13] N. Bree. *Shape coexistence in the neutron-deficient mercury isotopes studied through coulomb excitation.* Ph.D. thesis, KU Leuven (Belgium) (2014).

[14] T. Grahn et al. *Evolution of collectivity in ^{180}Hg and ^{182}Hg.* Physical Review C. 80, 014324 (2009).

[15] M. Scheck et al. *Lifetime of odd-spin yrast states in ^{182}Hg.* Physical Review C. 81, 014310 (2010).

[16] N. Rud et al. *Lifetimes in the Ground-state band of ^{184}Hg.* Physical Review Letter 31, 1421 (1973).

[17] D. Proetel, R. Diamond and F. Stephens. *Nuclear deformations in ^{186}Hg from lifetime measurements.* Physical Review B 48, 102 (1974).

[18] A. Schwarzschild and E. Warburton. *The measurement of short nuclear lifetimes.* Annual Review Nuclear Science 18, 265 (1968).

[19] W. Ma et al. *The structure of high spin states in ^{184}Hg and ^{186}Hg.* Physics Letters B 167, 277 (1986).

[20] A. Sonzogni et al. *Nudat 2.*

[21] *Laboratori Nazionali di Legnaro webpage.*

[22] *SPES webpage.*

[23] C. Signorini, G. Bezzon, F. Cervellera, P. Spolaore and R. Ricci. *Acceptance tests of the Legnaro XTU tandem.* Nuclear Instruments and Methods in Physics Research A 220, 30 (1984).

[24] C. Signorini, F. Cervellera and G. Bezzon. *Status report of the Legnaro XTU tandem.* Nuclear Instruments and Methods in Physics Research A 244, 27 (1986).

[25] A. Danielli et al. *Commissioning of the ALPI post-accelerator.* Nuclear Instruments and Methods in Physics Research A 382, 100 (1996).

[26] J. Valiente-Dobón, D. Mengoni and F. Recchia. *Status of the Gamma-Ray Spectrometer GALILEO.* Laboratori Nazionali di Legnaro (2015).

[27] D. Mengoni, F. Recchia and J. Valiente-Dobón. *The GALILEO array at LNL.* Laboratori Nazionali di Legnaro (2013).

[28] G. F. Knoll. *Radiation detection and measurement* (John Wiley & Sons, 1979).

[29] K. Krane and D. Halliday. *Introductory nuclear physics* (Wiley New York, 1988).

[30] E. Tronchin, M. Siciliano, D. Testov et al. *Tuning of the BGO anti-Compton shield in the GALILEO array.* Laboratori Nazionali di Legnaro (2015).

[31] A. Goasduff et al. *Possible geometries of GALILEO phase II.* Laboratori Nazionali di Legnaro (2016).

[32] A. Goasduff. *Galileo simulations: from optimizing the set-up to the interpretation of the data* (2017).

[33] Ö. Skeppsted et al. *The EUROBALL neutron wall - design and performance tests of neutron detectors.* Nuclear Intrumentation and Method in Physics Research A 421, 531 (1999).

[34] J. Ljungvall, M. Palacz and J. Nyberg. *Monte Carlo simulations of the Neutron Wall detector system.* Nuclear Instruments and Methods in Physics Research A 528, 741 (2004).

[35] A. Goasduff et al. *A New Dedicated Plunger for the GALILEO γ-ray array.* Laboratori Nazionali di Legnaro (2015).

[36] D. Bazzacco. *Private communication.*

[37] Z. Kis, B. Fazekas, J. Östör, Z. Révay, T. Belgya, G. L. Molnár and L. Koltay. *Comparison of efficiency functions for Ge gamma-ray detectors in a wide energy range.* Nuclear Instruments and Methods in Physics Research A 418, 374 (1998).

[38] *Radware webpage.*

[39] B. Fazekas, J. Östör, Z. Kis, G. Molnár and A. Simonits. *The new features of hypermet-pc.* In *Proceedings of the 9th International Symposium on Capture gamma-ray spectroscopy and related topics* (1997).

[40] W. Leo. *Techniques for Nuclear and Particle Physics* (Springer, 1987).

[41] A. Dewald, O. Möller and P. Petkov. *Developing the Recoil Distance Doppler-Shift technique towards a versatile tool for lifetime measurements of excited nuclear states.* Progress in Particle and Nuclear Physics 67, 786 (2012).

[42] T. Alexander and A. Bell. *A target chamber for recoil-distance lifetime measurements.* Nuclear Instruments and Methods in Physics Research A 81, 22 (1970).

[43] P. John, A. Goasduff, G. Jaworski and D. Mengoni. *Doppler Correction Performance via Complete Kinematic Reconstruction for GALILEO Coupled to EUCLIDES and NeutronWall.* Laboratori Nazionali di Legnaro (2015).

[44] D. Testov, A. Goasduff et al. *Light charged particle detector EUCLIDES for the GALILEO campaign.* Laboratori Nazionali di Legnaro (2014).

[45] I. Zanon et al. *Shape Coexistence in the Neutron-Deficient ^{188}Hg Isotope.* Laboratori Nazionali di Legnaro (2017).

[46] H. Bateman. *The solution of a system of differential equations occurring in the theory of radioactive transformations.* In *Proceeding of the Cambridge Philosophical Society, Mathematical and Physical Sciences* (1910), volume 15, p. 423.

[47] D. Ward, H. Andrews, J. Geiger and J. Sharpey-Schafer. *Lifetimes for level above the "Rotational Phase Change" in ^{158}Er.* Physical Review Letter 30, 493 (1973).

[48] A. Dewald, S. Harissopulos and P. Von Brentano. *The differential plunger and the differential decay curve method for the analysis of recoil distance Doppler-shift data.* Zeitschrift für Physik A 334, 163 (1989).

[49] L. Gaffney. *Private comunication.*

[50] R. Bernard, L. Robledo and T. Rodríguez. *Octupole correlation in the ^{144}Ba nucleus described with symmetry-conserving configuration-mixing calculations.* Physical Review C 93, 061302(R) (2016).

[51] T. Rodríguez and J. Egido. *Triaxial angular momentum projection and configuration mixing calculations with the Gogny force.* Physical Review C 81, 064323 (2010).

[52] T. Rodríguez and J. Egido. *Configuration mixing description of the nucleus ^{44}S.* Physical Review C 84, 051307 (2011).

[53] T. Rodríguez. *Structure of krypton isotopes calculated with symmetry-conserving configuration-mixing methods.* Physical Review C 90, 034306 (2014).

[54] M. Anguiano, J. Egido and L. Robledo. *Particle number projection with effective forces.* Nuclear Physics A 696, 467 (2001).

[55] T. Rodriguez. *Private comunication.*

[56] P. Ring and P. Schuck. *The Nuclear Many-Body Problems* (Springer Verlag, 1980).

[57] H. J. Lipkin. *Collective motion in many-particle systems: Part 1. The violation of conservation laws.* Annals of Physics 9, 272 (1960).

[58] Y. Nogami. *Improved superconductivity approximation for the pairing interaction in nuclei.* Physical Review 134, B313 (1964).

[59] W. Greiner and J. Maruhn. *Nuclear Models* (Springer, 1996).

[60] A. Bohr and B. Mottelson. *Nuclear structure: nuclear deformations*, volume 2 (World Scientific, 1998).

[61] M. Mayer-Goepper. *Nuclear Configurations in the Spin-Orbit Coupling Model. I. Empirical Evidence.* Physics Review Journal 78 (1950).

[62] M. Mayer-Goepper. *Nuclear Configurations in the Spin-Orbit Coupling Model. II. Theoretical Considerations.* Physics Review Journal 78 (1950).

[63] O. Haxel, J. Jensen and H. Seuss. *On the "Magic Numbers" in Nuclear Structure.* Physics Review Journal 75 (1949).

[64] A. Bohr. *The coupling of nuclear surface oscillations to the motion of individual nucleons.* Matematiks-fhysiske Maddelelser 26 (1952).

[65] L. Fortunato. *Solutions of the Bohr Hamiltonian, a compendium.* European Physics Journal A 26 (2005).

[66] K. Berthge, G. Walter and B. Wiedemann. *Kernphysik: eine Einfuhrung* (Springer-Verlag, 2008).

[67] V. F. Weisskopf. *Radiative Transition Probabilities in Nuclei.* Physical Review 83, 1073 (1951).

[68] M. Siciliano. *Shape Coexistence in the Neutron-Deficient Nucleus ^{194}Po.* Master's thesis, Università degli Studi di Padova (2013).

[69] K. Heyde and R. Meyer. *Monopole strength as a measure of nuclear shape mixing.* Physical Review C 37 (1987).

[70] *Nist: Physical Measurement Laboratory webpage.*

[71] O. Klein and Y. Nishina. *Über die streuung von strahlung durch freie elektronen nach der neuen relativistischen quantendynamik von dirac.* Zeitschrift für Physik 52, 853 (1929).